

2-1-2016

Analysis, Implementation and Considerations for Liquid Crystals as a Reconfigurable Antennas Solution (LiCRAS) for Space

Derek Doyle

Follow this and additional works at: https://digitalrepository.unm.edu/ece_etds

Recommended Citation

Doyle, Derek. "Analysis, Implementation and Considerations for Liquid Crystals as a Reconfigurable Antennas Solution (LiCRAS) for Space." (2016). https://digitalrepository.unm.edu/ece_etds/71

This Dissertation is brought to you for free and open access by the Engineering ETDs at UNM Digital Repository. It has been accepted for inclusion in Electrical and Computer Engineering ETDs by an authorized administrator of UNM Digital Repository. For more information, please contact disc@unm.edu.

Derek Doyle

Candidate

Electrical and Computer Engineering Department

This dissertation is approved and is acceptable in quality and form for publication.

Approved by the Dissertation Committee

Dr. Christos Christodoulou

Dr. Mark Gilmore

Dr. Tariq Khraishi

Dr. Brandon Arritt

**Analysis, Implementation and Considerations for Liquid Crystals as a
Reconfigurable Antennas Solution (LiCRAS) for Space**

by

Derek Doyle

**Bachelor of Science, Mechanical Engineering, New Mexico Institute of
Mining and Technology, 2007**

**Master of Science, Mechanical Engineering, New Mexico Institute of
Mining and Technology, 2008**

Dissertation

Submitted in Partial Fulfillment of the
Requirement for the Degree of

**Doctor of Philosophy
Engineering**

The University of New Mexico
Albuquerque, New Mexico

December, 2015

© 2015, Derek Doyle

DEDICATION

This manuscript is dedicated to my wife, Stephanie Abercrombie, and my son, Liam Doyle who are the foundation of all my ambitions and goals in life, I hope this effort results in opportunities that make up for the sacrifices you have both had to make for this to be completed.

ACKNOWLEDGEMENTS

I would like to acknowledge the work of my student intern, Christopher Woehrle, who assisted with building test articles and executing my directions in designing and building of test articles, as well as procuring resources and equipment for testing. While I guided his research efforts for his Masters and PhD work, he quickly excelled beyond my guidance and proved to be a valuable asset for my own professional and academic endeavors. I would also like to acknowledge David Wellems who helped with understanding the modeling problems with charge migration.

I would also like to acknowledge my committee members, Dr. Christos Christodoulou, Dr. Mark Gilmore, Dr. Tariq Khraishi, and Dr. Brandon Arritt, for their valuable recommendation pertaining to this study and assistance in my professional development. Additionally I want to thank Dr. Arritt for his mentoring of my professional development at the Air Force Research Laboratories, Space Vehicles Directorate that has fostered incredible professional opportunities and provided a secure future for my family.

Analysis, Implementation and Considerations for Liquid Crystals as a Reconfigurable Antennas Solution (LiCRAS) for Space

By

Derek Doyle

B.S. in Mechanical Engineering, New Mexico Institute of Mining and Technology, 2007

M.S. in Mechanical Engineering New Mexico Institute of Mining and Technology, 2008

Ph.D., Engineering, University of New Mexico, 2015

ABSTRACT

The space industry has predominantly relied on high gain reflector dish antenna apertures for performing communications, but is constantly investing in phase array antenna concepts to provide increased signal flexibility at reduced system costs in terms of finances and system resources. The problem with traditional phased arrays remains the significantly greater program cost and complexity added to the satellite by integrating arrays of antenna elements with dedicated amplifier and phase shifters to perform adaptive beam forming. Liquid Crystal Reflectarrays (LiCRas) offer some of the electrical beam forming capability of a phased array system with the component and design complexity in lines with a traditional reflector antenna aperture but without the risks associated with mechanical steering systems. The final solution is believed to be a hybrid approach that performs in between the boundaries set by the two current disparate approaches.

Practical reflectarrays have been developed since the 90's as a means to control reflection of incident radiation off a flat structure that is electrically curved based on

radiating elements and their reflection characteristics with tailored element phase delay. In the last decade several methods have been proposed to enable tunable reflectarrays where the electrical shape of the reflector can be steered by controlling the resonating properties of the elements on the reflector using a DC bias. These approaches range from complex fast switching MEMS and ferroelectric devices, to more robust but slower chemical changes.

The aim of this work is to investigate the feasibility of a molecular transition approach in the form of liquid crystals which change permittivity based on the electrical field they are subjected to. In this work, particular attention will be paid to the impact of space environment on liquid crystal reflectarray materials and reflector architectures. Of particular interest are the effects on performance induced by the temperature extremes of space and the electromagnetic particle environment. These two items tend to drive much of the research and development for various space technologies and based on these physical influences, assertions can be made toward the space worthiness of such a material approach and can layout future R&D needs to make certain LC RF devices feasible for space use. Moreover, in this work the performance metrics of such a technology will be addressed along with methods of construction from a space perspective where specific design considerations must be made based on the extreme environment that a typical space asset must endure.

Contents

LIST OF FIGURES	x
LIST OF TABLES	xiii
CHAPTER 0: MOTIVATION.....	1
CHAPTER 1: INTRODUCTION TO SPACE TERMINALS.....	3
1.1 Mechanical Design Considerations For Space Terminals	7
1.2 Thermal Design Considerations for Space Terminals	9
1.3 Space Radiation and Electrical Design Considerations for Space Terminals	12
1.4 Traditional Space Antenna Concepts	14
1.5 Engineering Philosophy	15
CHAPTER 2: RECONFIGURABLE REFLECTARRAYS	18
2.1 Introduction.....	18
2.2 Review of Previously Designed Reconfigurable Reflectarrays	19
2.2.1 Reconfiguration Using PIN Diodes	21
2.2.2 Reconfiguration Using Varactor Biasing	23
2.2.3 Reconfiguration Using MEMS	24
2.2.4 Reconfiguration Using FETs	26
2.2.5 Reconfiguration Using Liquid Crystals	27
CHAPTER 3: A LIQUID CRYSTAL REFLECTARRAY (LiCRas) APPROACH	33
3.1 Introduction:.....	33
3.2 Characterization:	33
3.3 LC impacts in RF cell:	38
CHAPTER 4: MANUFACTURING CONCERNS FOR RECONFIGURABLE LiCRas	48
4.1 Introduction:.....	48
4.2 Printed substrates	49
4.2.1 Designing to Account for Manufacturing Errors	49
4.2.2 Dielectric Characterization of Printed Dielectrics	54
4.2.3 Space Weather Effects on 3D Printed Dielectric	62
CHAPTER 5: THERMAL/VACUUM CONCERNS FOR RECONFIGURABLE LiCRas	64
5.1 Introduction:.....	64
5.3 Applied Thermal Considerations:	70
5.4 Vacuum Considerations:	79
CHAPTER 6: RADIATION/CHARGING CONCERNS FOR RECONFIGURABLE LiCRas...	84

6.1	Introduction:.....	84
6.2	Radiation Effects on LiCRAS:.....	86
6.3	Charging Considerations:.....	96
CHAPTER 7: CONCLUSIONS AND FUTURE WORK.....		124
7.1	Summary of work completed.....	124
7.2	Recommendations for future LC designs.....	125
7.3	Ideas for future research.....	127
APPENDIX A.....		129
REFERENCES		140

LIST OF FIGURES

Figure 1 Illustration for a LEO satellite identifying access parameters [2]	6
Figure 2 Recommended flow process of antenna design showing some factors that should feed into antenna design requirements.....	16
Figure 3 Unit cell with circular slots and 3 PIN diodes (left) and the reflection loss curves for PIN states (right) [27].....	22
Figure 4 Dual band unit cell showing 5 PIN diodes and voltage inputs (left) and the phase response of the unit cell for 12GHz.	24
Figure 5 Sketch of the unit cell (left) showing MEMS feed network and patch and simulated vs. measured reflection coefficient for a 16x16 array	25
Figure 6 FET reconfigurable aperture concept (left) and example array network (right).....	27
Figure 7 Illustration of LC rod order as temperature increases transitioning the material from a solid to an isotropic fluid.	28
Figure 8 Ashby chart of LC molecules and their tenability and loss tangent values. [46]	30
Figure 9 Phase shifting approach using LC channels and a MEMS switch to provide phase delay in a feed line [47]	31
Figure 10 Reflectarray utilizing LC elements and a single LC cavity. [48]	31
Figure 11 Rectangular waveguide resonator [48]	34
Figure 12 Inductive Coupled Ring Resonator with LC material as a microstrip-line substrate. [54]	35
Figure 13 Liquid Crystal director orientation change with applied DC voltage[22]	37
Figure 14 Modeled response shift of LC cell under various DC bias voltages [22].	39
Figure 15 Measured response shift of LC cell under various DC bias voltages [22].	39
Figure 16 CST Reflection loss plots of circular patch with varying permittivity.	40
Figure 17 CST phase plots of patch with varying permittivity	41
Figure 18 COMSOL plot of unit cell with and without DC bias applied.	42
Figure 19 Array setup for a normal (left) and steered (right) configuration.	44
Figure 20 Required plate phase distribution for a culminated beam in the normal (left) and steered (right) configuration.	45
Figure 21 Required element phase distribution for a culminated beam in the normal (left) and steered (right) configuration.	45
Figure 22 Reflectarray considering element phase control limitations.	46
Figure 23 3D samples printed for thickness verification procedures and for various build orientations in 3D printer: horizontal (left) and vertical (right).	50
Figure 24 Confocal Fabry-Perot Resonator	55
Figure 25 Profile of Fabry Perot Resonator showing focused Gaussian beam.....	56
Figure 26 Inspection Beam Size given mirror spacing (top) and frequency (bottom).....	57
Figure 27 Mode observation and isolation in open air FPR and with the addition of Teflon (lower right).....	59
Figure 28 Open chamber (blue) and Teflon sheet (red) measurement in FPR setup.	59
Figure 29 Open Chamber measurement with thermal extremes from air conditioned room (72F-75F).....	61
Figure 30 Phases of LC under pressure and temperature [46].....	64
Figure 31 Nematic LC elastic properties with increased temperature [63].....	65

Figure 32 Nematic LC viscosity properties with increased temperature [64].....	66
Figure 33 Nematic LC dielectric anisotropy trend with increased temperature [65].....	67
Figure 34 Split ring resonator on kapton layer exposed to 15 sec 1W pulse in a X-band waveguide [69]. The incident E-field, E, can be assumed from the below equation as ~ 1302 V/m.....	68
Figure 35 (a) temperature profile of square ring resonator under incident RF pulse, (b) absorption curve showing maximum absorptivity at unit cell resonance, and (c) temperature plot with time of RF exposure.	69
Figure 36 (top) Survey of amplifiers commonly used for GEO satellites[71] and (bottom) common power output of communication amplifiers [72].	71
Figure 37 Refellectarray with horn fed by high power transmitter resulting in excessive thermal loading $>0.5\text{W}/\text{cm}^2$	72
Figure 38: Phase shifter temperature test setup	74
Figure 39 Sample setup and patch arrangement	75
Figure 40 Return loss and resulting phase shift for the 2x1 LC reflector with BL006	76
Figure 41 Phase delta over frequency range at various test temperatures	77
Figure 42: Measured phase shift as a function of temperature	78
Figure 43 Optical microscope measurements made before (left) and after (right) thermal-vacuum testing where images show printed (top) and paint (bottom) effects.	80
Figure 44 Antenna sample (7F) reflection parameter over time after vacuum exposure.....	82
Figure 45 Chemical Structure of Kapton	87
Figure 46 Lithium-drifted Si charged Particle Detector, Baltic Instruments SPD 200-5, measurement of Sr-90 source.....	89
Figure 47 Sr-90 illuminated spectrum compared to other sources for space measurements	90
Figure 48 Printed substrate before (left) and after (right) Sr-90 exposure illustrating the manifestation of defects. The top picture is for between printed layers while the bottom shows a single layer with increasing defects.	91
Figure 49 Pictures of Cobalt (left) and X-Ray (right) setup for the exposures on the samples.	93
Figure 50: Material Characterization setup; Dielectrics Tested: Rogers RO3003 (Ceramic-filled PTFE), Rogers RT/duroid 5880 (Glass woven PTFE), Rogers TMM3 (Thermoset ceramic)	94
Figure 51 Modeled dielectric LC Profile (left) and the illuminated spot beam creating a charge deposition within the substrate (right)	99
Figure 52 Modeled dielectric charge density (left) and resulting field vectors (right) 2.5 seconds after illumination.....	99
Figure 53 Modeled dielectric charge density (left) and resulting field vectors (right) 30 seconds after illumination.....	100
Figure 54 Modeled dielectric LC Profile (left) and the illuminated sheet beam creating a charge deposition within the substrate (right)	101
Figure 55 Modeled dielectric charge density (left) and resulting field vectors (right) 2.5 seconds after illumination.....	101
Figure 56 Modeled dielectric charge density (left) and resulting field vectors (right) 30 seconds after illumination.....	102
Figure 57 Custom built Jumbo chamber for simulated space exposure.....	103
Figure 58 Chamber test hardware in measurement setup	104
Figure 59 distributed electron flux from test sample used for calibrating chamber.	104

Figure 60 Standing charge on TMM3 with increased charged particle exposure.....	105
Figure 61 Discharge profile of TMM3 once illumination is removed.....	106
Figure 62 Standing charge on 5880 with increased charged particle exposure.	107
Figure 63 Discharge profile of 5880 once illumination is removed.	108
Figure 64 Layup of LC RF element used for charging tests.	108
Figure 65 Layup of LC RF element used for charging tests.	109
Figure 66 Layup of LC RF element used for charging tests.	110
Figure 67 Surface potential expected on LC element under charge exposure.	111
Figure 68 Standing normal electric fields under LC charging exposure.....	111
Figure 69 Standing normal electric fields under LC charging exposure.....	112
Figure 70 Penetration depth of electrons in Duroid showing at what energy level the electrons become fully penetrating.....	113
Figure 71 Sr-90 exposure spectrum compared to common GEO dose rates.	114
Figure 72 Return loss for LC unit cell when fully biased with/without the Sr-90 source present.	115
Figure 73 Return loss for LC unit cell when fully relaxed prior to and after biasing with/without the Sr-90 source present.....	116
Figure 74 Percentage of difference between radiated and non-radiated voltage states.	117
Figure 75 LC feed line slot array with patch radiator setup.....	119
Figure 76 Electric Fields generated by 30V biasing charge on LC feed line.....	120
Figure 77 Corresponding voltage potential in LC cell.....	120
Figure 78 Electric Fields generated by 30V biasing charge on LC feed line in the presence of a low energy charge deposition.	121
Figure 79 Corresponding voltage potential in LC cell in the presence of a low energy charge deposition.....	121
Figure 80 Electric Fields generated by 0V biasing charge on LC feed line in the presence of a low energy charge deposition.	122
Figure 81 Corresponding voltage potential in LC cell in the presence of a low energy charge deposition.....	122

LIST OF TABLES

Table 1 Reconfiguration comparisons showing great (green), ok (yellow) and poor (red) characteristics.....	21
Table 2 Printing Thicknesses Of Varying Oriented Samples Pre-Cure	52
Table 3 Printing Thicknesses Of Varying Oriented Samples Post-Cure	53
Table 4 Dielectric Measurements of iPro 8000 printed ABS	61
Table 5 Coefficient of Thermal Expansion for primary reflectarray parts (ppm/°C).....	72

CHAPTER 0: MOTIVATION

Significant research is conducted on novel concepts to control the electromagnetic spectrum every year. These new methods are then reported to have applications for various fields from personal hand-held electronics to deep space communication. However, most of this research is done in the realm of modeling and low fidelity lab simulations. Testing antennas concepts to endure in the operational environment is sometimes seen as much of a complex task as the initial development, or in some cases it exceeds the capability and resources of the researcher to adequately explore the physical phenomenon. This is particularly the case when it comes to space apertures due to the difficulties in adequately capturing and understanding the various complex space environments.

Designing an antenna for space utilization is a daunting task that requires expertise in mechanical, aerospace, thermal, and space weather backgrounds. Several resources exist for the space community to aid in the design process of the most basic antenna platforms. With the advancement of materials and manufacturing processes, the applied EM community is seeing the emergence of unique metamaterial antennas, phase shifting elements, and printed antennas. Many of these new ideas have even been proposed as ideal candidates for space. The Air Force (AF) is always looking for improvements to current systems and communications is often one of the more highly emphasized areas due to the primary function of AF space assets. Researchers are looking at how phased array functionality can be achieved without the traditional hardware

burdens encountered with the $N \times N$ element array approach. Reflectarrays seems to be just one possible approach.

Among the various designs implemented in reflectarrays, in the literature, liquid crystal substrates seemed the most appealing to investigate based on various claims made to its robustness to space radiation based on Laser Communication work. The author was motivated to study this technique and assess the feasibility of liquid crystals for tuning reflectarrays in a harsh space environment. Given the resources available, it seemed feasible to develop various reflectarrays concepts using standard building approaches along with 3D manufacturing techniques and different liquid crystal mixtures and expose them to space simulated conditions and characterize the material change and impact on unit cell performance.

Ideally, such an effort would contribute design practice considerations to be made by future researchers creating antenna array solutions for space using molecular phase shifting media or other novel approaches. While there is a collection of resources available for this on traditional antennas, there is very little available for this new era of antenna design and failure to develop these technologies without the correct attention to detail for the complex environment will result in poor technology transitions and wasted engineering time.

CHAPTER 1: INTRODUCTION TO SPACE TERMINALS

Antennas are utilized in just about every application that requires transfer of information via electromagnetics (EM) waves. These components are used to both capture and transmit frequency dependent EM waves and couple that energy back into a useable electrical signal for processing. They are found on our persons, on our vehicles, in many of our appliances, and even toys. Each application requires specific design considerations to ensure that the antenna is sufficiently robust to the operational environment and expected duty cycle and power levels for the system. As the demands of the system increase, so does the level of complexity required for a practical antenna design. While many of the antennas we come into contact with on a daily bases are modular or cheap to replace, many of the antenna architectures we rely on are not.

Advanced applications, both terrestrial and space, are typically focused on communications, navigations, and sensing [1]. The most commonly recognized architecture is likely the communication system. These platforms reside in all orbital planes and provide military communication, digital audio broadcast, television, and broadband services. Communication platforms are used to relay data between 2 or more sites and are categorized based on their network setup. This setup can be performed as one-way or two-way links between single or multiple users. These link points can be stationary (like a cell tower) or mobile (like an automobile). Each configuration will have specific design impacts on antenna solutions. If there are only two static points communicating, the optimal scenario may be a dipole antenna, but if there is one broadcasting station communicating with multiple users on the ground and in the air all moving and using multiple channels while under threat of jamming, the more optimal

solution begins to drive toward phased arrays or gimballed parabolic reflectors. This is especially true for any broadband service. Additionally while single users may be able to maintain a constant link, multiple users may have to rely on predictable operation and a high degree of schedule awareness implementing strategies such as the Time Division Multiple Access (TDMA) method to handle sharing of resources. The chosen antenna must also be able to keep up with these scheduling approaches. If a gimballed, high-gain antenna is designed for a mobile system that may need to point to targets separated by an angular distance beyond the antennas beam width and relying on TDMA scheduling, it will not be able to slew in time to meet both targets millisecond span transmission windows. This operational reality imposes limitations on certain antenna designs and architectural approaches.

Navigational antenna platforms are focused on location awareness and are used on a wide array of applications from complex satellites for precise position and pointing requirements to mail package tracking in route. These antennas act as receivers for one or more Global Navigation Satellite Systems. There are four entities that provide, or are developing, this service through a constellation of satellites that constantly transmit unique signals used to characterize the receiver's location. Antennas can be designed to work with GPS (USA), Galileo (Europe), Glonass (Russia), or Beidou (China) and typically require multiple receivers. Researchers in Taiwan [2] have come up with an approach that only uses one reconfigurable receiver to listen to all four systems. By applying a reconfigurable mindset, researchers shift complexity away from the backend electronics and transition it to the antenna where constantly evolving material and manufacturing developments allow front end aperture advancements.

The final class of antenna platform can be grouped into sensing systems. These can be passive listeners detecting stray emitted signals or active systems, like radar, sending out a pulse and characterizing the reflection for relevant data. While many terrestrial applications may have to deal with scattering issues from nearby objects, the ground, the atmosphere, space platforms are typically less impacted and benefit from mostly line-of-sight (LOS) links. However, space components have to be designed for a wide array of operational requirements and harsh conditions.

Space RF terminals require an additional set of considerations that many terrestrial applications do not. Propagation distances are among the first things to consider when developing satellite links. With orbits for typical planetary satellites ranging from 200km to 36000 km, free space loss can quickly exceed 200dB as operating frequencies increase beyond X-band up through E-band. This inverse square law phenomenon only gets worse as we consider deep space communication and sensing systems beyond Geosynchronous Earth Orbits (GEO). Additionally, access time needs to be considered. Satellites in GEO synchronous orbits, like satellite TV providers, maintain a fairly constant location for simple pointing requirements and are available essentially as scheduling allows. It is possible to see the entire profile of the Earth as well with 3 systems and achieve nearly full global coverage. LEO satellites, however, must maintain high escape velocities to prevent deorbiting resulting in a system that circles the Earth multiple times per day (~ 1 orbit / 90 minutes) leading to short access times, as little as 15 minutes [3]. Add to this the fact that many satellites share ground terminal links and that time slot can be reduced to as little as 2 minutes. Additionally, the beam width of a LEO system does not cover the entirety of the access area nor does the access area cover all of the Earth's side profile as

seen in Figure 1. This results in a need for large constellations of satellites to cover the globe or just provide constant access to a critical ground points. Knowledge of the pointing and steering requirements can drive overall system design. Mechanically steerable designs require compensating reaction wheels and torque rods to mitigate slewing forces. The size of reflectors will limit the rate at which a satellite may slew and therefore may limit the system's time spent radiating in a desired direction. Electronically steerable arrays (ESAs) allow non-mechanical steering by driving arrays of feeds in arrangements where both magnitude and amplitude are adjusted to collectively radiate in a desired direction. This approach allows for instant pointing and adaptive radiation patterns with little mechanical influence on the system.

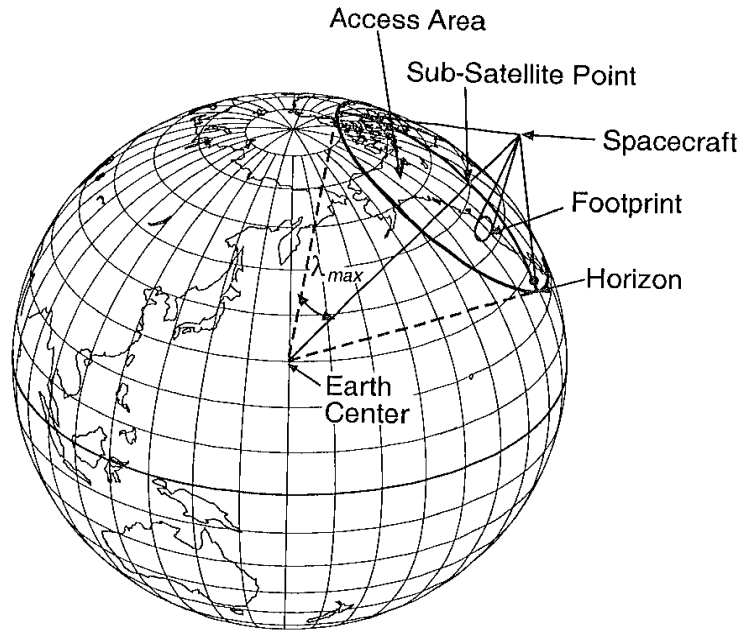


Figure 1 Illustration for a LEO satellite identifying access parameters [2]

1.1 Mechanical Design Considerations For Space Terminals

Antennas designed for space missions must be structurally robust enough to endure the launch phase. For a spacecraft bus and structural load carrying assemblies, the intense dynamic vibration loads applied by the thrust of the rocket, the acoustic loads imparted into the cavity as the rocket traverses the atmospheric layers, and the shock loads transferred through the structure as separations take place to shed spent segments must all be factored in the design during the modelling stage. A great deal of design goes into isolation systems to minimize dynamic loading on the spacecraft's appendages (solar arrays, antennas, deployable structures, etc.) for the system once in space so that pointing requirements can be maintained despite system disturbances from thermal changes or mechanical vibrations. The Falcon 9, which is the platform for SpaceX, launch experiences acoustic loads up to 140dB at frequencies up to 2 kHz [4] which can couple with the resonance of structures causing damage. Any aperture designed for space must therefore be sufficiently stiff so that no loss of function or damage occurs as deformations from these events occur. This is validated on hardware through the application of quasi-static loads in the form of single axis tensile/compressive loading to verify load bearing elements maintain required shape after maximum expected loads and vibration tables which apply dynamic responses to structures which may resonate components like solar arrays and reflector dishes.

Thermal cycling is also performed on components to make sure there is no detrimental thermo-elastic distortions occur. The thermal impact on mechanical design is very significant for aperture design. On the ground, antenna designers may use gold, silver, or more commonly, copper for traces and radiating elements. However, these

materials won't work well in high powered RF applications in space where temperatures can exceed 100°C. Other thermal design issues are discussed in the following section.

When antennas are made for space, precise manufacturing and inspection is needed to verify no defects exist. Composites, used often for reflectors and deployables due to their strength and low thermal expansion, must be properly handled to ensure no voids or volatiles (like water) exist in the layup prior to resin curing. AFRL utilizes vacuum bags and an autoclave to ensure all air bubbles and moisture are removed from parts. Ceramic Matrix Composites (CMCs) are very popular in proposed antenna design and are marketed for space use often [5,6] as they provide shape accuracy, hardness, and lightweight stiff structural bodies. The most challenging aspect of these designs is managing porosity, shape change and shrinkage that occur as the parts are formed. While these materials perform well at high temperatures, it is critical that designers verify the thermal robustness of the internal components as well. Metals, connections, liquid crystals and other items included in the CMC may not be able to handle the extremes that the CMC can, requiring special thermal management designs to remove heat from the component to avoid mechanical strain and failure. These strong RF-Thermal-Mechanical coupled structures can drive design costs for complex apertures.

Overall, designers are encouraged to consider lightweight, stiff, and dimensionally stable structures for spacecraft designs that can handle the extreme launch conditions and thermal induced loads on components.

1.2 Thermal Design Considerations for Space Terminals

From the author's experience, it has typically been seen that many design problems come back to thermal management for most spacecraft components. This is rooted in the fact that software is behind almost every stage of initial design and modeling errors propagate through the entire design and assembly. Antennas are certainly not excluded from this fact as these reflectors, booms, and arrays are exposed to the space environment more so than many other space systems that may reside inside the vehicle bus and benefit from the structural protection for many issues. Additionally, thermal design must be considered to meet both the operational environment and platform (if the platform is a transmitter) requirements. The content of this section is largely based on the author's professional experience and exposure to satellite systems. For more in depth details, readers are encouraged to utilize available literature [7].

The first level of analysis on antenna elements is a 2-node thermal model where the first node is the side facing the Sun and the second node is facing deep space (-270°C). The Sun heats spacecraft and the intensity depends on the distance the object is from the sun. For near Earth objects the solar flux is approximated in practice to about 1350 W/m^2 . The amount of heat exchanged is based on the solar absorptivity and infrared emissivity of the surface layers and the conductivity of the region between these layers. As the element takes in heat it radiates heat back into space in all directions. This is the only way for objects to dump heat in space. However heat can be managed on the structure through the use of different conductive technologies to reduce the amount of thermal energy that a particular component has to store for radiating. Additionally, materials and interfaces are designed with near-zero coefficient of thermal expansion (CTE) materials or different

materials with low CTE mismatches such that thermal variations do not impose a mechanical load in the substrate or at critical interfaces. One of the biggest challenges with conductive transport is maintaining an isothermal structure to control deformation. Convective radiation is more risky to use in space and requires shielded pressurized chambers to protect the cooling medium (like the air in International Space Station). For antennas, this would require a pressurized radome which is unpractical.

Micro Meteoroid Orbital Debris (MMOD) is the largest source of concern for this approach as punctures release the cooling medium and catastrophically impact thermal performance. This method is not foreseeably practical for antennas due to the need for the aperture to reside on the exterior of the spacecraft. The most common thermal management philosophy is to blanket the spacecraft in solar rejecting materials, assuming the electronics on board provide sufficient heat generation. Prospective antenna designers should be considerate of these technologies in their design process to properly understand how beam parameters may be affected.

Radiative properties are tailored through surface layers and controlling exposure. This can be done with paints, tapes, occluding structures (baffles or shades), or multilayer insulation (MLI). These materials are used to influence the emissive and absorptive properties of the external surface and control how much heat is exchanged to and from the surrounding environment. MLI is different in that it insulates the structure blocking solar heating, with the drawback of preventing any radiation of heat to deep space. This usually raises the thermal balance of the structure as less heat can be dumped to space. Occluding structures, like a radome, are effective at preventing solar flux on antenna elements but must be RF transparent. Depending on the method chosen for a space

antenna, there will be consequences for the systems radiator(s) which rely on a ΔT^4 between the radiating surface and deep space to dump the most heat possible in a controlled and steady fashion. While MLI may simplify appendage design and minimize thermal gradients from solar exposure and shadowing, it may require an increase in the size of the radiator to compensate for the larger heat capacity of the total structure. All heat on the antenna must be conducted to the radiator to preserve performance.

Conduction is controlled by designing in the highest level of conductivity possible and minimizing thermal bottlenecks between layers and interfaces. Each material/component interface acts as a thermal resistance. For antennas exposed to solar flux (or any hot body) the radiating element may absorb some heat, have to pass it through a dielectric/metallic substrate towards a structural backing element and then send that heat to a radiator to dump back into space. Failure to minimize the heat on the antenna may result in mechanical deformations of plate and rod elements as the component heats or cools beyond its manufactured state. When thermal bottlenecks create significant thermal differences between interfaces there is risk that fatigue or failure will occur. Material selection is critical here to attempt to utilize dimensionally stable materials with near zero Coefficient of Thermal Expansion (CTE). Structural analysis is performed on antenna elements for the worst case hot and cold scenarios as well as any worst case thermal gradient that may be expected due to pointing scenarios with casted shadows or IR flux on the antenna to ensure that these stress hot spots do not exceed plastic limits. Thermal Interface Materials (TIMs) can be used at mechanical interfaces of components to provide a ductile, highly conductive layer that contacts all surface points and compensate for mechanical surface errors generated during the

manufacturing process. Heat pipes can be used to pull heat directly from components toward the radiator. This method may be utilized on sub reflectors on a transmitting dish reflector where the sub reflector is essentially isolated from the bus and exposed to high transmit power and environmental fluxes. Heat pipes are traditionally aluminum which may interfere with beam parameters.

Antenna designers must remember that these components are likely to be exposed to the full space environment and will need to incorporate appropriate radiative and conductive technologies. Additionally, material selection trades may be required to handle the extreme thermal environment thus reducing peak antenna performance potential.

1.3 Space Radiation and Electrical Design Considerations for Space Terminals

Space RF transmission are subject to many losses between sources due to the influence of the EM environment. The polarization of transmitted waves is altered by the Faraday rotation effect when interacting with the ionosphere. The conductivity of LEO antennas exposed to impacts from atomic oxygen may result in the formation in oxides and diminished performance. Surface charge that builds up on the aperture may suddenly be released by an impact from a differentially charged particle or dielectric breakdown in the form of arcing releasing a plasma current across the structure and producing unknown anomalies. Even aging of the spacecraft may reduce the effectiveness of thermal paints, as they discolor [8], causing temperatures to rise and increasing noise figures. Additionally, the antenna must be protected from Passive Inter-Modulation (PIM) effects and multipaction [9].

PIM is the result of two or more RF sources in a system that results in noise. Many satellites utilize multiple bandwidths for various missions and these systems can create nonlinearity in the signals, especially if when these functions use the same antenna [10]. Additional PIM can occur when metallic radiating elements form oxides creating a material defect and a site for RF heating [11].

Multipaction is an arching between electrodes with RF fields on them in vacuum. When electrons impact the electrodes, emissions of secondary electrons may occur at the surface and can cause anomalies in the system or damage. The generation depends on [11]:

- Vacuum pressure $< 10^{-5}$ torr
- Applied RF voltage
- Electrode geometry and frequency
- Impurities on the material surface

This phenomenon can drive the maximum power that may be used for a particular radiating element. This will be of critical interest for the LiCRas as the two nearest electrodes are likely the patch element and the ground plane with a thin dielectric space. This will be discussed later in the design section.

Antenna designs need to consider these EM issues early on in the design phase to prevent the use of materials that change physically and dimensionally in space. RF components need to be optimized to minimize the number of interfaces (tuning screws, flange mates, etc.). Additionally, the layup of complex antennas that utilize arrays of

elements must consider damaging multipaction that may occur between electrodes which may drive layout configurations.

1.4 Traditional Space Antenna Concepts

The antenna components used for space mission can be essentially generalized to five types [1]. Each type has application specific benefits and limitations. Dipole antennas are simple antennas to include on a spacecraft and offer linear polarization omnidirectional radiation. This antenna would likely always have reduced bandwidth and transmission rates over high gain apertures making it the preferred choice for telemetry data. This is low rate data from satellites used to determine attitude and control, as well as, possible health and status data. Dipoles would be useful in events where control was not in effect and pointing uncertain. However, polarization losses are to be expected as these antennas are linear polarized requiring ground terminals to account for polarization rotation from traversing the ionosphere as well as ground terminal selection. This is likely handled by using a cross dipole ground terminal. The next step up from the dipole would be the helical antenna. The winding of the wire element creates a broadband, circularly polarized element that can be designed to radiate with a broadside or end-fire pattern. Arrays of these are used on GPS satellites to create broadband pattern for carrying multiple frequency channels. These are also used for lower data rates.

Horn antennas are used to create wide beam coverage or are coupled with a reflector dish. Their beam profiles are determined by the aperture geometry and field distribution. Polarization is based on the mode generated in the horn. These apertures are used for high power transmissions but suffer from asymmetric field patterns and beam diffraction. This is mitigated with corrugated walls to provide capacitive reactance [12]. Reflector

antennas are almost an extension of horn antennas. While other feeds may be used, the most common is a horn with Gaussian beam characteristics [13]. Reflectors are the dominant high data antenna approach due to its high gain and design potential to meet a variety of complex radiation patterns. These antennas are subject to spillover, illumination, blockage, and surface geometry losses. The combination of feed horn and reflector can be orientated in multiple ways that involve in/off axis orientations and direct/sub-reflected illumination on the main reflector. Various shapes of reflectors exist depending on the application. These apertures can be expensive to manufacture to ensure no manufacturing defects occur on a large surface.

The final type of element is the patch antenna. This patch element is designed with dimensions defined by the operating frequency and bandwidth. While these elements are more narrowband than reflectors, research has shown broadband patches and configurations that would meet many operating bands. These elements are however more limited in their ability to tolerate incident power. While proper design may allow a micro-strip radiator to handle over 100 watts [14], multipaction between the layers would result in breakdown between the layers [15]. Printed arrays of these elements are used to balance gain and power levels. This approach can be utilized with multiple approaches to create tailored or reconfigurable beam forming. Of most interest for this research was the application of reflectarrays which will be discussed in the next chapter.

1.5 Engineering Philosophy

From this section, the reader should note that the design of space apertures is a multidisciplinary task requiring early understanding of the limitations that will be imposed on an antenna due to launch vehicle design requirements, operational thermal/radiation

extremes and the specific antenna functional requirements. Many antenna developments proposed for space typically focuses on the antenna requirements alone and then addresses the rest of the design challenge as funding is provided. This hostage situation makes for an iterative design process where RG and electrical design of the antenna must be redeveloped as each new set of requirements are defined. This makes sense for prototypes and demonstrators but for serious space inquiries the design process needs to be flipped. The figure below shows some of the considerations and requirements that should be defined before any tasks on the antenna design are performed.

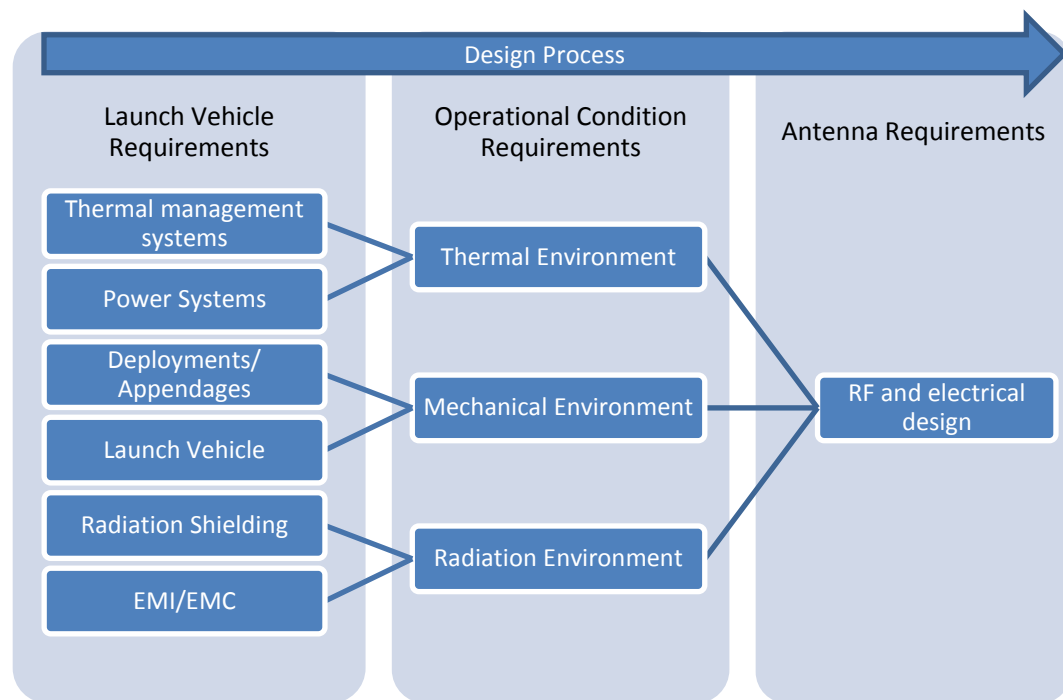


Figure 2 Recommended flow process of antenna design showing some factors that should feed into antenna design requirements

The rest of this dissertation will focus on the development of a Reflectarray with patch elements and a reconfigurable substrate taking in various space design considerations and factoring in those scenarios into the design process showing how

performance can be expected to change. The final contribution should be a guide to space antenna design for next generation reconfigurable antennas and a proposed reconfigurable liquid crystal reflectarray design.

CHAPTER 2: RECONFIGURABLE REFLECTARRAYS

2.1 Introduction

A reflectarray is essentially a reflector that is made of an array of radiating elements that are illuminated by a feed source and reflect that energy [16]. The earliest designs were arrays of dipole lenses reported in 1958 [17] but the current approach uses printed patches. Some researchers have even utilized 3D manufacturing to create novel reflectarrays for high power applications [18]. Whereas a parabolic reflector relies on the curvature to create a plane wave from the feed source, a reflectarray is flat and corrects phase delays at the reflecting element. Each element in the array is at some length, S , away from the feed. As the wave propagates to each element, there is some spatial phase delay, ΔS , that separates adjacent elements that are separated by some fraction, d , of the operating wavelength, λ . This fundamental description of phase change between N elements can be put into the form;

$$\Delta S = (N+d)\lambda \quad 1$$

The phase difference is corrected at the adjacent element so that the reflection in the far-field becomes a plane wave. The change in phase between two elements is corrected by designing in phase delay at each element. The amount of delay is based on the desired far-field pointing vector and can be determined using phase synthesis techniques [19].

The fundamental limit of this approach occurs when the number of elements grows so large that the phase difference between edge elements approaches 360° . This excursion error can be compensated for by utilizing a larger focal length/diameter ratio to allow the main beam to have less node to node distance change, reducing the array size to stay below 360° , or add a time delay line to the patch [16]. Thales Alenia Space [20] and

NASA/JPL [21] have both created piecewise flat reflectors that are assembled with angles to make a pseudo-curved apertures and allow for a larger array to avoid this problem.

The other noted problem with reflectarrays is the bandwidth being limited to less than 10% based on traditional patch designs [22]. However the author would dispute the narrowband performance to be a limiter as many satellite terminals split transmitter and receiver apertures and that the academic community has been developing wide band patch designs that could be implemented into reflectarrays [23]. These types of patches trend away from tradition squares and circle and utilize genetic algorithms to optimize complex topologies that match multiple desired frequency ranges. However, if we look at traditional Satellite terminals like AEHF that utilize phased arrays, it can be found that they only operate with a 5% bandwidth [24].

While the earliest developments were static arrays, it was conceived by Dr. Encinar and Dr. Huang [16], that one could add a phase shifter to the time delay line to create a low power alternative to phased arrays by getting rid of the dedicated amplifiers that are used to feed each element or subset network in a traditional phased array. This concept sparked a wide array of research looking into advanced reconfigurable concepts that could be used to tune a reflectarray. Reconfiguration can be applied to an antennas frequency, polarization, and/or its beam pattern.

2.2 Review of Previously Designed Reconfigurable Reflectarrays

The function of a reflectarray element is determined by its EM resonant properties, which are controlled by the geometry of the patch and cavity, and the material selection

which defines its conductive and dielectric properties. To make an element reconfigurable, one must change the electrical or material properties. This can be done through electrical, mechanical, optical, or molecular means. Electrical methods of tuning would include: RF-MEMS, PIN diodes, and Varactor diodes. Optical methods utilize photoconductive materials that change conductivity based on interaction with light and are similar in principal to PIN diodes that function as binary variable elements. Mechanical changes would include shape altering techniques like shape memory alloys and material changes in this case covers changes in material properties as seen in ferrites and liquid crystals [25]. Each approach will have performance limitations and applications best suited for it. While there may be a multitude of methods to perform this function, the following review is based on the most cited techniques in available literature. The below table is a generalized trade between the following reconfiguration methods based on input from the cited literature collected over the next few sections. It should be noted that manufacturing processes are constantly evolving and new materials may emerge that go against the provided table. Readers should investigate new technologies that may have emerged recently that show improvements to current poor performance parameters. Ultimately, there is never one solution that is the best solution for all applications. Instead, each method must be considered based on the design requirements and mission parameters.

Table 1 Reconfiguration comparisons showing great (green), ok (yellow) and poor (red) characteristics

	Switching speeds	Switching power (mW)	Isolation	Loss (dB)	Cost
PIN Diodes	nanoseconds	high	high	low	low
Varactor	nanoseconds	negligible	low	high	med/high
RF MEMS	microseconds	negligible	Very high	low	medium
FETs	nanoseconds	negligible	medium	medium	high
LCs	milliseconds	negligible	medium	medium	low
Shape	milliseconds	high	medium	low/med	high

2.2.1 Reconfiguration Using PIN Diodes

A PIN diode is semiconductor with a ‘p’ type and ‘n’ type doped region surrounding a near ‘intrinsic’ region that switches states of being a good or poor conductor based on sufficient biasing. This diode only has two states with no tunability. Unit cell designs that incorporate this device are typically closing circuits to change the conducting path of the reflectarray element and thus change its radiating properties. One concept recently published shows polarization reconfigurability by coupling cross dipoles with loaded diodes to control vertical and horizontal reflection coefficients [26]. Researchers have solicited one array concept for space antenna functionality at X-band frequencies by adding geometric gaps to a square element that are closed with the use of PIN diodes to change its resonant topology [27]. An illustration of the patch with diode state reflections can be seen below.

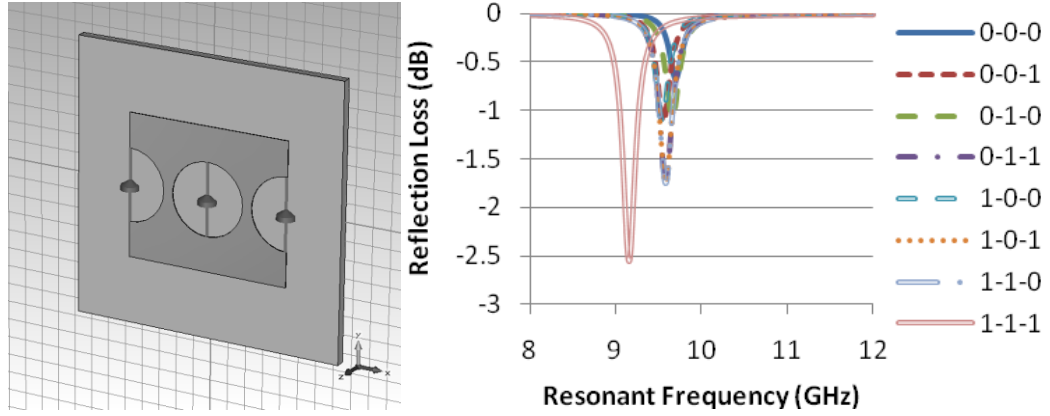


Figure 3 Unit cell with circular slots and 3 PIN diodes (left) and the reflection loss curves for PIN states (right) [27].

While no space worthiness testing or consideration was reported they did design in redundancy by refining the design to operate at two frequencies and share PIN states such that a failure of one diode does not allow a functional failure of the array. This feature is critical for space systems where maintenance is not feasible and missions can greatly exceed 10 years approaching 20 or more. Other research efforts were less concerned about redundancy and more about power/thermal management. In such a design, optimization is performed on an $N \times N$ array of elements to create a Fresnel reflector where patches shift between 0 and π radians. Researchers identify the steering values and identify similar state patches between angles. Doing this approach for a 15×15 array going from 0° - 45° identified that only a quarter of the elements needed tunability saving potentially 74% power consumption and decreased component complexity [28]. However, this design was proposed for a mobile aerial platform that would likely need far more than two pointing configurations. Many GEO platforms may have predetermined spot beams that may make such an approach an attractive optimization

approach. While, PIN diodes are fast, they require power and biasing lines to change conductive states, meaning more system resources and thermal loads to manage.

2.2.2 Reconfiguration Using Varactor Biasing

Varactor diodes utilize applied voltage to apply phase change in the form of varying capacitance. Unlike a PIN diode that is binary in function, varactors can have a range of phase shift possible. This simplified illustration of this, and other approaches, is an LCR circuit where tuned capacitance changes resonance. Researchers in Egypt [29] have shown a 13GHz reflectarray with 23dB gain that utilized a single varactor diode between a 'C' patch (basically a split ring resonator) to scan from 0° - 75° and operating with 28% efficiency. Diodes were controlled from behind the ground plane using Digital/Analog Converters (DACs) and RF Chokes. An RF choke essentially allows a circuit to pass a low frequency DC current while blocking any high frequency signals from interfering with the line. More elaborate designs have been designed combining a 12 and 14 GHz cross dipole and split-ring element collocated together using five varactor diodes and two biasing lines to independently control the phase shift for each frequency [30]. Although this approach is still in the element design stages, such an array would allow for two separately steerable bands and allow the reflectarray to act as a transmitter and receiver in the same footprint. The patch element and its phase response are shown in the following figure.

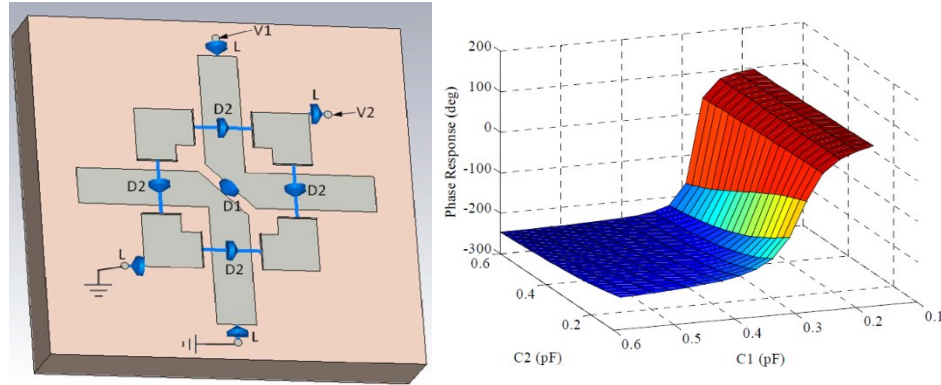


Figure 4 Dual band unit cell showing 5 PIN diodes and voltage inputs (left) and the phase response of the unit cell for 12GHz.

Other unit cell designs have been created that utilize varactor diodes and amplifiers to boost gain by 12 dB [31]. This design setup would also be useful even at smaller magnitudes to compensate large steering angles for elements that would otherwise have decreasing gain as angles trend toward 60° . One of the issues with these varactor diodes is that as an electronic device it may require radiation hardening to survive in space, which is commercially available, but at an increased cost [32].

2.2.3 Reconfiguration Using MEMS

Micro Electro-Mechanical Systems (MEMS) are micron scale machines printed with semiconductor processes to perform sensing or mechanical functions. For the purpose of reflectarrays, MEMS are used as switches to close circuits comprising a patch element to change the resonant properties. Researchers have developed MEMS based reflectarrays for W-band frequencies to perform steerable imaging that can be designed and manufactured on a single wafer allowing for quick packaging and minimum handling/assembly, and is shown in the graphic below [33].

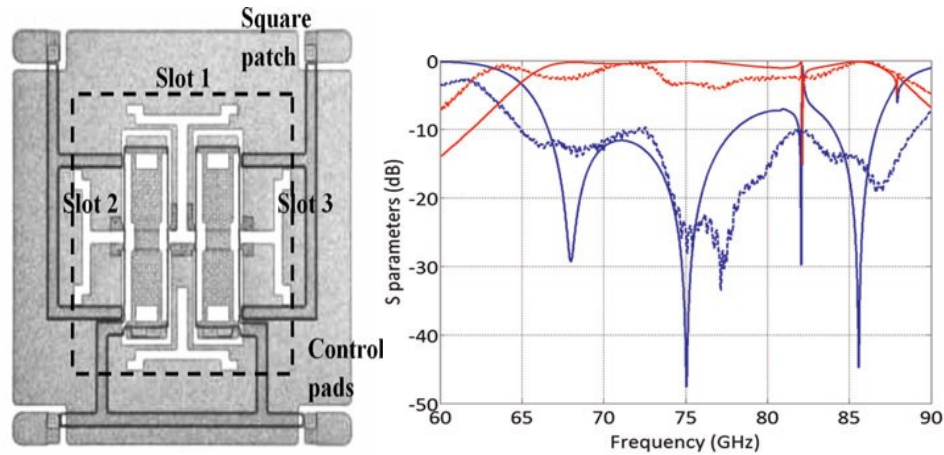


Figure 5 Sketch of the unit cell (left) showing MEMS feed network and patch and simulated vs. measured reflection coefficient for a 16x16 array

UCLA researchers created a microstrip element that utilized MEMS to change the variable length in the ground plane enabling a 150° phase and minimal loss of 0.4 dB [34]. While other efforts can be located about ongoing MEMS research for space, there are no readily available conclusive results showing that they are reliable enough for 20 year operational windows.

One of the concerns of MEMS is the mechanical function. Reliability of RF MEMS has been carried out for reflectarray cells that utilize these switches [35] and showed the MEMS switches should be heavily redundant to prevent phase error from MEMS failure with an eight MEMS configuration for connecting three patches across two slots accepting only one failure before signal degradation occurs. While RF MEMS with over a hundred billion cycles have been reported, they are vulnerable to hermitical packaging errors and operating conditions [36]. For space applications, the thermal extremes, radiation induced material changes, and launch environmental shock loads make it difficult to find reliable RF MEMS that can survive the external environment [1].

Universities have tried to qualify MEMS in LEO experiments, but with no long duration mission success to properly characterize MEMS functionality over the course of an expected satellite lifetime [37]. Other concerns may have to do with how the MEMS device mechanically functions at higher temperatures where component drifting may occur. All metal large contact force MEMS are being specifically designed to address these issues and may be solution for ruggedizing MEMS for harsh space environment [38].

2.2.4 Reconfiguration Using FETs

Field effect transistors (FETs) are utilized as switches for changing electrical path lengths and can be utilized for reconfigurable antennas. The transistor allows current to pass through as an electric field is applied to the gate. This diode is a bit more complicated to implement than others but operates at very high speeds. These diodes and other ferroelectric-semiconductor approaches have demonstrated various times as effective phase delay solutions and under certain low dose radiation exposure may have improved zero-field loss tangent [39]. This same design was later developed to a 616 channel array that required 25W for controlling. This particular approach that incorporates ferroelectric may be too high on power consumption as an X-band array with 1-m resolution grows to 2560 radiating elements [40]. However, other approaches are possible. Researchers have created reconfigurable aperture antennas using these devices and controlling them with photo detectors that controlled FETs that linked together radiating elements [41]. Light Emitting Diodes (LEDs) were placed behind the ground plane with a drilled hole allowing illumination of the detector which applied voltage to the FET. Depending on what FET was illuminated determined the network of

radiating elements that were fed RF current based on surface wave coupling from the feed point. This setup is shown in the following figure.

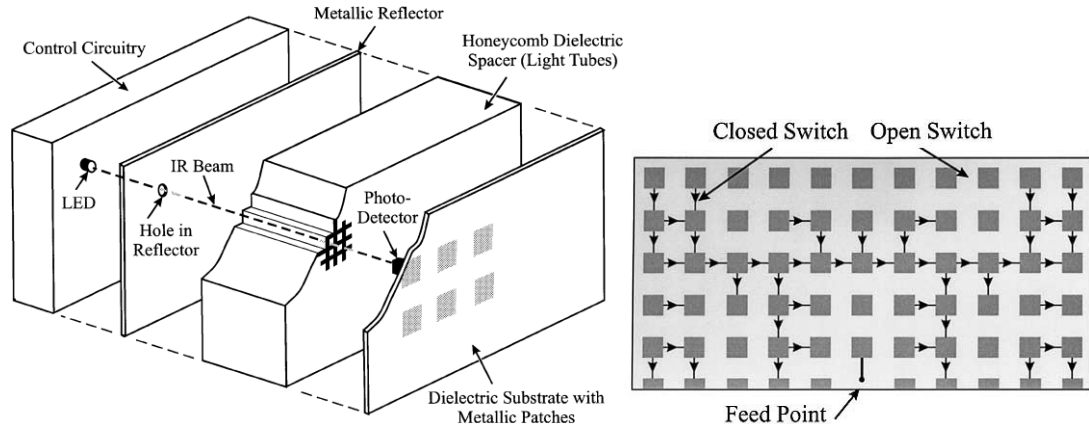


Figure 6 FET reconfigurable aperture concept (left) and example array network (right).

2.2.5 Reconfiguration Using Liquid Crystals

The final class of reconfigurability is different from the rest in the sense that it is a molecular approach. Liquid Crystals (LC) are molecules composed of carbon, hydrogen, nitrogen, oxygen or other materials and with a form that results in some level of polarity. Several LC materials are currently available and are regularly tailored to meet necessary operating temperatures. LC exists as calamatic (rods) or discotic (disks) mesophases and are named based on the molecular ordering [42]. Nematic, smectic and crystalline phases are all possible and can be tuned to various temperature ranges. An illustration of the rod arrangement for these various phases is shown below and shows that as temperature rises the LC becomes less ordered until it reaches its isotropic state where no orientating direction is maintained.

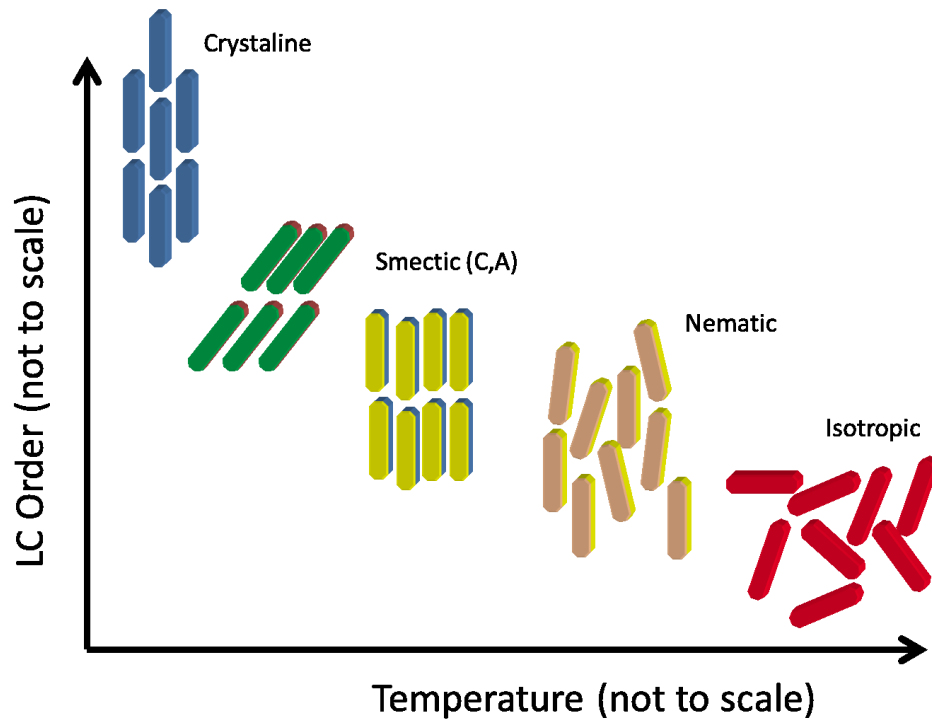


Figure 7 Illustration of LC rod order as temperature increases transitioning the material from a solid to an isotropic fluid.

If space environments are to be considered, it must be realized that operational temperature ranges for a satellite can vary significantly depending on orbit and a system can see temperatures of -200°C to $+200^{\circ}\text{C}$ or within a managed environment may be kept near room temperature based on effective removal/input of thermal loads. That being said, thermoplastic phases will need to be addressed that result from increased temperatures beyond the LC's melting point resulting in mixed phase configurations that can be difficult to control.

The most popular phase utilized in LCs for reconfigurable purposes is the nematic phase [33, 43, 44]. In this phase the rod shaped molecules have no positional order, but the directional orders of the directors are essentially parallel. The centers of gravity of

individual molecules are randomly distributed and they can freely flow. This property allows them to be easily manipulated by externally applied electric and magnetic fields. Additionally, as the temperature drops, the LC can establish a smectic phase where the order of the LC increases by defining layers within the material that can slide over one another and each layer can have a unique pointing vector. The final phase, practical for RF frequencies, is the chiral (cholesteric) phase that exhibits similar layering as smectic but now with a pitch associated to the director orientation at each layer. Depending on the temperature of the LC material, it can transition between all mesophases. The most commonly recognized flaw with this method is the mechanical nature of the transition resulting in longer switching times than other methods. However, LCs are being recognized and advertised as effective technologies in a space environment and easily implemented based on testing similar to that done at Kirtland AFB [45] for optical applications. The most commonly accepted figure of merit designated for an LC is the ratio of the tenability ($[\epsilon_{||}-\epsilon_{\perp}]/\epsilon_{||}$) with respect to the maximum loss tangent of all orientations. A recent study of various commercial LCs was assessed and compiled into an ‘Ashby’ graph as seen in the following figure showing that the ideal blend is one with large tenability range and low loss tangents. This report comes from the Merck Corporation who is well known as the industry leader in production and manufacturing of liquid crystal mixtures. The purpose of the study was to assess over 400 LC blends for understanding the molecular relationship between the compound and its dielectric properties. Worth noting from the study, increased molecular size consisting of conjugation bodies with biphenyl and terphenyl structure generally yield higher tenability over a phenylcyclohexane molecule due to increased diamagnetism of the molecules.

This is also aided by the presence of triple bonds between phenyl aromatic rings. Factors were also observed for contributing to the loss tangent based on the position and strength of the dipole moment, the fluid viscosity and the overall molecular shape. But there was not universal relationship that was able to be determined.

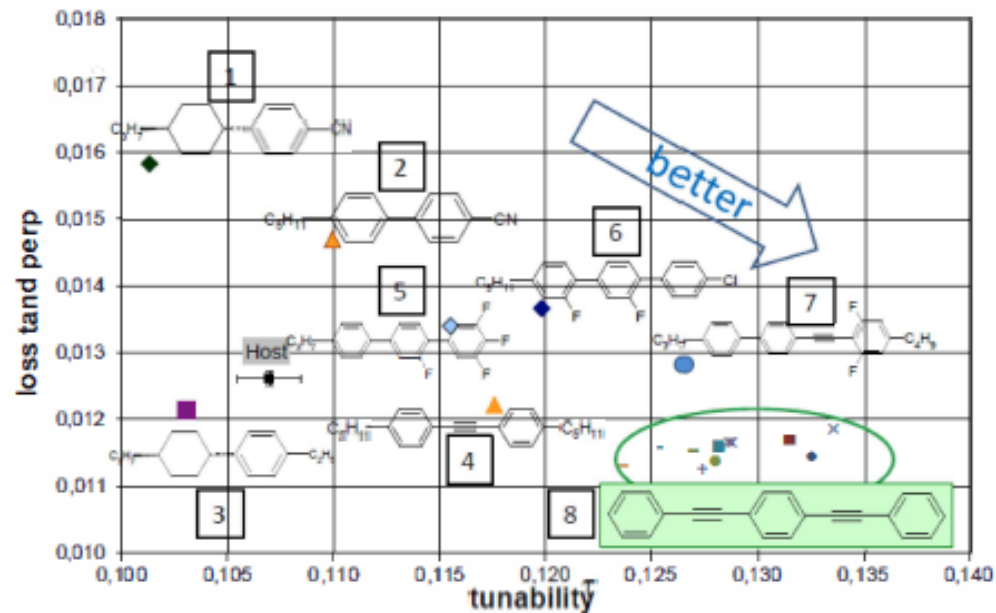


Figure 8 Ashby chart of LC molecules and their tunability and loss tangent values. [46]

Two well-developed approaches are worth noting as utilizing these materials to provide tunable phase delay. The first is from Jokoby's group in Germany where researchers have developed a hybrid phase shifter along with a MEMS switch to provide a traditional feed line phase delay approach. This type of device fits in with traditional phased array approaches and allows for more than 360 degrees of phase delay based on the intervals of LC channels added. The main concern with this approach is the utilization the real estate required to accommodate the loaded feed line in a large array with multiple feeds and the possible requirement for amplifier at the feed location.

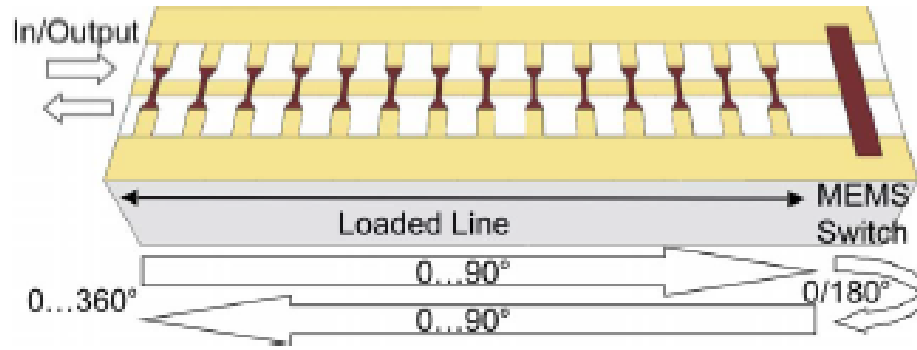


Figure 9 Phase shifting approach using LC channels and a MEMS switch to provide phase delay in a feed line [47]

The second concept is from Encinar's group and utilizes patch elements in a reflect array structure. This method has yielded -60 to -5 degree scanning. However, the main concern with this layout is the single LC reservoir that creates a single point of failure and does not allow for graceful degradation if leaks occur.

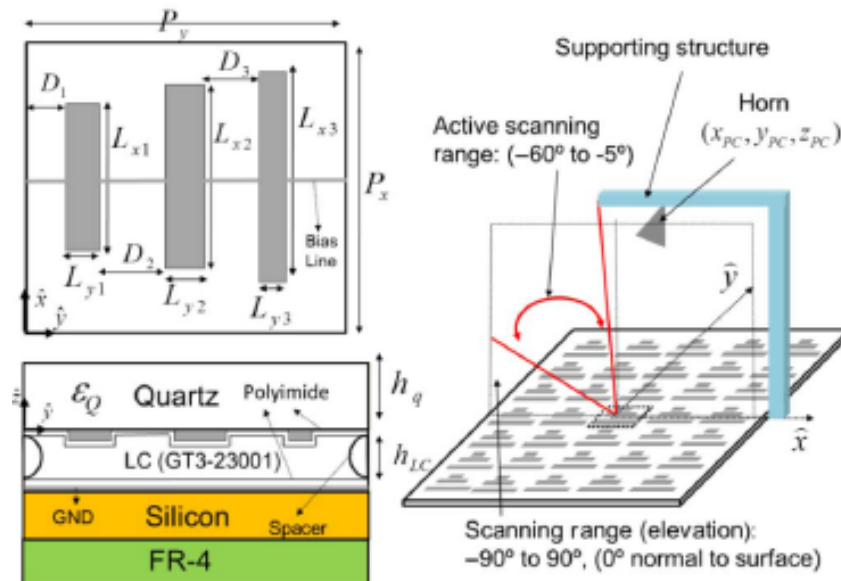


Figure 10 Reflectarray utilizing LC elements and a single LC cavity. [48]

What are needed now are studies into the space worthiness of such an approach at more relevant RF application frequencies and performance impacts on LC systems under space conditions where thermal and electrical loads may produce uncertainties in the LC or body properties and radiation may alter the substrates RF features. While it is not known if this is the optimal reconfigurable approach, it appears the easiest to consider for this research direction and the methods and testing developed herein should be translatable to other reconfigurable apertures as well.

CHAPTER 3: A LIQUID CRYSTAL REFLECTARRAY (LiCRas) APPROACH

3.1 Introduction:

Liquid Crystals (LC) are polar molecules that occupy material phases from solid to liquid but with mesophases of liquid states with varying electro-optical properties. These materials can have mesophases controlled by mixture ratios with a solvent or by temperature. The second type of LCs, thermotropic, are what are predominantly used in reconfigurable approaches and where briefly describe in Chapter 2. LCs can usually be classified based on their:

- anisotropic molecular shape (either rod like or disk like) typically provided by benzene rings,
- rigid molecule chain consisting of double and triple bonds along the director axis,
- and strong dipoles.

The molecule chains can become quite complex but usually the external groupings of elements on the backbone extremities have little importance. The basics of these materials are easily obtained in the open literature [49-52] and will not be overly emphasized here beyond the critical properties of importance for RF control.

3.2 Characterization:

In order to characterize LC components, several techniques have been developed. Mueller, et al. [48] setup a standard rectangular waveguide WR-28 and shorted both ends to make a cavity resonator. Two holes at opposite ends were made to couple apertures to excite the resonator. The cavity was dimensionally tuned to have a resonant TM mode at

30GHz. The Q and resonant frequency shift as a PTFE-probe filled with LC are inserted into the center of the cavity. This setup is seen in Figure 11 and is used to calculate the parallel and perpendicular permittivity and loss tangents.

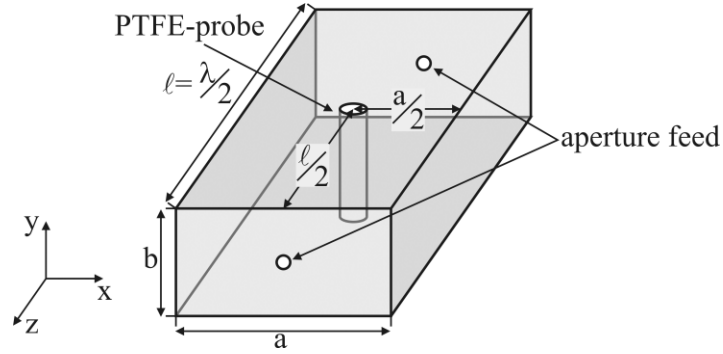


Figure 11 Rectangular waveguide resonator [48]

Utsumi, et al. [54] developed an inductive coupled ring resonator to quantify the birefringence (difference between perpendicular and parallel permittivity). The inductive ring is located above a ground plane and the LC goes in between the two. If a DC voltage is applied to the ring, the directors of the LC will align and a measurement of parallel permittivity is obtained. Removing the electric bias gives a measurement of perpendicular permittivity. The setup is seen below in Figure 12.

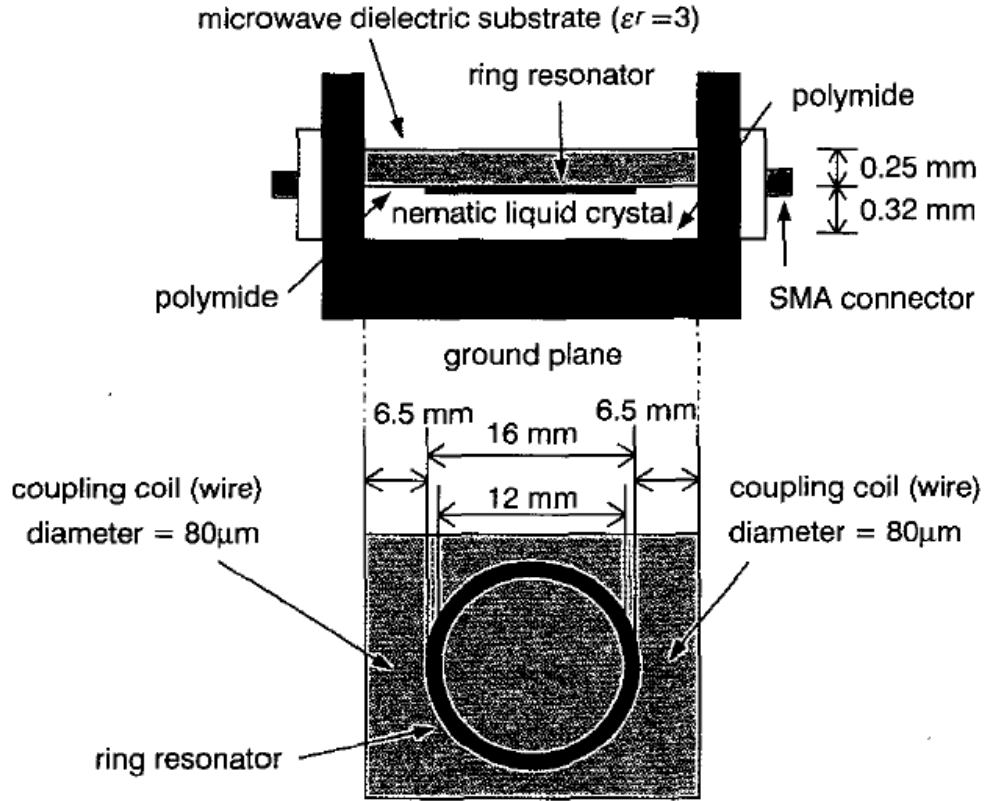


Figure 12 Inductive Coupled Ring Resonator with LC material as a microstrip-line substrate. [54]

In order to extract dielectric properties from these approaches using S-parameter measurements, consider the following using the A.M. Nicolson's method as an inverse problem [55]. Considering a Vector network analyzer provides S-parameters for reflection, r , and transmission, T , coefficients.

$$S_{11} = \frac{r(1-T^2)}{(1-r^2T^2)}, \quad S_{21} = \frac{T(1-r^2)}{(1-r^2T^2)} \quad 2$$

Once these are measured for a given setup, determine the impedance, η_s , from

$$\eta_s = \pm \eta_o \sqrt{\frac{(S_{11}+1)^2 - S_{21}^2}{(S_{11}-1)^2 - S_{21}^2}} \quad 3$$

The wave characteristic is then captured by

$$e^{-jkd} = \frac{S_{21}(\eta_s + \eta_o)}{(\eta_s + \eta_o) - S_{11}(\eta_s - \eta_o)} = Z \quad 4$$

The wave number is isolated by

$$k = \frac{j}{d} \log Z \quad 5$$

And permeability and permittivity are tracked by

$$\mu_r = \frac{k\eta_s}{\omega}, \epsilon_r = \frac{k}{\omega\eta_s} \quad 6$$

Loss tangent, $\tan \delta$, is the ratio of dielectric loss to dielectric constant and can be extracted from the network analyzer using,

$$\tan \delta = \frac{1 - |S_{11}|^2}{-2|S_{11}|\sin\varphi} \quad 7$$

where φ is the phase of the scattering coefficient.

The permittivity of a LC is dictated by its molecular orientation under an applied electric or magnetic field. Traditionally, electric field orientation is favored over magnetic fields due to the order of magnitude difference in magnitude required for a magnetic field to compete. The below figure illustrates the rod orientation in a substrate where the surface provides an anchoring orientation of horizontal orientation.

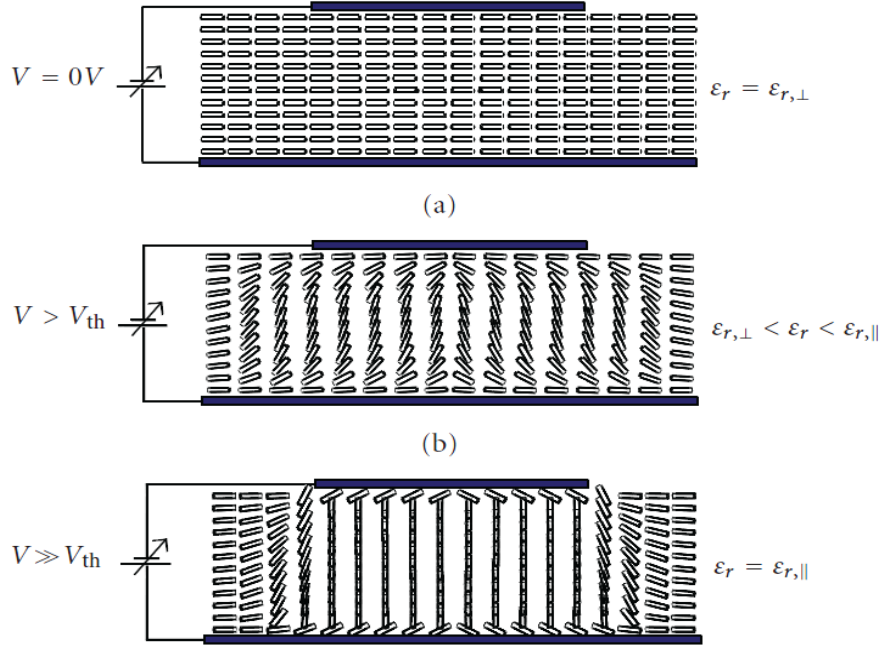


Figure 13 Liquid Crystal director orientation change with applied DC voltage[22]

One of the most important parameters of LC is the DC bias voltage, V_0 , required to re-orientate the directors in the fluid. This is controlled by the bulk fluid viscosity, k , permittivity of free space, ϵ_0 , and the delta permittivity of the LC mixture, $\Delta\epsilon = \epsilon_{\parallel} - \epsilon_{\perp}$. The perpendicular and parallel orientation permittivities can be used to define a mixtures tunability, τ . The time required for transition, $\Delta T_{on}/\Delta T_{off}$, is dependent on substrate thickness, d , viscosity, and applied DC field strength, E_{DC} . This is captured in Equations 8-10 below.

$$V_0 = \sqrt{\frac{K}{\epsilon_0 \Delta\epsilon}} \quad 8$$

$$\tau = \frac{\epsilon_{\parallel} - \epsilon_{\perp}}{\epsilon_{\parallel}} \quad 9$$

$$\Delta T_{on} = \frac{\gamma d^2}{\Delta\epsilon(V^2 - V_0^2)} \quad \Delta T_{off} = \frac{\gamma d^2}{\Delta\epsilon V_0^2} \quad 10$$

3.3 LC impacts in RF cell:

There are significant benefits for Reflectarrays in general to offer huge cost savings over parabolic reflectors. Several reconfigurable methodologies exist to allow for beam steering. LC is supported as a viable substrate approach given efforts by other entities looking at them for their dielectric anisotropy and potential space hardness. Demonstrations have been shown beyond 77GHz. Demonstrations have been primarily linearly polarized only and control has been restricted to entire columns rather than single elements. Significant challenges have been identified with the analysis and control of single elements due to simplified assumption of unit cells and lack of consideration for impact of coupling and source charge. Modeling efforts have been focused at matching lumped element representation with a simulation to allow for quick design iterations. None of the modeling has been aimed at matching to experimental result of a charged unit cell. This is shown below in Figure 14 and Figure 15 where trends and magnitudes of shifts are not repeated. Unit cells may be more effective if designed as a band pass filter where only a wideband portion of signal that captures the operational frequency over the LC tuning range was reflected. The current approach just reflects everything and applies reflection loss to cell in the form of heat. In order to change this, a RF transparent LC control layer would be needed. ITO, while conductive, may have enough transmission to work for this purpose.

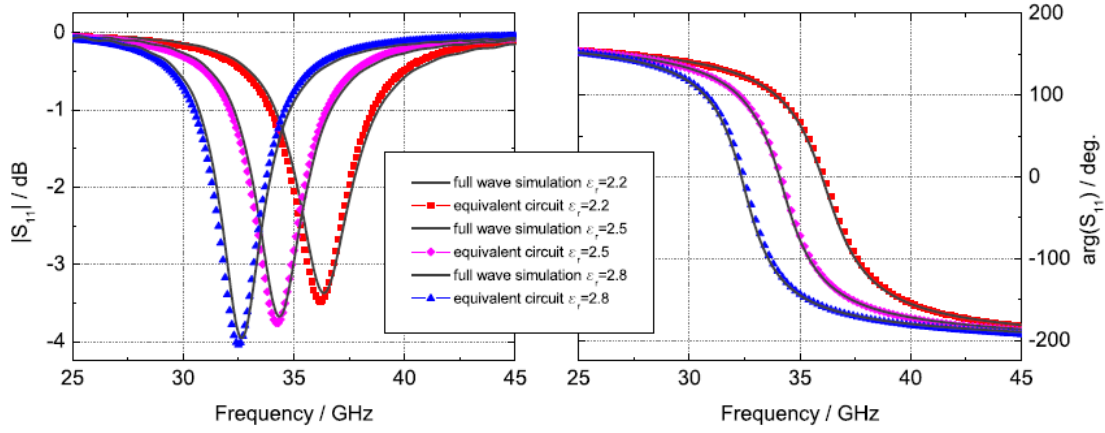


Figure 14 Modeled response shift of LC cell under various DC bias voltages [22].

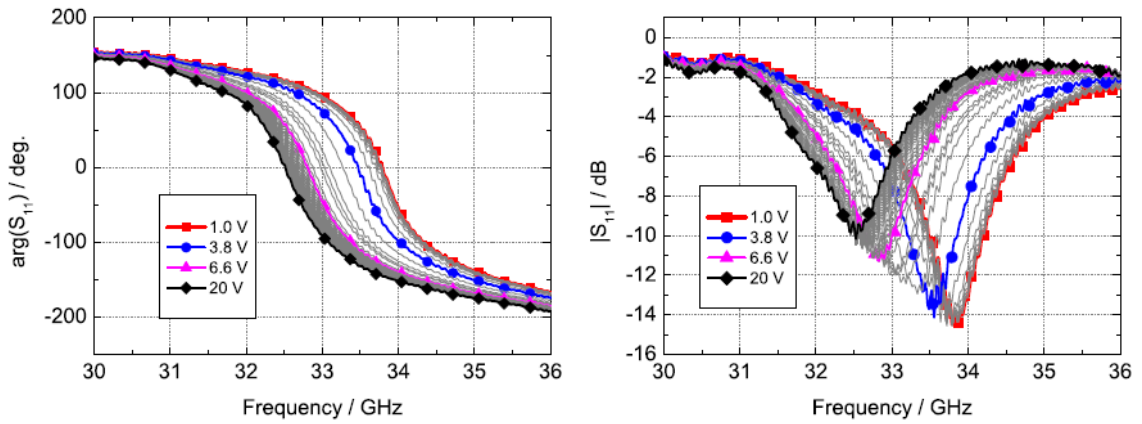


Figure 15 Measured response shift of LC cell under various DC bias voltages [22].

Through this review, a few groups have consistently shown up in the literature and have been identified as sources to follow throughout this effort. The Institute of Microwave Engineering in Darmstadt Germany has published numerous papers on tunable LC RF electronics and is led by Dr. Jakoby. This group demonstrated the first LC reflectarray with the potential for 2D steering, but much is left to do in terms of beam steering. The Institute of Electronics at Queens University Belfast in Ireland has also worked with Jakoby's group and developed some interesting LC components. Kent State

University in Ohio is working with the Materials and Sensors Directorates of AFRL at Wright-Patterson Air Force Base on developing new LC blends specifically tailored for RF applications. Previous efforts utilize commercial LC developed for optical purposes. This research in doping LC materials to enhance RF properties will likely be necessary for handling operational challenges that will pop up during testing.

Modeling has been performed on COMSOL and CST. COMSOL has multi-physics capabilities necessary to capture thermal, DC, and RF interactions. Tutorials are easily found online to assist in model development. However, CST offers quick full wave field computation of elements allowing for quick iterative design work. The following two figures show the magnitude and phase of modeled S11 measurements taken from CST of a circular resonating patch above a ground plane where the spacing dielectric is treated as a bulk sheet of LC with varying dielectric constant and consistent loss tangent of 0.01.

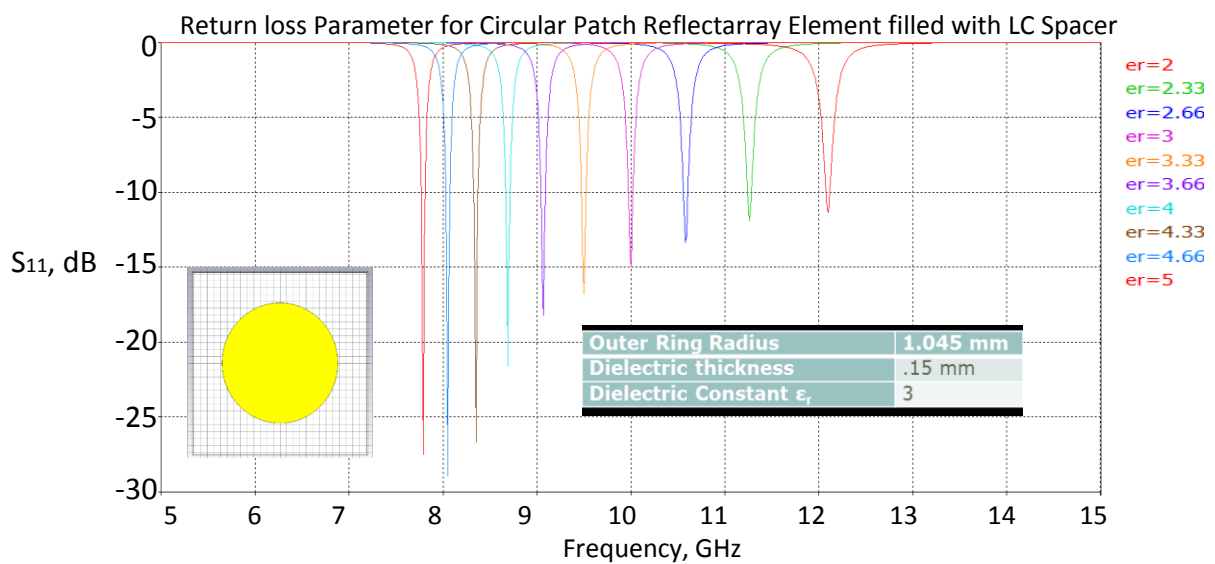


Figure 16 CST Reflection loss plots of circular patch with varying permittivity.

Increasing permittivity of the LC results in greater return loss and less bandwidth. Considering how dielectrics will create a phase delay of an incident EM wave, the increased loss is to be expected. This trend was also shown in modeled results from Figure 14. Typically for a patch element the desired return loss is -10dB meaning that most of the energy is transferred to the patch. However, for a reflectarray, all incident energy is reflected or absorbed meaning any loss is actually waste heat. From a design standpoint it would be prudent to minimize return loss as much as possible or chose configurations where you are transmitting at a frequency that lies as close as possible to the zero line. A narrow band design means less shifting is required to get to either side of the resonance peak. Similarly, the phase can be extracted from modeled results which are essentially derivatives of the magnitude plot. This can be seen in the following figure.

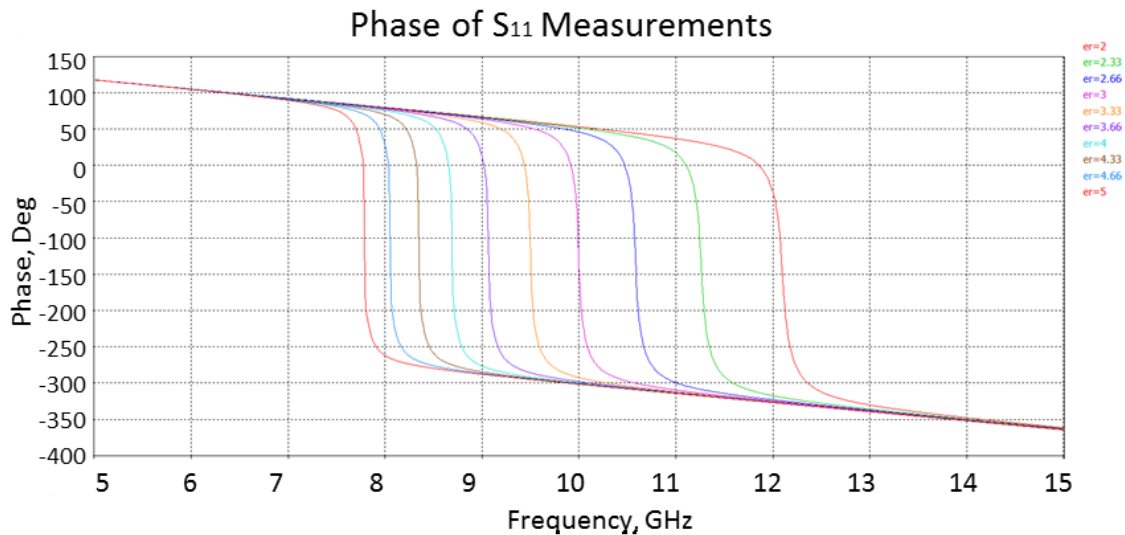


Figure 17 CST phase plots of patch with varying permittivity

For a phase array element, the potential phase difference needs to be at up to 300 degrees to serve as a useful element for wide field of views but for very narrow steering limits <20 degrees, less will work. This is required to achieve beam steering in arrays. It

can be seen how the permittivity controls not only the placement of the curve but also the slope. Having a narrow slope (as seen for the higher permittivity plots) means left LC tunability is needed. For example. If 10GHz was the operational frequency then a permittivity range of 2.6 to 3.3 is needed to cover ~ 350 degrees of phase differential. However, for 8GHz, permittivity values of 4.6 to 5 will suffice to achieve similar shift. One interesting observation from previous researcher results shown in Figure 14 and Figure 15 was that the magnitude of loss would increase with applied DC voltage and that the range would be almost 5 GHz for a 35GHz unit. However, the measured response showed decreased loss as well as a smaller range of shifting. This is suspected in this effort to be a manifestation of the effects of applied surface charges on the reflecting element. Figure 18 shows a COMSOL model of the previously modeled unit cell with no surface charge and with a surface charge present from DC charging. Results show a decrease in the amount of loss that occurs as well as less shifting down in frequency, similar to the trends seen in previous research.

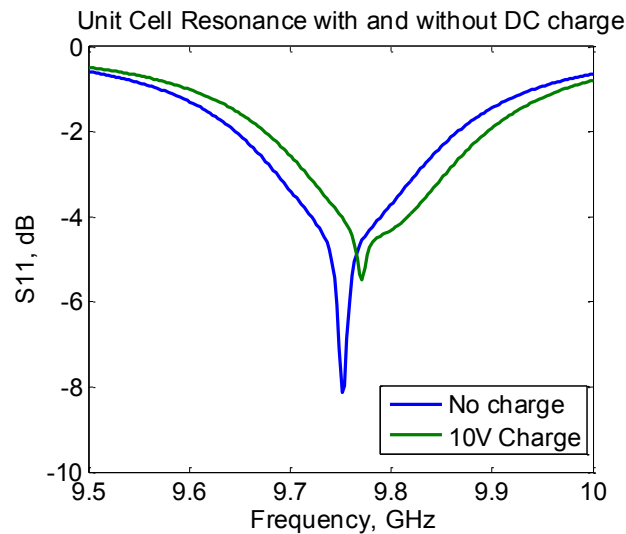


Figure 18 COMSOL plot of unit cell with and without DC bias applied.

Ideally the element's topology would be designed to have a broadband response such that the permittivity change did not diminish reflective power of the cell. With the traditional square and circular patches used in this research a change return loss magnitude will be noted as permittivity is tuned. However optimization of the unit cell is not the focus of this work and is a common research area invested into already for specific missions. The author will instead consider amplitude of reflection energy constant over all tuned regions to simplify the array discussion. Readers can expound on the remaining discussion by evaluating a particular elements amplitude change and incorporating into their own non-uniform amplitude, non-uniform spacing design approach. Once the phase range of a setup is known, the array design can be checked. Assuming the array is fed by a horn antenna, the array must convert the spherical wave it receives into a culminated focused beam in some desired direction or a contoured beam be achieved with a phase-only synthesis method. Other design assumptions from literature [16] include choosing array sizes and f/D ratios (D is array length, f is distance of horn from array) where spacing changes for elements beyond 40 degrees and 50 degrees off normal from the horn, and added efforts be invested into the phase correction of these elements that are much farther from the source than the central elements. The same source sites that coupling may be ignored for elements with greater than $1/4\lambda$, but this will lead to larger grating lobes. A simplified approach to understanding the array layout and controlled phase distribution can be done by considering the following.

To change the 'electrical shape' of a reflected beam (θ_b, φ_b) from a horn incident to a flat plate, the phase at any point, $\varphi(x_i, y_k)$, is expressed by,

$$\varphi(x_i, y_k) = -k_0 \sin \theta_b \cos \varphi_b x_i - k_0 \sin \theta_b \sin \varphi_b y_k \quad 11$$

where k_0 is the propagation constant and (x_i, y_k) represent element locations. However the phase reflected at those locations are also defined by the phase of the array resonating element which will match with the incident beam corresponding to it geometrical based phase delay. This contribution is captured as follows,

$$\varphi(x_i, y_k) = -k_0 d_{i,k} + \varphi_R(x_i, y_k) \quad 12$$

where φ_R is the phase of the element located at some point on the flat plate and d is the distance from the feed phase center to the element. These two equations can be combined to isolate the phase of the element at a given point as,

$$\varphi_R(x_i, y_k) = k_0(d_{i,k} - (\cos\varphi_b x_i + \sin\varphi_b y_k)\sin\theta_b) \quad 13$$

The previous equations have been setup for a more common rectangular array and tested in Matlab. The following 3 figures show the array setup for a 10GHz 30x30 element array with an f/D ratio (ratio of feed phase center height to the reflector diameter) of 0.5 and element spacing of 0.25λ . The code shows the difference between a normal reflected pencil beam and a beam steered off normal by 30 degrees along both phi and theta.

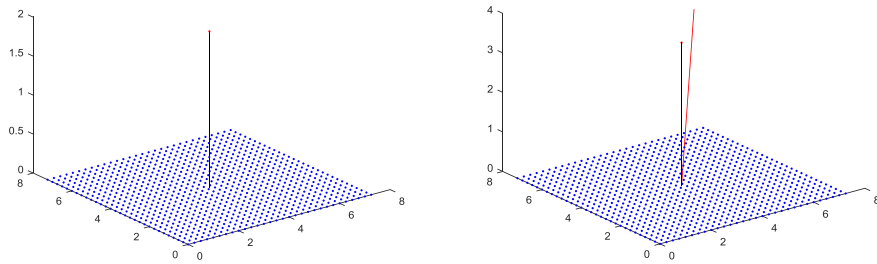


Figure 19 Array setup for a normal (left) and steered (right) configuration where blue dots are elements, black line is path to feed center and red line is reflectarray pointing vector.

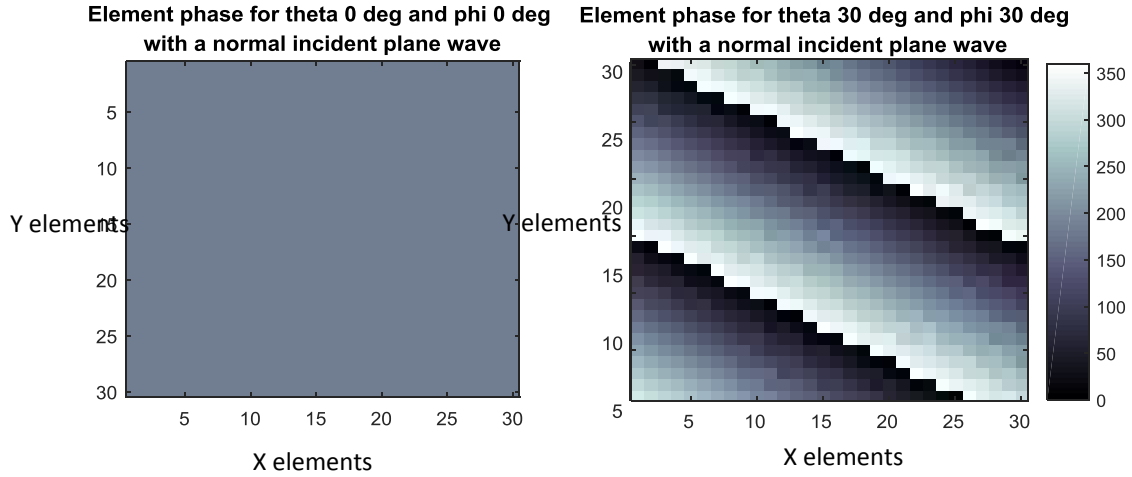


Figure 20 Required plate phase distribution for a culminated beam in the normal (left) and steered (right) configuration.

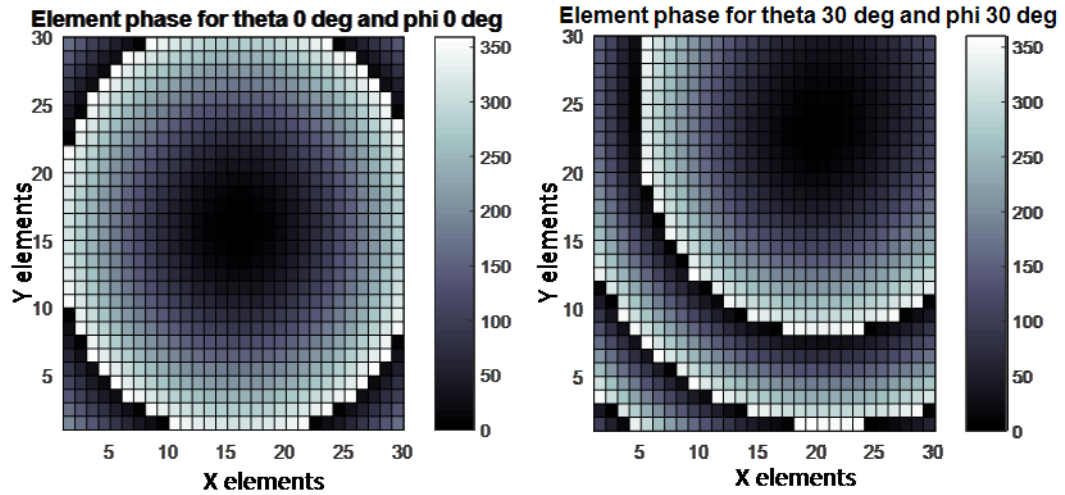


Figure 21 Required element phase distribution for a culminated beam in the normal (left) and steered (right) configuration.

This series of equations allows for a quick way for reflectarray designs to be matched to a possible configuration. The elements are catalogued into their respective phase states and distinguished by their available range and tuning resolution and then

essentially they are matched on the graph shown in Figure 21. However if a particular designed topology only has a tunable range of 200 degrees, then the size of the array, f/D ratio, and steering limits will all be reduced or shifted to meet the elements phase limits. Additionally, the cycling of multiple 360 degree bands can result in echoing noise in the signal. This can be rectified by making elements with larger phase delays that exceed 360 degrees or by bending the flat panel such that it resembles more of a corner reflector. If a flat plate is ultimately desired with 30x30 elements and the reconfigurable element is only capable of 200 degrees of phase shift then the previous distribution for a normal reflected beam significantly increases the feed height from an f/D of 0.5 to 2 and will increase the design requirements for the feed horn to minimize overspill from the beam shape onto the array. This distribution is shown in the following image.

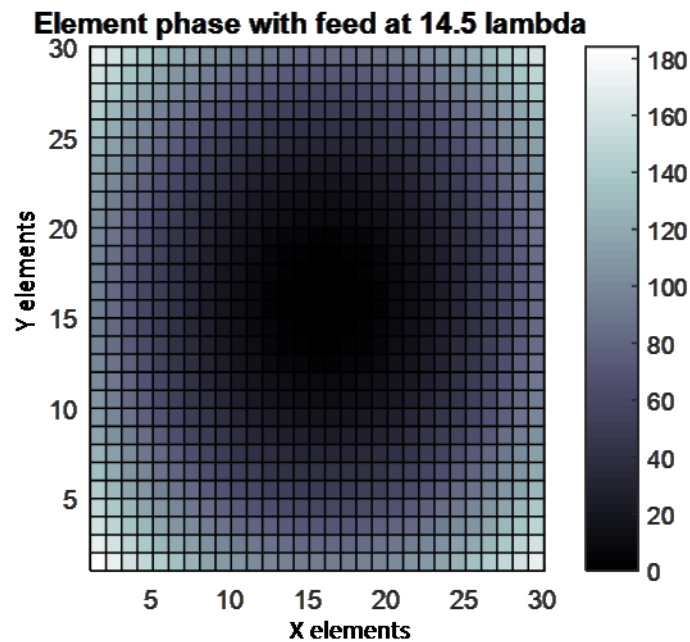


Figure 22 Reflectarray considering element phase control limitations.

While these models work well for known materials in a benign environment, there is much left undiscussed about the modeling and operational impacts to the cells for an as-built system or even as constituent materials once exposed to harsh environments. The following chapters will explore some of those effects and the resulting operational impact that can be expected if the effects are not properly mitigated.

CHAPTER 4: MANUFACTURING CONCERNS FOR RECONFIGURABLE LiCRas

4.1 Introduction:

This chapter will cover fabrication and limits of elements along with surface roughness issues encountered while building a prototype reflectarray. The reflectarray can be considered as a collection of components assembled into one functional package. These components may be designated in varying levels of complexity. For this effort we will consider the dielectric body, the metallic radiators and routing, the liquid crystal, and the control electronics. These 4 items are required to make a functional reconfigurable reflectarray. One of the design interests of this research was to look at more unique manufacturing processes of assembling an array. The traditional approach is to etch the ‘cathode’ and ‘anode’ metallic elements on some dielectric (PCB, rogers, LCP, etc.) with necessary wire routing and vias and then sandwich them together with some thickness controlling dielectric spacer. Another more unique way to approach this problem is to take advantage of the advancements in 3D manufacturing.

The advancement of 3D printing has spawned countless areas of research applications and in materials consisting of both conductive and dielectric properties. Within the field of applied electromagnetics, 3D printing has been used for complex antennas, probes and light weight plated waveguides [56-62]. These new processes along with plating and direct write technologies create a new frontier for antenna approaches to be conceived and executed with increasing precision. Of critical importance is first determining dielectric permittivity and loss tangents for modeling as well as dielectric strength for surviving spacecraft charging and outgassing of the material. Other relevant test include UV exposure, Atomic Oxygen (AO) degradation and energetic particle

exposure simulating space weather radiation (electrons and protons). This chapter will focus on the procedure used to characterize a 3D printed material sample and monitor changes prior and after exposure to various simulated space environments.

4.2 Printed substrates

Of critical importance is first determining dielectric permittivity and loss tangents for modeling as well as dielectric strength for surviving spacecraft charging and outgassing of the material. While it is suspected that the material used here is absolutely not suitable for space, it is expected to provide a useful tool to the reader in understanding the design and test challenges to expect for printing materials that do claim space worthiness. It should also be noted that some materials that are not space practical may be made so through the use of additives. All of the electronic boards we make at AFRL follow Military Specification standards for potting and conformal coating so that the vulnerable components are protected from vacuum by some enclosing medium.

4.2.1 Designing to Account for Manufacturing Errors

AFRL utilizes an iProTM 8000 Stereo-lithography (SLA) printer which can support a variety of solutions. Currently we utilize an Accura 55 solution for models and prints in layers of 2-6 mils depending on part geometry and solution. After parts are printed they are cleared of any truss structures printed to support geometry and cleaned in an alcohol bath for 30 minutes to remove unintended resin still present. Afterwards, parts are UV cured to solidify the structure to final specifications for an additional 30 minutes. In this time the printed specimen can warp or constrict as the material becomes denser. For RF applications, this can be a significant source of error, [59] requiring a verification procedure to quantify the amount of constriction and even surface roughness occurring

and if it is linear or nonlinear. Two parts were prepared with stepped thickness common of other RF dielectrics (like Rogers RT/Duroid high frequency laminates [58]) with incremental thicknesses of 0.01, 0.025, .0500, 0.075, and 0.100 inches. Samples were made to be printed flat and vertically, as seen in Figure 23.

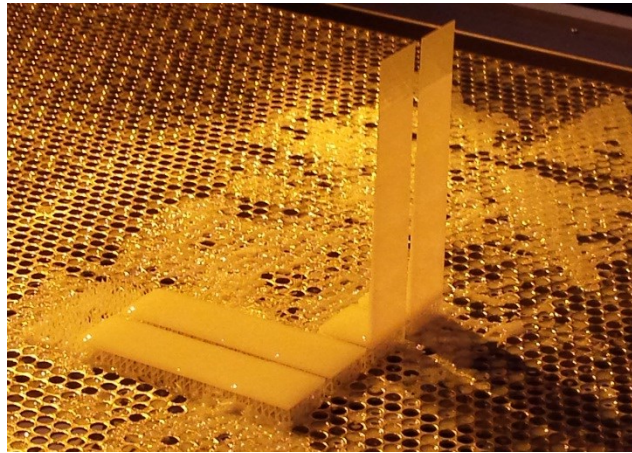


Figure 23 3D samples printed for thickness verification procedures and for various build orientations in 3D printer: horizontal (left) and vertical (right).

It can be seen that a truss is printed with this SLA machine that must be removed. The very act of removing the truss structure introduces damage to the surface and creates a guaranteed surface error on the printing initiation face. The other anomaly noticed was that the software/hardware failed to print the thinnest 0.001 inch section for the horizontal standard. A mechanical caliper set was used prior to and after curing on the samples to verify dimensions to the nearest 0.001 inch. Thickness measurements were taken at all corners for each sample segment and at the center. The results are tabulated below in the next two tables. Measurements show that the act of curing caused the thickness of all samples to decrease 1-2 mils. It was also found that while flat printed samples were more likely to be closer to the modeled thickness, it had a greater standard deviation across the

surface measurements meaning that the printing and removal of the truss has a significant impact on surface finish which would correlate to an increased surface Root Mean Square (RMS) error. The standard deviation for all measurements of the horizontally printed specimen reached up to 4 mils. Contrarily, it was realized that the vertical standing orientation yielded a nearly flawless surface with standard deviations less than 1 mil. However it was also found that thickness were 4-5 mils thicker than modelled resulting in a manufacturing thickness error of up to 24%. This was seen for all segments except the 0.01” thick segment. It is speculated that the printer software rounds layers (performed in 3 mil increment) for parts to a common interval and factors in UV curing related shrinkage.

Table 2 Printing Thicknesses Of Varying Oriented Samples Pre-Cure

<div> <div>1 3</div> <div>5</div> <div>2 4</div> <div>decreasing size →</div> </div>		Prior to UV Cure					
		Flat (in)		Standing (in)			
		A	B	A	B		
0.1" segment						Flat Average	Flat Std Dev
1		0.110	0.110	0.107	0.106	0.106	0.004
2		0.111	0.110	0.105	0.106	Standing Average	Standing Std Dev
3		0.105	0.105	0.106	0.106	0.106	0.001
4		0.105	0.104	0.107	0.106	Flat Error	Standing Error
5		0.101	0.101	0.106	0.106	6.20%	6.10%
0.075" segment						Flat Average	Flat Std Dev
1		0.076	0.076	0.081	0.081	0.075	0.002
2		0.076	0.076	0.082	0.082	Standing Average	Standing Std Dev
3		0.072	0.075	0.081	0.081	0.081	0.000
4		0.075	0.075	0.081	0.081	Flat Error	Standing Error
5		0.072	0.072	0.081	0.081	0.67%	8.19%
0.05" segment						Flat Average	Flat Std Dev
1		0.052	0.051	0.056	0.056	0.051	0.002
2		0.054	0.051	0.056	0.056	Standing Average	Standing Std Dev
3		0.050	0.051	0.056	0.056	0.056	0.000
4		0.052	0.050	0.056	0.056	Flat Error	Standing Error
5		0.048	0.048	0.056	0.056	1.40%	12.00%
0.025" segment						Flat Average	Flat Std Dev
1		0.028	0.027	0.032	0.032	0.028	0.002
2		0.026	0.027	0.032	0.032	Standing Average	Standing Std Dev
3		0.030	0.031	0.032	0.032	0.032	0.000
4		0.032	0.031	0.032	0.032	Flat Error	Standing Error
5		0.025	0.025	0.032	0.032	12.80%	28.00%
0.01" segment						Flat Average	Flat Std Dev
1		NA	NA	0.010	0.011	NA	NA
2		NA	NA	0.011	0.011	Standing Average	Standing Std Dev
3		NA	NA	0.010	0.010	0.010	0.000
4		NA	NA	0.010	0.010	Flat Error	Standing

						Error
5	NA	NA	0.010	0.010	NA	1.50%

Table 3 Printing Thicknesses Of Varying Oriented Samples Post-Cure

	Post UV Cure for 30 minutes					
0.1" segment					Flat Average	Flat Std Dev
1	0.109	0.109	0.104	0.104	0.105	0.003
2	0.109	0.107	0.104	0.104	Standing Average	Standing Std Dev
3	0.104	0.103	0.105	0.104	0.104	0.000
4	0.103	0.103	0.105	0.105	Flat Error	Standing Error
5	0.100	0.100	0.105	0.104	4.70%	4.40%
0.075" segment					Flat Average	Flat Std Dev
1	0.074	0.074	0.080	0.079	0.073	0.002
2	0.075	0.074	0.080	0.079	Standing Average	Standing Std Dev
3	0.070	0.074	0.079	0.079	0.079	0.000
4	0.074	0.075	0.079	0.079	Flat Error	Standing Error
5	0.071	0.070	0.079	0.079	2.53%	5.60%
0.05" segment					Flat Average	Flat Std Dev
1	0.046	0.050	0.055	0.055	0.050	0.002
2	0.050	0.051	0.055	0.055	Standing Average	Standing Std Dev
3	0.051	0.050	0.055	0.055	0.055	0.000
4	0.053	0.052	0.055	0.055	Flat Error	Standing Error
5	0.047	0.047	0.055	0.055	0.60%	10.00%
0.025" segment					Flat Average	Flat Std Dev
1	0.026	0.025	0.031	0.031	0.027	0.002
2	0.025	0.026	0.031	0.031	Standing Average	Standing Std Dev
3	0.029	0.030	0.031	0.031	0.031	0.000
4	0.030	0.030	0.031	0.031	Flat Error	Standing Error
5	0.025	0.025	0.031	0.031	8.40%	24.00%
0.01" segment					Flat Average	Flat Std Dev
1	NA	NA	0.010	0.010	NA	NA
2	NA	NA	0.011	0.010	Standing Average	Standing Std Dev

3	NA	NA	0.010	0.010	0.010	0.000
4	NA	NA	0.010	0.010	Flat Error	Standing Error
5	NA	NA	0.010	0.010	NA	1.00%

Models were updated to account for the non-linear effects and reprinted to verify correct thicknesses. Three 12”x 6” sheets were printed to be tested for dielectric property characterization of each relevant size that the printer could handle and corresponding to traditional commercial product thicknesses (0.1, 0.076, 0.049 and 0.030 inches).

4.2.2 Dielectric Characterization of Printed Dielectrics

The confocal Fabre-Perot resonator has been developed and described in the literature for obtaining dielectric properties of sheet materials [60]. It consists of two spherical antennas, shown below, with radius of curvature R separated by distance R , while semi-confocal resonator consists of one spherical antenna and a flat plane separated by $R/2$ distance. At a distance of $R/2$ from the spherical mirror the electromagnetic radiation inside the resonator focuses to a Gaussian spot, the radial diameter of which is proportional to the radiation wavelength and the mirror’s radius of curvature. While multiple modes are present in the resonator, the fundamental TEM₀₀ modes which have the smallest radial diameter are typically used.

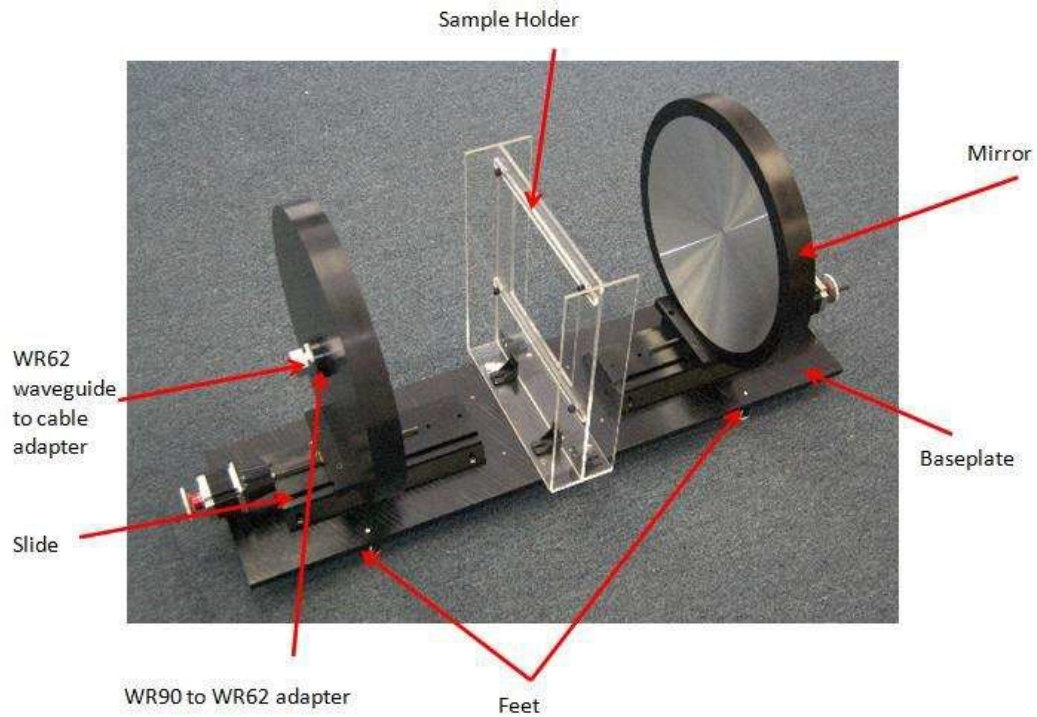


Figure 24 Confocal Fabre-Perot Resonator

The radiation is coupled through a small hole in the center of the (each) spherical mirror. Present confocal resonator is used for transmission and reflection measurements, while the semi-confocal resonator is set up for reflection measurements. The confocal resonator has twice the volume of a semi-confocal resonator, and correspondingly twice the Q value. The resulting focused Gaussian beam provides a profile as seen below.

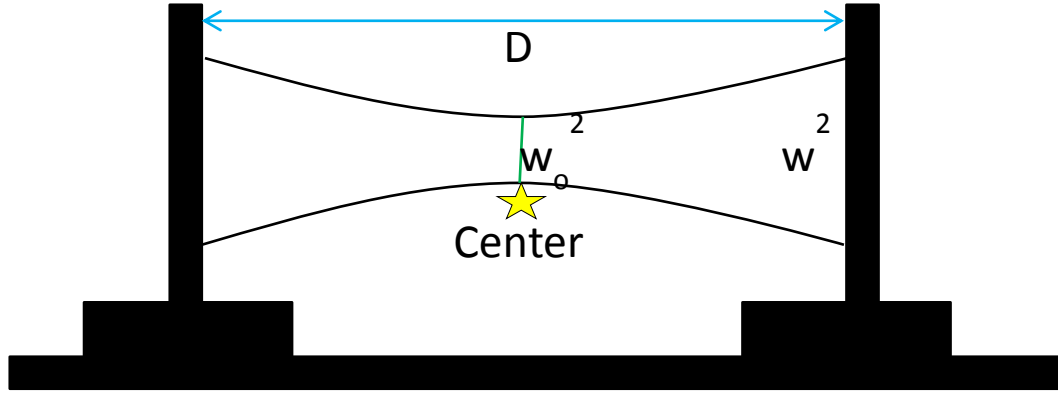


Figure 25 Profile of Fabre Perot Resonator showing focused Gaussian beam

Measurement frequency is controlled by the distance between the plates, D , such that a resonating standing wave node or antinode should be present at the center. Additionally, the spot beam diameter, w_o^2 , will change with the distance and size of the mirrors with radius of curvature, R_o , as indicated in by the following equations.

$$w^2 = \frac{\lambda R}{\pi} \sqrt{\frac{D}{(2R_o - D)}} \quad 14$$

$$w_o^2 = \frac{\lambda}{2\pi} \sqrt{D(2R_o - D)} \quad 15$$

Given the fixed size of the mirrors, the above equations can be used to determine the inspection size of a given material for the operational frequency range of the attached waveguide and the available spacing possible in the setup as follows.

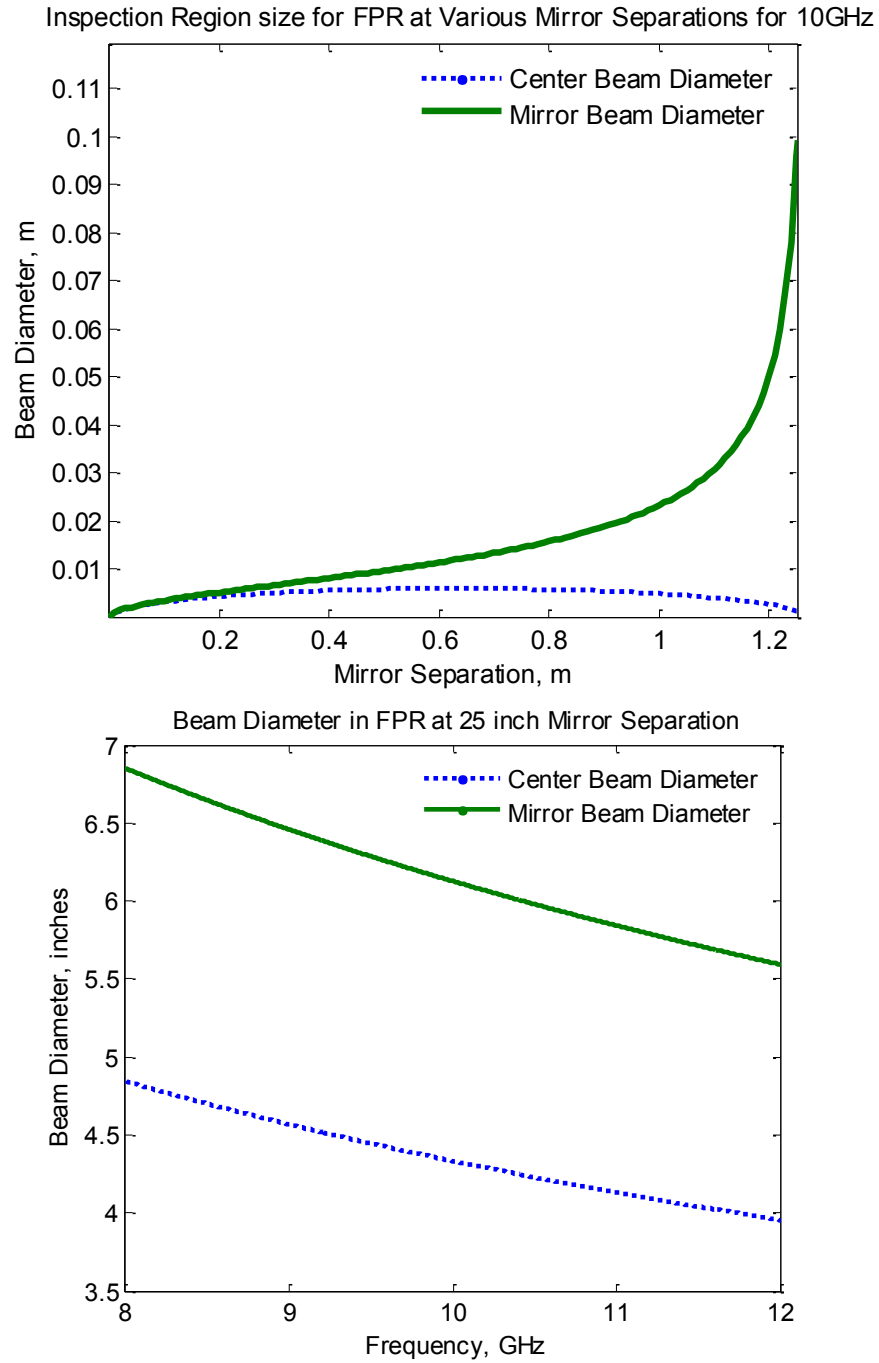


Figure 26 Inspection Beam Size given mirror spacing (top) and frequency (bottom)

When the FPR chamber is empty, a measurement can be taken to see the effects various electromagnetic modes. To determine a particular TEM_{qpl} mode, the following

equation is used, where Fc_q is peak position, $q/p/l$ are mode numbers for transverse EM waves, D is plate separation, c is speed of light.

$$Fc_q = \frac{c}{D} (q + 1 + (2p + l + 1) * \frac{\arccos(1 - \frac{D}{Ro})}{\pi}) \quad 16$$

Additionally, the peaks will correspond to a symmetric or antisymmetric mode as shown below where wave number, k , refractive index, n , and phase shift from the focused wave in the material are indicated by ϕ_t and ϕ_d , and become factors.

$$\frac{1}{n} \cot(nkt - \phi_t) = \tan(kd - \phi_d) \quad 17$$

$$\frac{1}{n} \tan(nkt - \phi_t) = -\tan(kd - \phi_d) \quad 18$$

These equations require slightly higher level iterative analysis to converge on the correct value. The resulting resonating cavity for our chamber is shown below along with bandwidth measurements used to define the quality factor of the peaks. To isolate the TE/ M_{00} mode a piece of paper with a circle cut out the size of the beam spot size is placed in the center to disrupt the fundamental mode. This process is seen in the following figure.

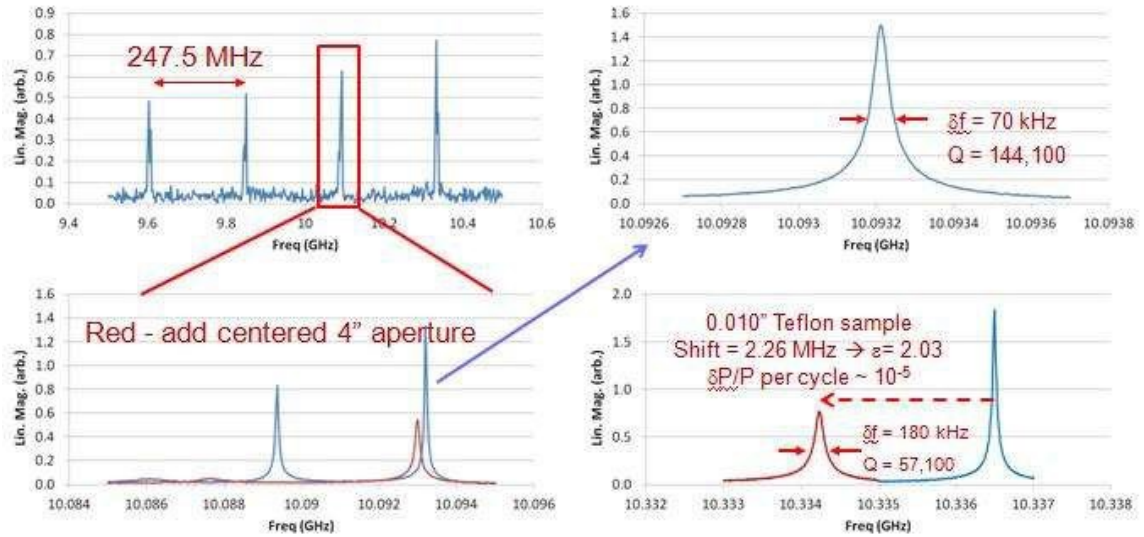


Figure 27 Mode observation and isolation in open air FPR and with the addition of Teflon (lower right)

To calibrate the setup, one would typically use a substrate with known properties, such as Teflon. Placing this sheet in the mirror will result in a shift of resonant modes that would be present with just atmosphere in between. This effect is shown below isolating the addition of Teflon seen above to its own frame.

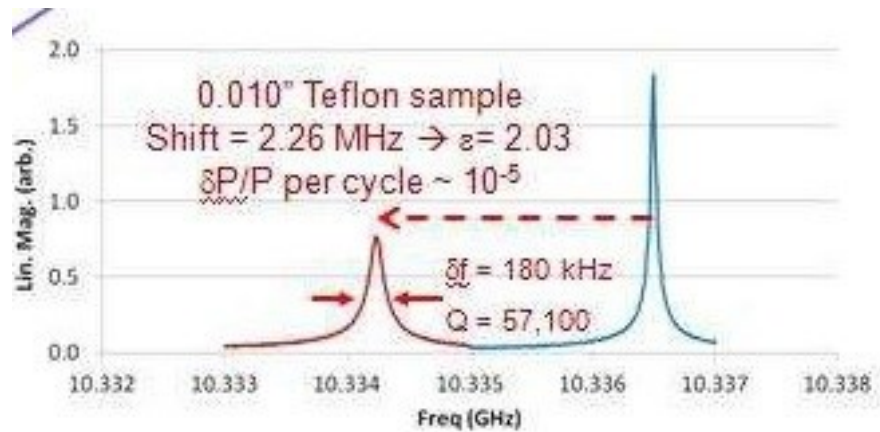


Figure 28 Open chamber (blue) and Teflon sheet (red) measurement in FPR setup.

To perform a sample measurement, the resonant frequency and Q factor are measured for both the empty resonator and for the resonator loaded with sample. For dielectric samples the change in resonant frequency is mostly due to the real part of the dielectric constant and the thickness of material under test, while the change in Q is due to dielectric losses. The analytical equations described in [61, 62] are used to derive dielectric properties of flat samples measured in confocal and semi-confocal Fabre-Perot resonators. The necessary equations are provided as follows where t is half-thickness, Q_o is the lossless Q (no sample present), Q_l is for the “lossy” Q (sample present) and Q_e is the final Q factor.

$$\tan\delta = \frac{1}{Q_e} \frac{t\Delta + d}{t\Delta + \frac{1}{2k}(\sin 2(kd - \phi_d))} \quad 19$$

$$\Delta = \frac{n^2}{n^2 \cos^2(nkt - \phi_t) + \sin^2(nkt - \phi_t)} \quad 20$$

$$\frac{1}{Q_e} = \frac{1}{Q_o} - \frac{1}{Q_l} \quad 21$$

One of the primary issues with this measurement is the need for a very stable environment. Measurements required a canister placed around the chamber to block air currents from the air conditioner. The effects of failing to do so are seen below and are the direct result of thermal expansion in the aluminum FPR.

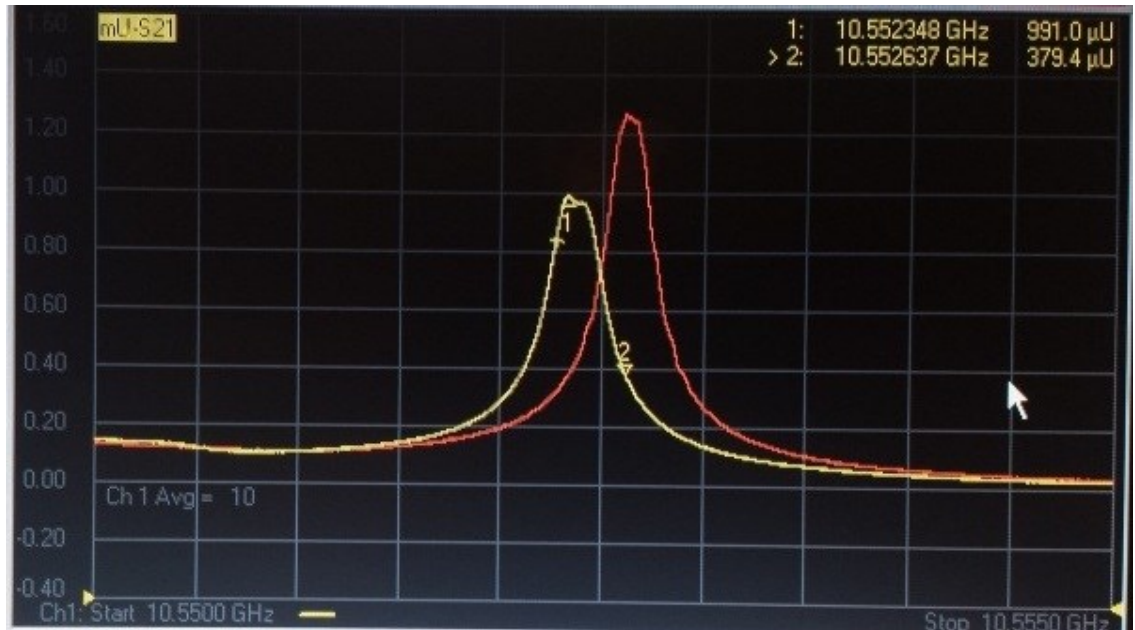


Figure 29 Open Chamber measurement with thermal extremes from air conditioned room (72F-75F)

Table 4 Dielectric Measurements of iPro 8000 printed ABS

Sample thickness	Average ϵ_r	Standard Deviation	Average loss tangent ($\tan \delta$)
.100	1.935	.065	0.02
.076	1.943	0.179.	0.03
.049	1.586	0.132	0.02
.030	1.426	0.117	0.01

The measurements made with the printed substrates is summarized in the above table. Another limitation was realized with this approach upon completion of measurements. The accuracy is reduced with reduced sample thickness as it occupies less of the measured volume in the FPR ($\ll 1\%$) however, if the sample is very lossy ($>.01$) then the peaks obtained drop below the VNA noise floor making it impossible to get a

good measurement. While the printing error between sheets can lead to substantial deviations in permittivity for thicknesses near the printer limits or not an interval of the mechanical layer spacing, the permittivity was slightly more consistent.

4.2.3 Space Weather Effects on 3D Printed Dielectric

While a future chapter will discuss space weather effects on various LiCRAS components, a brief section was seen as useful to discuss how the radiation of space compiles on the mechanical/geometric uncertainties discussed in this chapter already. The samples previously tested were exposed to a simulated rapid space aging exposure where Strontium 90 (Sr-90) is used to expose materials to large doses of high energy electrons as the sample radiates. Depending on the proximity of the sample to the source, the material may experience levels less than, equal to, or greater than GEO radiation levels. Unfortunately, no source exists that can properly replicate the complex environmental spectrum created by our sun/magnetosphere/galactic rays/etc. But we can isolate certain spectrums to capture the basic effects. In the case of the printed ABS, we simulated a 3, 5, and 7 day GEO high energy electron environment. The intent was to re-measure the permittivity and loss tangent values of the ABS plastic. Unfortunately, only the thinnest sample retained enough of its shape to be measured. The bond breaking and dislocation that must have occurred in the thicker samples was so great that the sheets bowed out facing the source as the closest layer expanded due to the greatest incident flux on that face. As a result, none of them can be re-characterized in the FPR as the center is not constant. The one sample that did seem to survive relatively undamaged likely due to the lack of material present to create the deformation force required to bow the sample had improved properties. The permittivity dropped from 1.426 to 1.29 but

with a standard deviation of .079 between measurement samples as opposed to the prior 0.117. Additionally, the loss tangent dropped from 0.01 to 0.007. When plastics breakdown, they can outgas their broken bond constituents which may be responsible for the reduction of lossy materials in the way of the FPR after aging. More discussion and testing will be provided later, but at this point it is important to note that geometrical consistency of printed material prior to curing, post cure, post space exposure can have a significant amount of variability and in the case of ABS exceeded our ability to track it making it a non-starter for consideration. Appropriate candidate printed substrates must be able to withstand radiation and manufacturing processes without deviating from the initial modeled specimen.

CHAPTER 5: THERMAL/VACUUM CONCERNS FOR RECONFIGURABLE LiCRas

5.1 Introduction:

What isn't properly captured in the reflectarray equations discussed in Chapter 3 is the impact temperature has on the array, LC transition voltage, LC tunable range, or LC transition times. For example, if we consider a generic LC from previous studies [46] the various phases can be monitored based on pressure and temperature with noting that there is not a vapor transition of the fluid within the expected operational limit of 0°C-100°C.

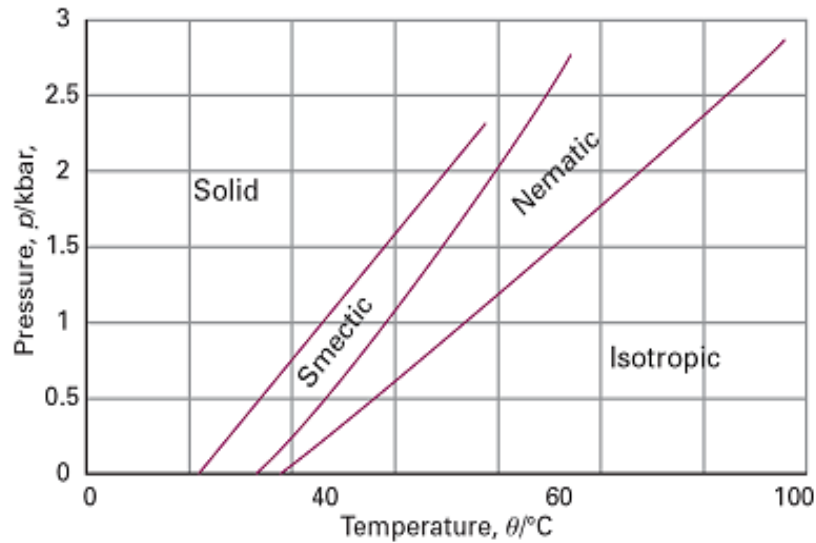


Figure 30 Phases of LC under pressure and temperature [46]

As the LC occupies different regions of the previous graph, the viscosity of the fluid changes. These trends are anecdotal and change for every molecular blend. These trends are not typically studied for a particular blend and rather an assumption is made for thermal stability. However, separate studies have been found to illustrate this point. First, as temperature rises, LCs become increasingly less ordered until they lose their anisotropy altogether. This implies a reduction in fluid viscosity, which in turn means reduced stresses needed to disorder rods. From

Hooke's law we know that material elastic properties are directly proportional the force required to displace the 'spring' load of the crystalline structure under a shear or tensile load ($F=kx$). Therefore, we would fundamentally expect that as an LC is heated becoming more 'fluid', less ordered and more isotropic, that the force required to displace orienteers also goes down trending towards zero indicating no orientation displacement and also reduced elastic moduli. The below figure validates this conceptualization showing LC elastic degradation with increased temperature.

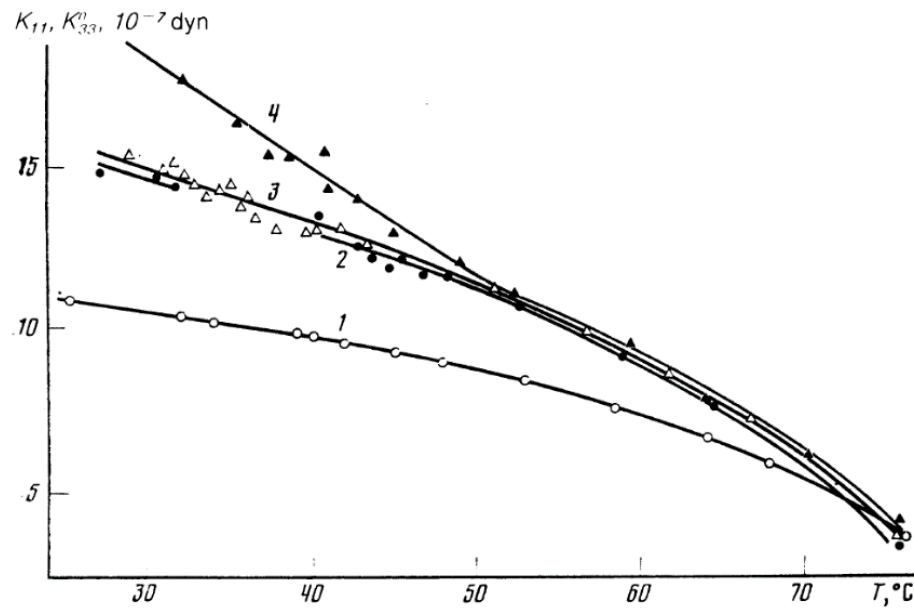


Figure 31 Nematic LC elastic properties with increased temperature [63]

Considering equations 8-10, one might expect LC applications to be considered at higher temperatures in order to reduce the required operational voltages. However there are consequences to the material as a result to these reduced elastic moduli. For one, it is expected that a reduction of the elastic moduli of a material makes it more susceptible to shear loading or less viscous. Looking at Eq. 10. It can be seen that reduced viscosity will make an LC switch faster. This seems logical as an LC that is made too cold will solidify and be unable to shift from a reasonable applied electric field. This trend is

illustrated below where the viscosity of a particular LC is tracked according to the applied temperature, T , relative to its nematic thermal limits, T_N and T_{NA} .

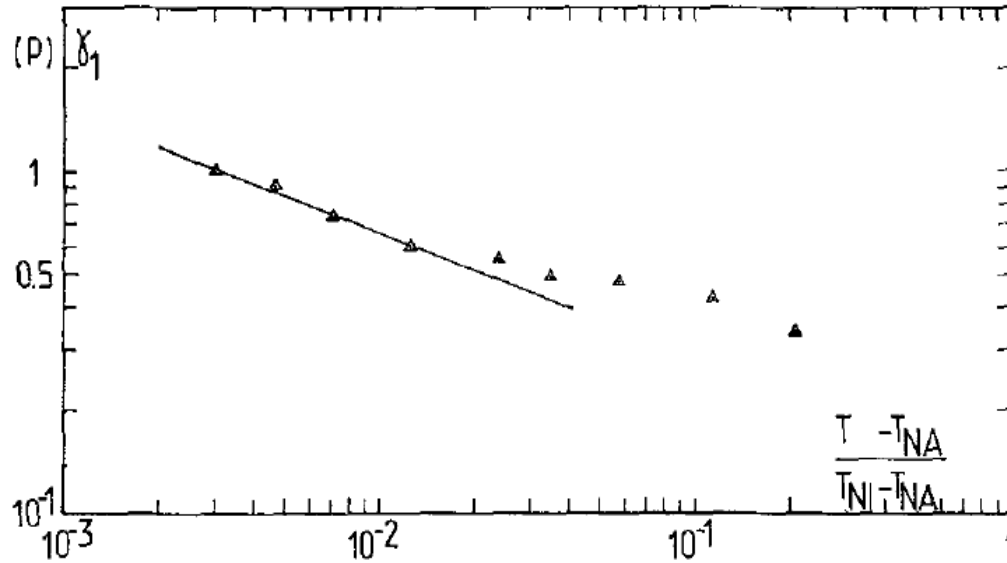


Figure 32 Nematic LC viscosity properties with increased temperature [64]

The negative impact of increased temperature comes from the realization that the hotter an LC become, the closer it approaches an isotropic state. This means the mixture becomes less ordered and once the fluid breaches that transition temperature, the dielectric anisotropy, or δ , is reduced to zero. The following figure demonstrates this phenomenon and indicates the gradual degradation as the temperature limit is reached. This reduction of δ permittivity means that a less dynamic range can be achieved from a cell and less phase delay overall achieved at higher operating temperatures.

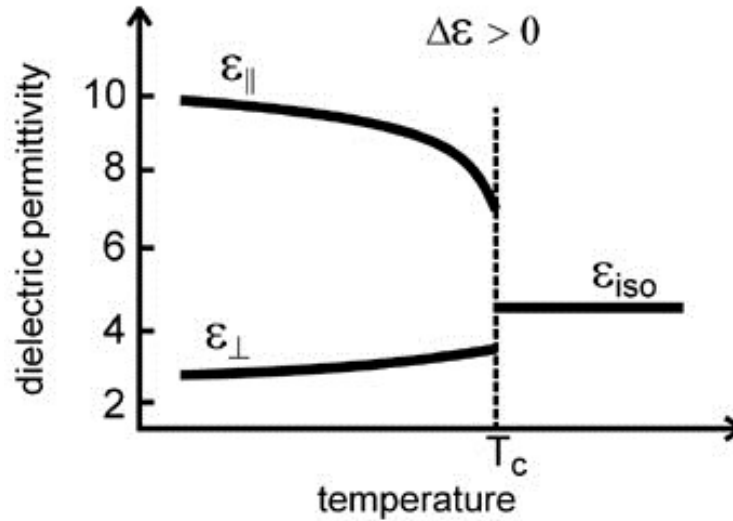


Figure 33 Nematic LC dielectric anisotropy trend with increased temperature [65]

The important observation to make from this attribute of LCs is that it aligns with the Maier-Saupe theory that defines molecular order trending from ‘1’ for a solid LC to ‘0’ for an isotropic LC where the order parameter defines a ratio proportional to the maximum anisotropy for an LC blend and that a larger delta requires a lower transition voltage [66]. From these separate measurements we can create a trade-space table to consider when defining system requirements. Based on the level of thermal management, beam steering, terminal type, different LCs may be chosen.

As Temp rises	Performance
Elastic constant decrease	Smaller activation, slower switching
Reduced Anisotropy	Larger activation, slower switching
Reduced viscosity	Slower switching

5.2 Heat source

Link budgets are briefly discussed in Chapter 1 with highly reliable links containing upwards of 300dB of loss. This is why high power transmitters are required for space communications. The following figure shows a Frequency Selective Surface (FSS) element exposed to a nearly continuous 1W wave in a X-band waveguide (22mm x 10mm) resulting in a power flux density, PFD, of $\sim 4.5\text{kW/m}^2$ or $\sim 0.45\text{W/cm}^2$.



Figure 34 Split ring resonator on Kapton layer exposed to 15 sec 1W pulse in a X-band waveguide [69]. The incident E-field, E , can be assumed from the below equation as $\sim 1302\text{ V/m}$.

$$PFD = \frac{E^2}{377} \quad 22$$

This damage is certainly to be considered catastrophic and uses traditional Kapton and copper etched substrates. This can be mitigated by using more robust substrates (ceramic based) and thicker layers of copper. For now we will assign 0.5W/cm^2 as the red flag for our examples. To help understand just how large this is, the sun provides about 0.137W/cm^2 . Depending on the configuration and exposure to sun light, use of thermal white paints or radomes, it is likely that the transmitter will be the dominating contributor of heat to the system.

Modeling was done on COMSOL of another type of resonating structure meant to perform as an RF absorber in a separate effort to capture high power microwaves in previous in-house research by the author. It was shown in the model how quickly an EM pulse can build up heat in a resonant RF element by resonating at a particular frequency matching the incident wave. This result is shown in Figure 35 where temperatures of the material can exceed 500K in a very short time from very high energy EM pulse. It should be noted that the incident field for the figure below was almost four orders of magnitude greater and is not typical of communication transponder magnitudes.

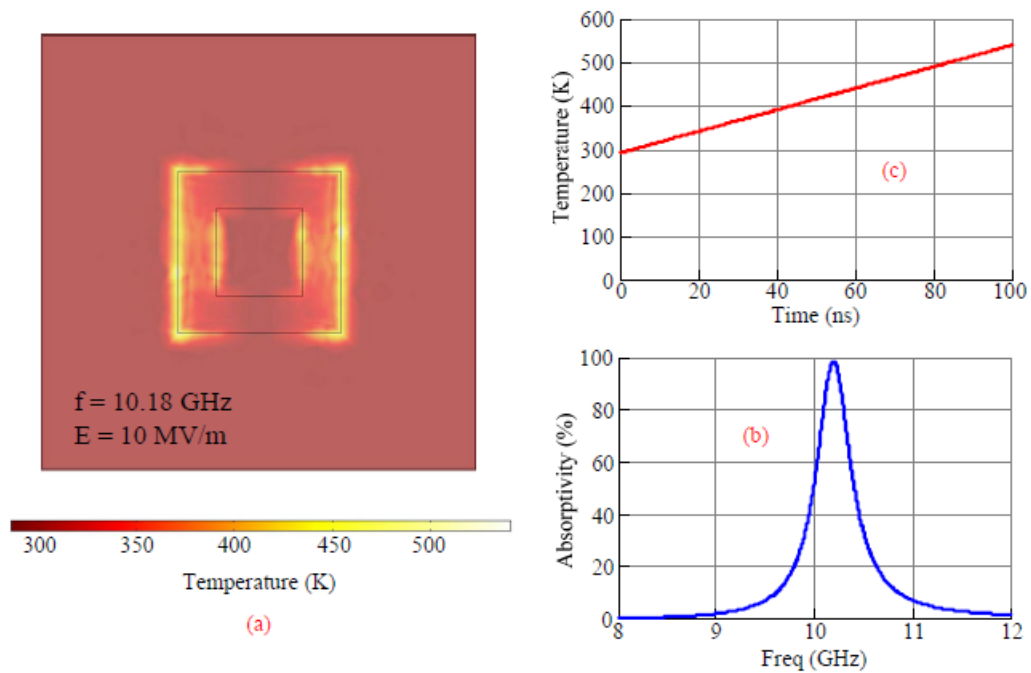


Figure 35 (a) temperature profile of square ring resonator under incident RF pulse, (b) absorption curve showing maximum absorptivity at unit cell resonance, and (c) temperature plot with time of RF exposure.

5.3 Applied Thermal Considerations:

Satellite transponders may not be outputting such high powers as shown in Figure 35, but they are not trivial. While a radar setup may use pulses, communication setups require continuous carrier frequencies modulated at a lower frequency to deliver continuous data. For most satellites, Traveling Wave Tube Amplifiers (TWTAs) are still standard as seen in the case study results shown in Figure 36. The bottom graph shows that TWTAs can range from 50W-1kW for a satellite system. When fed to a 20dB horn for a parabolic reflector setup this can further magnify the transmitting power, P_T . The resulting incident field strength is then found using Equation 23 below,

$$E = \frac{1}{R} \sqrt{\frac{\eta P_T}{2\pi}} \quad 23$$

where R is the distance from the horn to the reflector and η is free space impedance. If the reflector is placed 0.5m away from the horn, the range of incident fields is then assumed to be between 775V/m and 3.6kV/m. The average power flux density can then be estimated as 1.5kW/m² and 34kW/m².

GEO SATELLITE TYPES 1992-2007

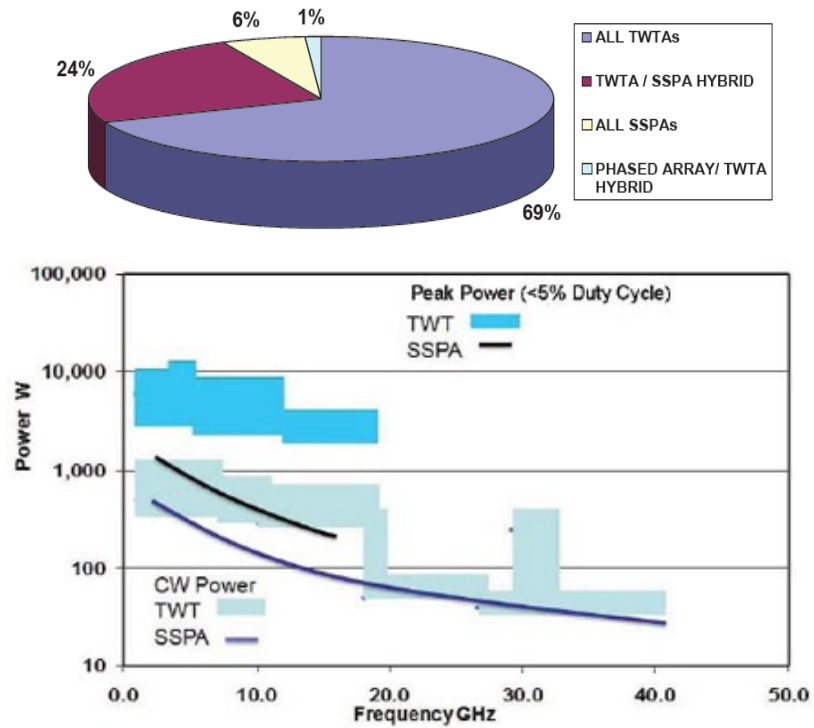


Figure 36 (top) Survey of amplifiers commonly used for GEO satellites[71] and (bottom) common power output of communication amplifiers [72].

This heat is then transferred from the resonating material to the dielectric body. This heat must be removed from body to prevent several issues from risking the functionality of the design. First are the differing thermal expansions on the design. Consider the below table. Material selection is typically done such that all materials in the assembly have approximately the same coefficient of thermal expansion (CTE). Failure to do so will cause fatigue at the interfaces as the assembly under goes thermal cycling. Eventually cracking will occur and the pressure differential between space and the cavity of the LC will cause it to flow out and stop functioning. Consider a 1kW

transmitter feeding a 20dB horn for the earlier described setup shown in Figure 22. Using the discussed thermal issues, the thermal distribution of the source can now be considered. The resulting plot shows the power flux density for the earlier setup.

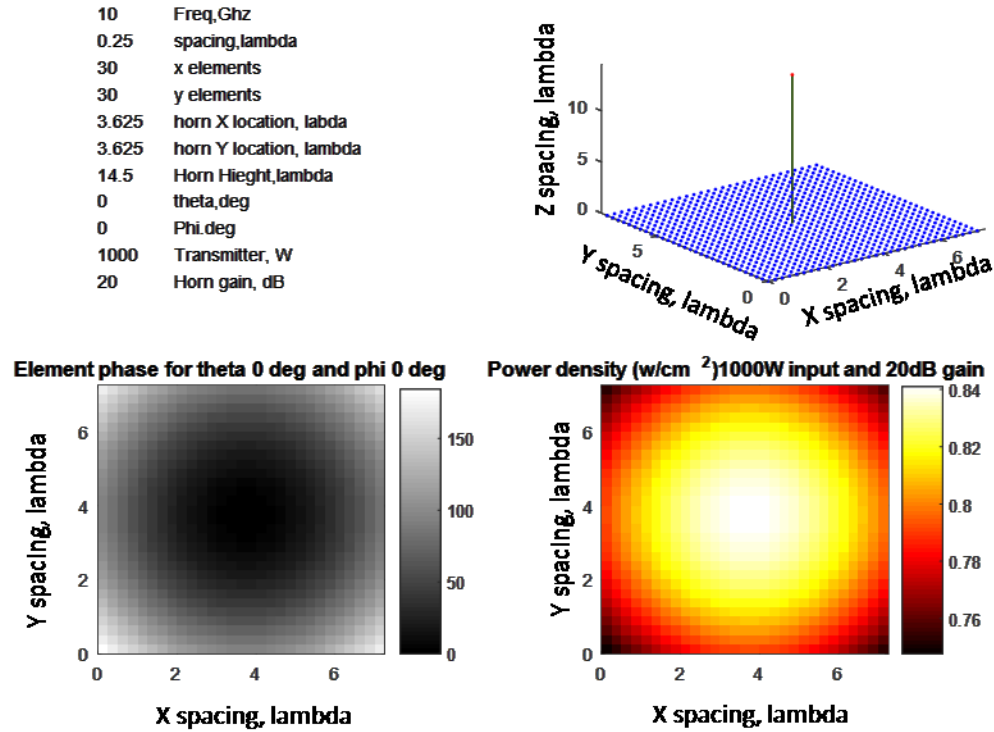


Figure 37 Reflectarray with horn fed by high power transmitter resulting in excessive thermal loading $>0.5\text{W}/\text{cm}^2$

Table 5 Coefficient of Thermal Expansion for primary reflectarray parts (ppm/ $^{\circ}\text{C}$)

Dielectric	Conductive element	Liquid Crystal [73]
Silicon, 3	Aluminum, 23	Adjusted by formula
Glass, 4	Copper, 16.5	Between 3 and 30
FR4, 18	Silver, 19.6	But typically to 17

Given the relative close proximity of traditional RF/LC candidate materials, it is unlikely that mechanical strain and deformation will be the root cause of failure for a candidate LC RF element. It is more likely that the thermal design will be driven by the need to maintain a 0C-60C (at the most) thermal operational range to prevent the LC from solidifying or becoming isotropic. However design will have to consider different approaches for removing heat from a reflectarray to prevent thermal buildup and damage. In the previous figure we see how one configuration may add up to 0.8W/cm², but deep space radiation, integrated oscillating heat pipes, and thermal straps can be used to move that heat away. Each potential design must recognize the amount of heat it can remove to a radiator source. If that delta is too large than additional elements can be added to the array to maintain a desired f/D ratio or, the f/D ratio can be increased. Increasing the ratio will reduce overall all gain due to increased spill over while increased elements adds cost, size and complexity to a design.

Along with changing temperatures come changing properties. While dielectric and conductive properties change for traditional RF material, these are trivial when compared with the effects of temperature on Liquid Crystals. If the LC gets too cold, it freezes and requires more biasing voltage to tune and greater transition times as it transitions into a smectic arrangement. As it heats up the pressure in the cavity may have some reorientation effects as well due to thermal expansion of the orientating ‘rods’ resulting in an imposed torque on the rods[74]. If it gets too hot, it loses its anisotropy and stops functioning as a reconfigurable element. Blending LCs can help increase the thermal range of the molecule by adding dissimilar arrangements of the ‘rods’ making it more difficult for the individual components to react as a bulk material.

A test setup was done to raise a candidate LC cell to a range of equilibrium temperatures. While a particular design can be engineered to accommodate a desired thermal balance, it is of interest to observe the possible steady state thermal limitation on an operational LC. The following summary describes the investigation into the temperature dependence of liquid crystal phase shifters (devices). Several phase shifters were tested at temperatures ranging from -25 °C to 75 °C on a cold plate (which provide both heating and cooling using a circulated fluid bath) to assess the affect temperature has on the total phase shift ($\Delta\phi$) of the device. It has been shown in numerous publications that liquid crystal operation has a dependence on temperature and this temperature dependence varies between the liquid crystal blend employed as discussed previously. Insulating was a challenge for the setup and nitrogen gas chamber was required at lower temperatures to prevent water damage to the setup.

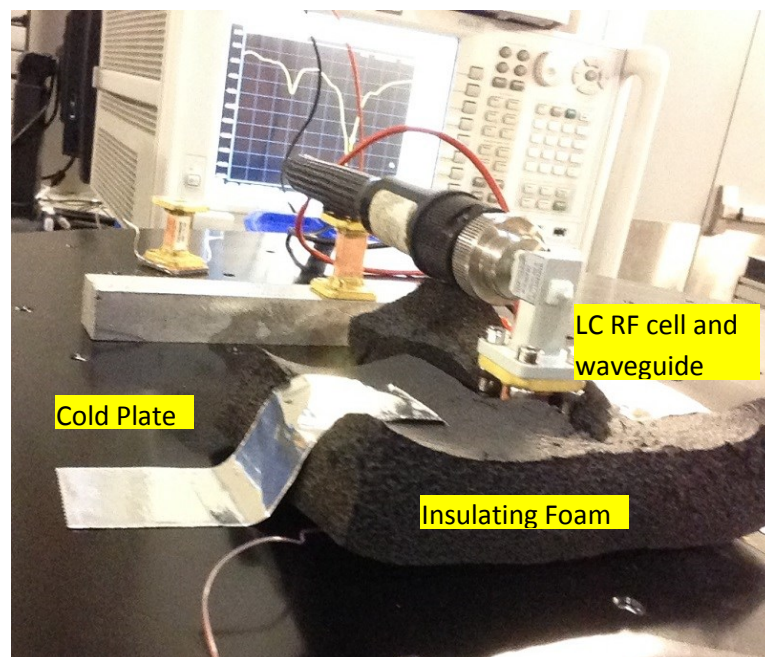


Figure 38: Phase shifter temperature test setup

Phase shifters were tested three times at each temperature and averaged to ensure that the entirety of the device was at equilibrium with the cold plate's temperature. In addition to multiple data sets at each temperature, devices were held for a minimum of ten minutes at a specific temperature before data collection was performed. Test samples using the BL006 LC failed to shift below 2C and after 50C. However the delta permittivity change over the temperature limit was minor resulting in a phase limitation of ~9 degrees of total shift loss. The sample cell was a 2x1 array and its return loss, phase delay, and overall temperature influenced phase deltas are shown in the following 3 figures.

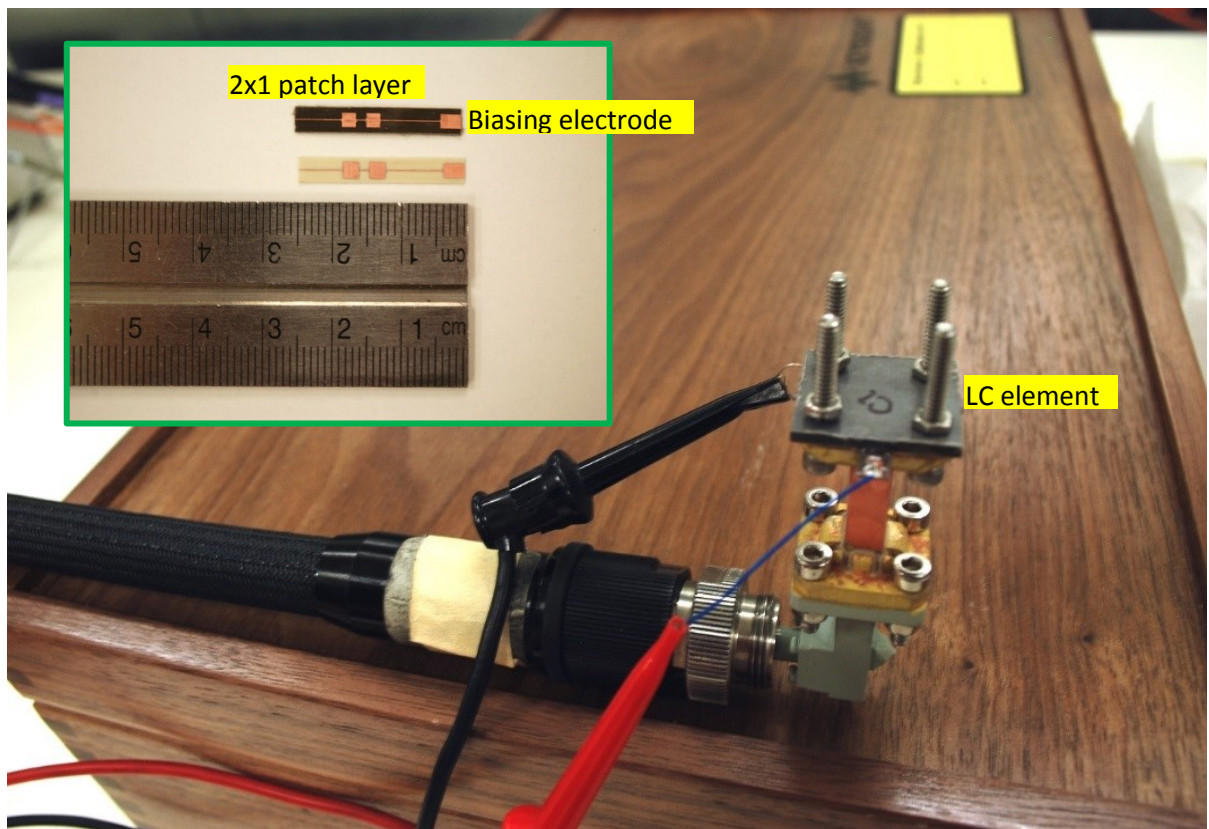


Figure 39 Sample setup and patch arrangement

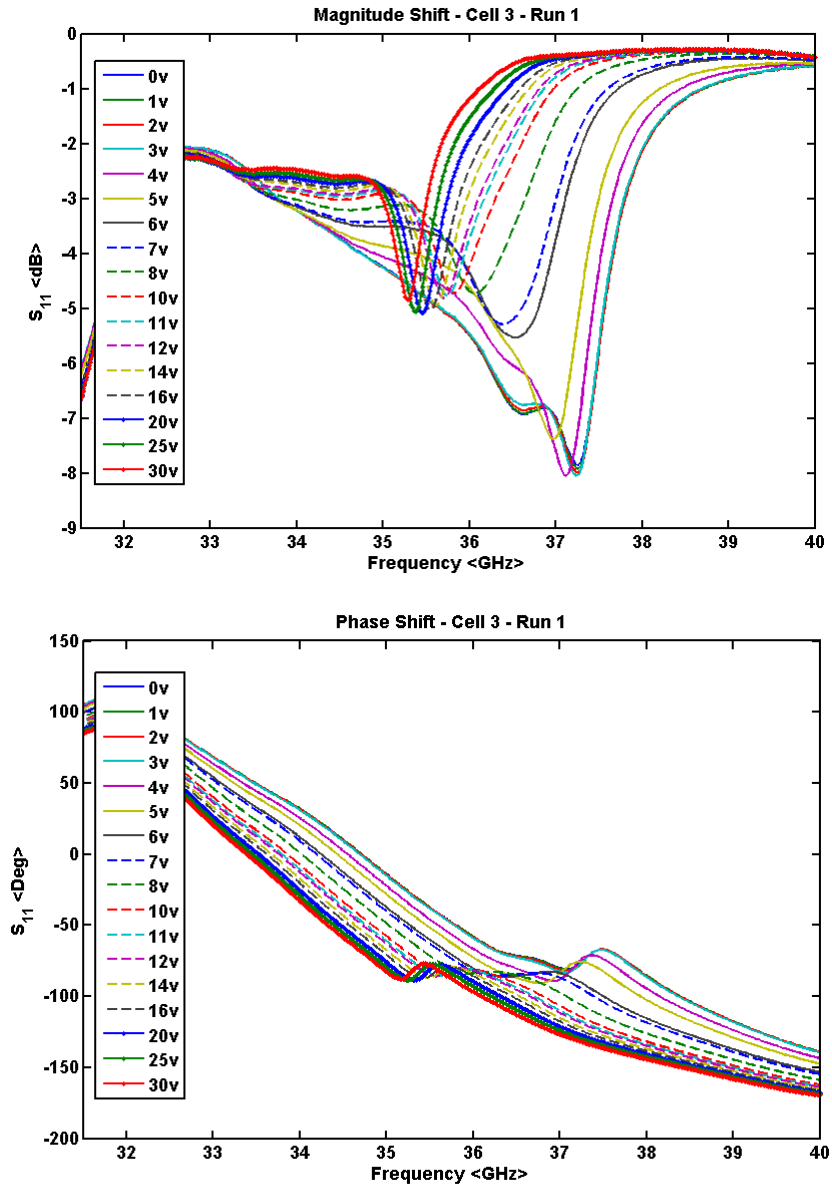


Figure 40 Return loss and resulting phase shift for the 2x1 LC reflector with BL006

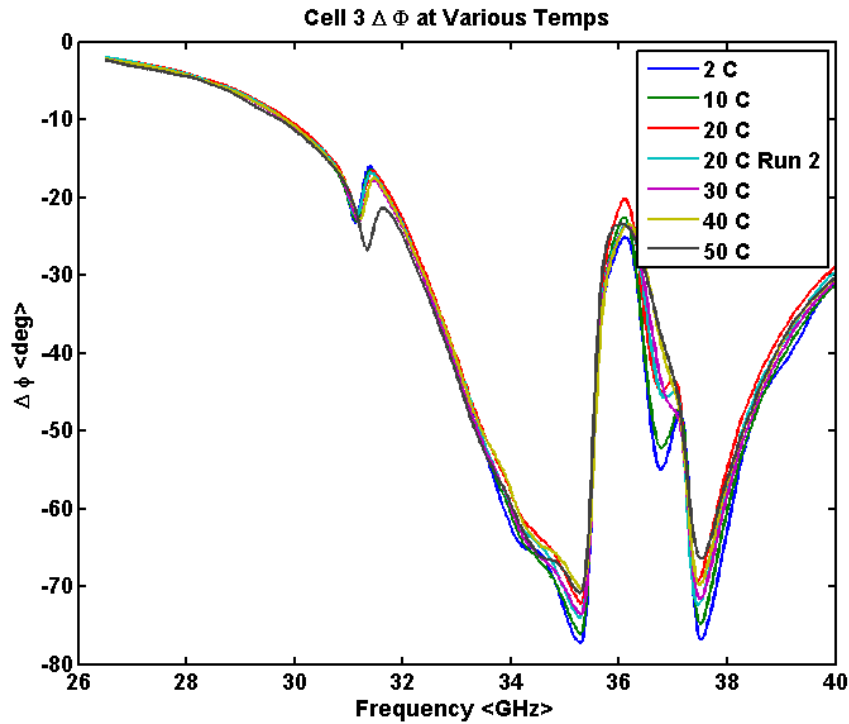


Figure 41 Phase delta over frequency range at various test temperatures

For this element, the thermal management support system would need to be designed to accommodate the limited thermal range of ~5 to 50C.

Mr. Chris Woehrle created a meander phase shifter using a higher performing blend of GT3-23002. The phase shifters used for this study were tested at eight temperatures in the range of -25 °C to 75 °C. Review of Figure 42 shows that the liquid crystal blend, GT3-23002 used in this experiment exhibited very little change in total phase shift at the tested temperatures. The 75°C data set has slightly less phase shift than the other temperatures; approximately 7° less than the average phase shift. The 7° difference in phase at 75°C translates to a ~13% decrease in phase shift tunability. The decrease in phase shift can be explained by the fact that the liquid crystal is becoming

more liquid like as the temperature increases towards the liquid crystal's clearing point (153°C), thus reducing control of the LC's anisotropy.

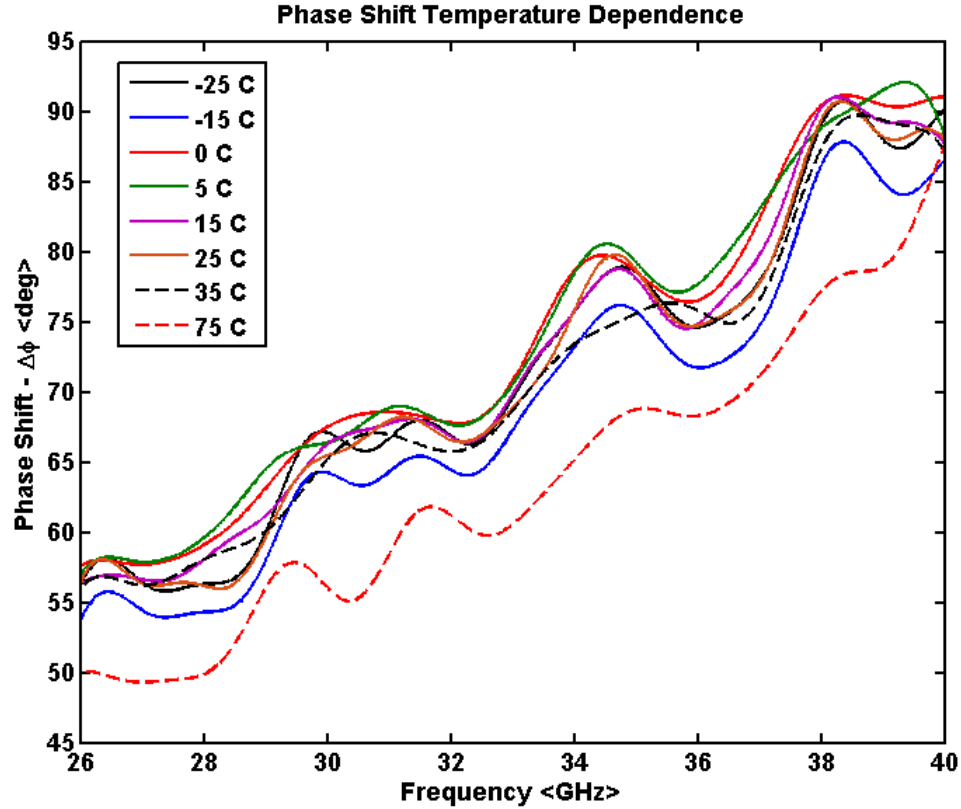


Figure 42: Measured phase shift as a function of temperature

Consequently, the greater the thermal performance of the LC, the less demanding the thermal management design needs to be. Switching times as a function of temperature are not trivial to capture, requiring a complex optical spectrum in-situ measurement that was not available. Still, several noteworthy observations were made that were consistent with theory. The phase shifters displayed a small decrease in switching time when temperatures were rose above room temperature ($T > 25^{\circ}\text{C}$). Then, when temperatures were lowered below ambient temperature ($T < 25^{\circ}\text{C}$) the liquid crystal showed slower

switching times. The magnitude at which the liquid crystal switched decreased significantly compared to the switching times when $T > 25^{\circ}\text{C}$ demonstrating a nonlinear temporal thermal relationship. It was observed that the liquid crystal switched on the order of 10's of milliseconds at temperatures above 10°C , and on the order of several seconds at temperatures below 0°C . Change in switching time behavior can once again be explained by the shift in material state as a function of temperature. As the liquid crystal begins to experience lower temperatures its material state transitions from a liquid crystal to more of a solid, which explains the slower switching speeds at lower temperatures due to the increase in restrictive forces against the liquid crystal molecules. The same thing can be said for hotter temperatures, but in this case the liquid crystal molecules are able to move more freely as the material state transitions to more of a liquid.

Increased temperatures can also cause materials to 'bake-out' and outgas. When a material outgases, trapped vapors and other particulates will escape. This can be a problem for spacecraft where those vapors then float around the system and condense on colder components which may impact performance. Traditionally, the rule of thumb is that the material must not lose more than 1% of its total mass and that it must not give off more than 0.1% condensable volatile material. However, other features need to be considered if a material will be acting as a pressurized container.

5.4 Vacuum Considerations:

All materials exposed to space must be able to withstand the harsh vacuum and minimize the amount of particulates that may come from the sample and may potentially recollect somewhere else on the system. Samples are typically exposed to $>1\text{e-}6$ torr vacuum and cycled between the expected operational temperature range. For a Low Earth

Orbit mission, this may be -20C to 80C. Most RF materials meant for space applications have already gone through this form of testing and been tailored to survive with minimal material change. 3D printing materials are not as well tested. One particular form of ABS that claimed to meet NASA outgassing requirements (ASTM E-595-93) of <1% Total Mass Loss (TML) and <0.1% Condensable Volatile Material Loss (CVML) was printed to make a 5GHz patch antenna. While four samples utilized copper tape, an additional four were coated with an RF paint. All samples were put under 5e-6 Torr vacuum for one week. The painted samples remained at room temperature while the remaining were attached to a cold plate and driven to temperatures of 25C-95C during facility operational hours to assist outgassing. The following figure highlights the observations made of the material.

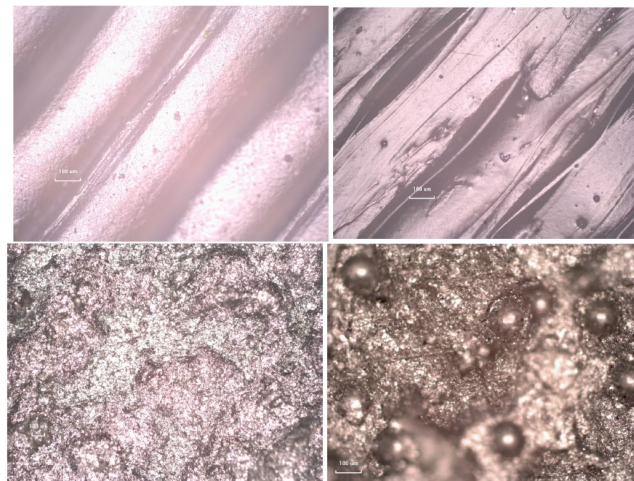


Figure 43 Optical microscope measurements made before (left) and after (right) thermal-vacuum testing where images show printed (top) and paint (bottom) effects.

One inconsistent feature seen in the samples was warping of the samples that were heated. This was an expected feature to find as the elements were not mounted to a

backing structure, such as a honeycomb composite plate to maintain stiffness during thermal transitions. However, the images capture a more troubling phenomenon. Many printing approaches utilize Fused Deposition Modeling (FDM) where printable strands are passed through a heater head to prep the strand for layering in the structure. As the filament is heated and cooled, it collects water vapor inside the structure and in the strand. When the sample is put under vacuum, the trapped water escapes creating cracks in the strands and between the bonded layers. For an LC cavity, this will risk creating fissures for the LC to permeate through as many blends have strong capillary forces and a high degree of wetting. Coating methods like epoxy infiltration may be possible sealing approaches depending on the cavity approach used but also can fill capillary channels and LC reservoir spaces.

The effect of this outgassing had a major impact on the conductive MG silver epoxy applied to the samples as well. The trapped gas came up under the paint causing some spots to bubble and pop. Overall the painted structure was cracked to the point of reducing surface conductivity from $17.4 \text{ m}\Omega\text{-cm}$ to effectively $>1\text{M}\Omega$ as the 4-point probes became unable to consistently find sufficient path conductance. As a result this type of conductive layer should be avoided to preserve surface conductivity.

For the non-painted samples the outgassing changed the resonance of the copper patch antenna. As water returned to the system, the radiation pattern shifted back 40MHz to the starting frequency. It is believed that as water vapor returned to the sample and replaced the nitrogen backfilled gas residing in the material, that a small change in the substrate's dielectric properties occurred restoring permittivity. This can be seen in Figure 44.

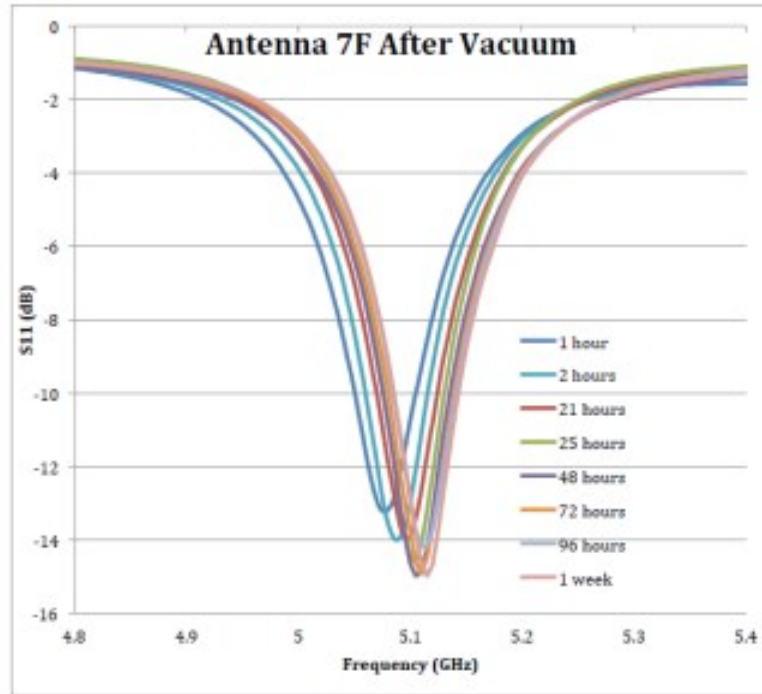


Figure 44 Antenna sample (7F) reflection parameter over time after vacuum exposure

These effects will only get worse for FDM materials that work with higher temperature plastics like Ultem or PEEK. The author recommends that 3D printing practices for RF consider nitrogen chambers for manufacturing to remove moisture from the build and that parts be printed such that the cavities are not formed until the parts are pressed together allowing infiltration and coating methods to be used to better hermetically seal the part.

Further research is needed to understand the role of coefficient of thermal expansion differences between the assembled materials to assess the likelihood of crack formation and propagation as well. In terms of the LC, researchers must understand the relationship temperature has on the viscosity of the LC substrate as reduced temperatures will certainly increase the viscosity of the material. If researchers wish to mitigate the wetting of a nematic LC, than polymerization may be an effective approach to mitigate flow

through possible cracks. However, increasing viscosity will lead to a higher Fréedericksz transition requirement but can also increase the turn off transition time.

CHAPTER 6: RADIATION/CHARGING CONCERNS FOR RECONFIGURABLE

LiCRas

6.1 Introduction:

By far the number one source of hazards to a spacecraft comes from the phenomenon discussed in this chapter. Space systems have been impacted by a variety of factors from poor design, poor processes, unexpected collisions, and predominantly Single Event Effects (SEEs). These events are electrical anomalies that can be caused by a number of sources and have unpredictable results. Ideally a system is designed around materials and electronics that are damage resistant to SEEs, meaning they don't breakdown or permanently latch-up making them inoperable on orbit. These events are usually caused by the interaction of some high energy particle colliding with the spacecraft. Even a micro size piece of debris carrying a different potential can unleash greater damage from the ionized collision between bodies where the released EM pulse can be more devastating than the mechanical damage done at the crater site. This is due to the pulse propagation following any unknown conductive path to any unknown electrical component and possibly forcing some operational state change.

To reduce the concerns associated with new materials in space, researchers will utilize available sources of high energy particles on the ground to see how materials respond to different forms of particles and energy levels. These interactions may be fully penetrating where the proton/neutron/heavy ion/etc. rips into the material releasing localized energy able to break molecules apart. When this happens, the material properties change (optically, electrically, mechanically, even geometrically) which may result in the material no longer performing its needed function. To some extent this is

acceptable. The cover glass of a solar cell darkens over time making the cell less efficient. Designers use test data to build spacecraft that can perform even with a degraded end of life performance.

Some particles, like electrons, can also penetrate a material and release secondary bremsstrahlung radiation, but an additional concern is with trapped and deposited surface electrons that charge the spacecraft. Seeing as each system is a collection of metals and dielectrics, eventually each system obtains its own unique charging profile and average potential. If this charge is too great on a given material, the material will fail and spark, thus creating the release mechanism for an SEE. The charge build up may also interfere with other measurement devices if not mitigated. The important factor to understand with a new material or component is how it charges and if it can operate under this charged state. To understand the concept of charge buildup and mitigation, the writer suggest considering a common differential equation example of a water tank with an inlet hose and a drain pipe.

The tank is the dielectric with a volume constrained by its dielectric breakdown property. The inlet hose is the space environment dowsing the system with charged particles. The outlet hose would be the ground plane sync where the rate at which charge can leave the sample is controlled by the material's radiation induced conductivity. If the inlet hose fills the dielectric with charge faster than the material can move it to the ground, then the material is not suitable as it will discharge. Ideally the material should reach some average steady state where it moves charge as it is deposited and reaches a steady standing voltage potential as charge flows through.

That standing static charge is of great concern to reconfigurable components. The reason is that these approaches utilize DC voltage biases to perform switching. If orientation, mitigation, or tolerance are not understood and designed into a reconfigurable material there may be a variety of unknown states possible in a reconfigurable medium or device. For now, the author will focus on the easier problem of radiation degradation in LiCRAS candidate materials and will then discuss charging.

6.2 Radiation Effects on LiCRAS:

Research here was focused at electron exposure levels relevant to GEO space exposure. Sources examined included X-ray, Cobalt, and Strontium 90 (Sr-90). While the flash X-ray and Cobalt sources allow for rapid aging of lower energies below 150 keV to provide total ionizing dosages (TID) of up to 1Mrad in less than a day, they are not as suited for doing relevant in-situ effects testing. Sr-90 simulates the higher energies of GEO in the MeV range and can be performed in a simple low Z shielded atmosphere with minimal risk for live measurement tests. All sources allow observers to monitor the impact of various ionizing particles on candidate space materials and assemblies.

As charged particles bombard a spacecraft, the energy is reflected, absorbed in the material, or transmitted through if the energy is high enough. These particles interact with the material and can cause damage in certain polymer molecules by separating molecular bonds. While the effects may be recoverable with heated annealing, it may also change the properties in terms of mechanical and electrical parameters of particular bonds by breaking molecules into any of the possible constituents of the complex molecule. To better understand this, consider a common space dielectric such as Kapton. The chemical

name for Kapton is known as PMDA-ODA, or poly-(pyromellitic dianhydride-4,4'-oxydianiline) and has a chemical structure as seen below [75].

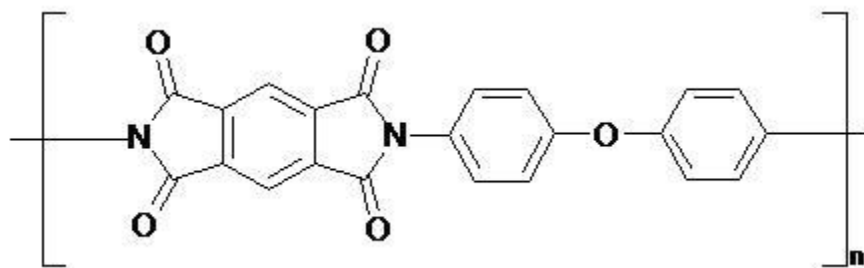


Figure 45 Chemical Structure of Kapton

Understanding the molecular degradation of these types of molecular chains is still relatively unexplored and difficult to perform. Additional research is currently underway as of the time of this writing specifically to attempt to better understand this. From discussions with the principal investigator for the effort, Dr. Ryan Hoffman [76], the challenge with understanding material degradation is that there are no absolute trends and each material behaves in unique ways. The energies of radiated particles almost universally exceed all bond energies in a molecule so if any part of the molecule gets hit, it can break. It's then a matter of statistical likelihood of if that broken bond will be ionized in such a way that it restores or falls apart. In order to properly characterize all the pieces coming off a material requires multiple complex processes to understand the molecular ratios of outgassed particles present, Fourier Transfer Infrared Spectroscopy FTIR and X-ray spectroscopy to understand the particles left on the material that stay crystalized or stuck to the substrate, and newer approaches still under development. For most materials, this low level understanding is sufficient because the material is built as a bulk material and able to withstand the small amount of degradation over the 5-20 year spacecraft lifetime. More often the concern is for understanding risk to nearby sensitive

sensors that may be corrupted by emissions for an unknown material. When the phenyl rings are broken on Kapton for example, it releases primarily hydrogen, carbon monoxide, and carbon dioxide gasses. As a surface coating, this is not typically a mission critical problem. However, for LCs, this may be a difficult design problem for encapsulated cavities of LC where gasses may build up and apply pressure to the assembly. This further drives the need for isolated reservoirs rather than large chambers spanning multiple radiating elements. The author suspects that this is mitigated through designing a substrate which can permeate molecules as large as these gasses of concern.

Unfortunately the providers of commercial LC blends are not willing to provide molecular structural information so it is difficult to offer a guess as to all the possible constituents that may develop for LCs under radiation. However by studying the results of LC reviews discussed in Chapter 2 we can see that most LCs are a mixture of phenyl and biphenyl rings with other acrylates and particles to help tailor electrical and optical properties. Therefore, it is very reasonable to expect similar gasses to form from the LC when bombarded with radiation. The real challenge is capturing the beginning and end of life parameters and if there is substantial degradation to pollute the dielectric with sufficient ionization to make it either degrade or not function at all.

As nematic LCs have already been shown to hold up to TID, X-ray, and fast neutron radiation [77], we focused on the printed substrate that may house the complex LC fluid channel and cavities and built up a single element test unit with all parts required for an LC reflector.

One of the first tests was looking at fully penetrating electrons. A Strontium-90 source is used to provide this spectrum of beta particles and is advantageous due to its

low shielding requirements of Plexiglas and air. However caution is needed for shields containing higher density particles like aluminum or copper as these slow down the electron to fast creating secondary radiation of gamma rays that are more hazardous to nearby staff. The profile of Strontium is seen below.

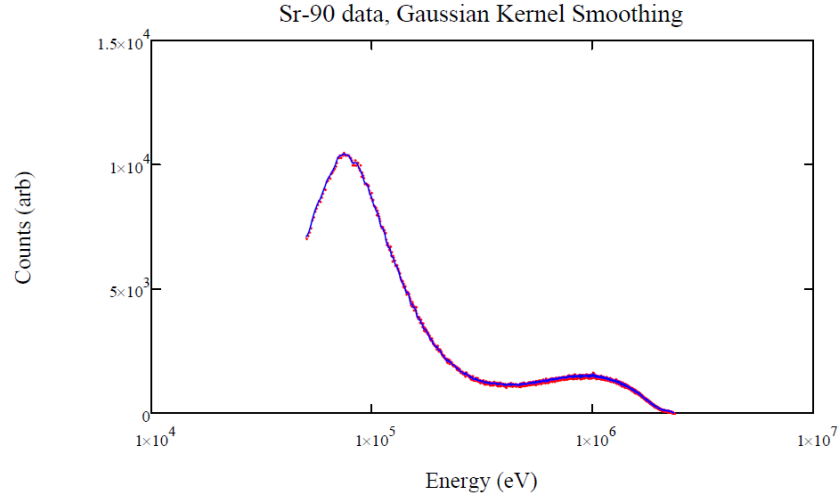


Figure 46 Lithium-drifted Si charged Particle Detector, Baltic Instruments SPD 200-5, measurement of Sr-90 source.

This profile indicates the flux of electrons over the energy spectrum from 80 keV to ~2MeV. This profile diminishes with distance squared from the source to the sample. If we consider the distance from the source, d , radius of the disk, R_s , and area of detection on a sample, A_d , then the area of interest, R_d , can be determined as

$$R_d = \sqrt{\frac{A_d}{\pi}} \quad 24$$

and the solid angle of the source, Ω , is found as follows [78],

$$\Omega = \frac{R_d^2}{4d^2} \left[1 - \frac{3}{4} \left(\frac{R_d^2 + R_s^2}{d^2} \right) + \frac{15}{8} \left(\frac{R_d^4 + R_s^4}{3d^4} + \frac{R_d^2 R_s^2}{d^4} \right) - \frac{35}{16} \left[\frac{R_d^6 + R_s^6}{4d^6} + \frac{3}{2} \frac{R_d^2 R_s^2}{d^4} \left(\frac{R_d^2 + R_s^2}{d^2} \right) \right] \right] \quad 25$$

The total output of the source is determined using a detector to calculate the curries of the source and based on the electron charge the output of the Sr-90 disk is defined for this setup as 0.190 Ci or current of 1.126nA. The total flux on a target spot is then captured as

$$J = I\Omega/A_d \quad 26$$

To capture the differential flux on a sample you need to multiply the total flux by the ratio of the area of each increment of the total area under the curve profile shown in Figure 46. The profile from above can now be compared to other measurements for comparing representative intensities from other space measurements and is shown below for a sample placed 12 inches away from a 2.5cm Sr-90 disk.

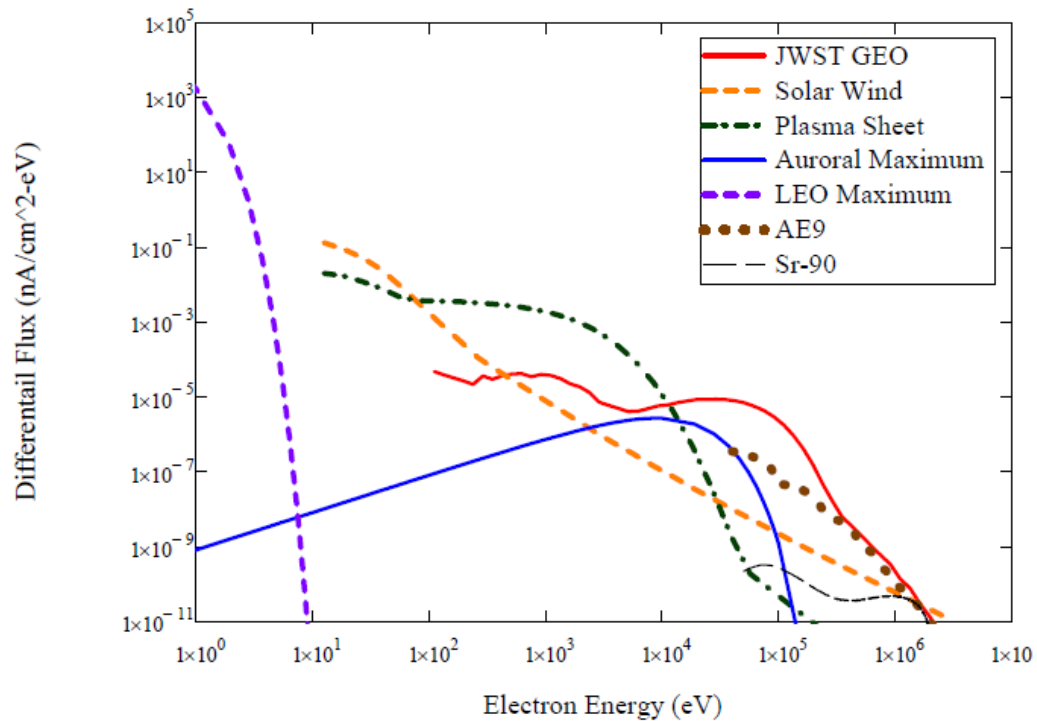


Figure 47 Sr-90 illuminated spectrum compared to other sources for space measurements

Once the flux is known for a particular spacing, materials can be placed to either rapidly age or simulate reduced space fluxes. Stereo-lithography (SLA) ABS samples were prepared and exposed to the equivalent of 2-5 days of GEO exposure in terms of the

higher energy spectrum around 100keV while closer to 1-2 months in regards to energies near 1MeV. This can be obtained by comparing the electron flux emissions of Sr-90 to that of an AE9 model of the GEO fluxes. Exposure caused visible warping in larger thin sheets, which is indicative of bond breaking in the polymer substrate. This expansion of the dielectric caused layer interfaces to dislocate and created fissures of up to 35 μ m wide to form. This expansion would likely crack parylene coatings traditionally applied to electronics and would allow a fluid cavity to depressurize.

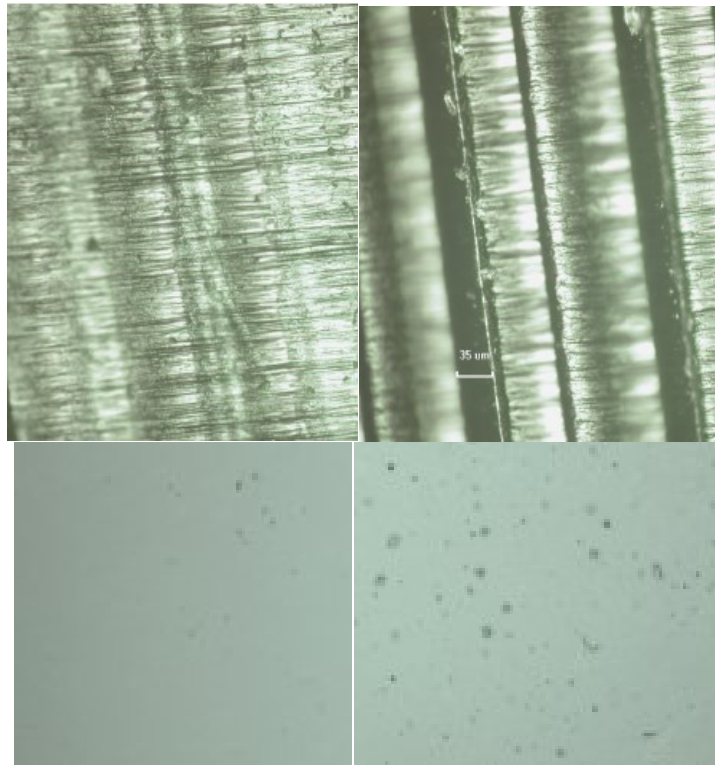


Figure 48 Printed substrate before (left) and after (right) Sr-90 exposure illustrating the manifestation of defects. The top picture is for between printed layers while the bottom shows a single layer with increasing defects.

The rate of LC leakage through such a defect would be dependent on how far the defect permeates into the vessel, the pressure differential between the LC cavity and the external vacuum, the temperature of the LC which will affect its viscosity, and the tortuosity of

the crack (is it a straight through penetration or are there a lot of curves. While the crack opening in Figure 48 indicates a 35 μ m gap, there is layering between the printed channels that reduce this gap and may help minimize leakage of the internal fluid channels. While ABS is not a suitable RF dielectric due to its high lossiness, see Chapter 4, it does give an idea of what problems to expect. The authors looked at more common RF dielectrics that may one day be available in either an SLA type solution or filament for deposition modelling.

Duroid and Rogers samples were tested next. No noticeable effect was seen from Sr-90 exposure. The next step was then to take the sample to more intense exposure to accelerate the aging/degradation potential. A cobalt-60 chamber and X-ray source were considered and setups took multiple samples of the two candidate materials and placed them at varying distances to vary the total dosage from a 100 rad to over 1 Mrad or covering a mission range of 2-15 years. These rapid tests are somewhat misleading if materials degrade and are more useful for identifying good materials that see no change. If a material does change there is the chance that the rapid nature of the test exceeds the flux which the material can handle and although it may fail on Earth, it could survive space just fine. Never the less, it gives an idea of the possible deteriorations that can occur. The Cobalt and X-ray setups are seen next. In addition to material tests, an LC cell using the Duroid dielectric and a copper patch/ground plane was also tested.

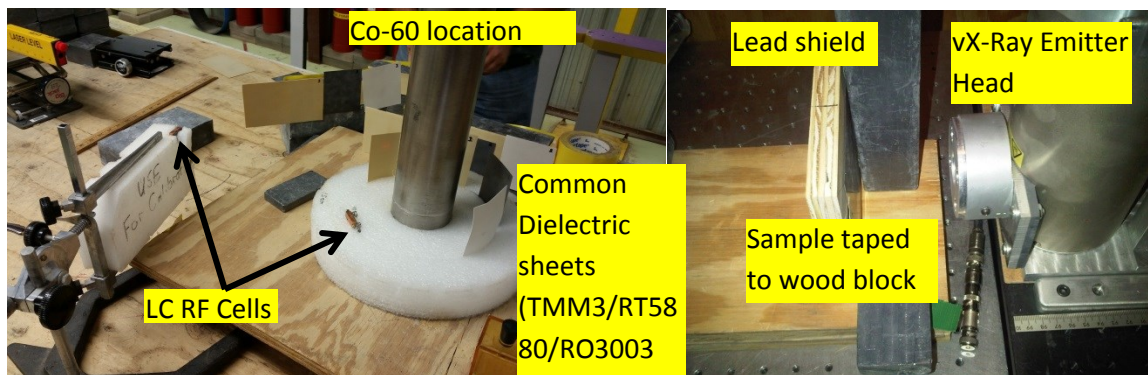


Figure 49 Pictures of Cobalt (left) and X-Ray (right) setup for the exposures on the samples.

Prior to exposure, each sample had its dielectric properties tested to be used as a reference and were characterized visually using an optical microscope. RF properties of the dielectric samples were tested by waveguide extraction technique (ASTM D5568-08) as seen in Figure 50.

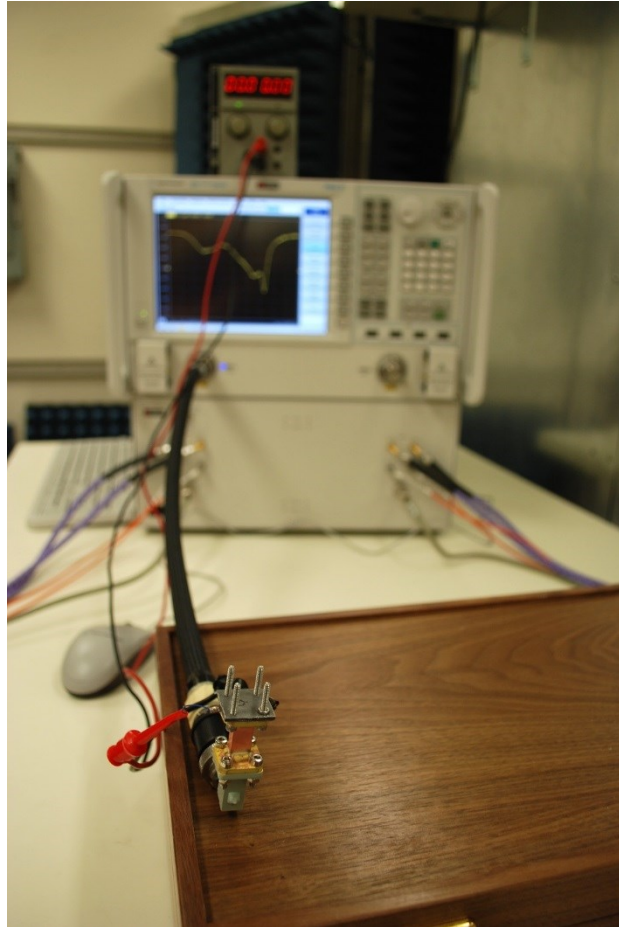


Figure 50: Material Characterization setup; Dielectrics Tested: Rogers RO3003 (Ceramic-filled PTFE), Rogers RT/Duroid 5880 (Glass woven PTFE), Rogers TMM3 (Thermoset ceramic)

Comparison of data collected before and after exposure showed little to no negative impact from exposure at 50 keV and 140 keV energy levels on the RF properties of the dielectrics tested. Visual inspection of the surfaces revealed no significant change to RO3003 and RT/Duroid 5880, but TMM3 showed some small differences which may indicate some material damage. TMM3 samples also displayed significant embrittlement (extremely fragile) after exposure to radiation, which alludes to bond breakage within the

polymer. This can lead to significant risk of assembled structures to tolerate thermal cycling.

All materials exposed showed no change in permittivity (ϵ_r) and loss tangent ($\tan \delta$) in the Ka-band. VNA measurements showed that values for permittivity and loss tangent at Ka-band frequencies are well within the 2% margin of error inherent to the waveguide extraction testing technique. RO3003 and RT5880 showed no change in RF properties at E-band frequencies, but TMM3 showed some change after exposure to 50 keV and 140 keV energy levels. The TMM3 samples showed roughly 6% change in permittivity (ϵ_r) and loss tangent ($\tan \delta$), which would agree with notion of bond breakage or re-bonding effectively changing the polymer properties of the dielectric. Overall, RO3003 and RT5880 dielectrics showed no visual or RF change when exposed, and would make a good candidate for applications operating in harsh radiation environments.

Duroid materials seemed to tolerate the lower dosages but higher dosages made the Roger TMM3 more brittle and showed a 6% reduction in permittivity and change in loss tangent at frequencies above 60 GHz into the E-band range. However, the problem with an accelerated exposure test is that materials are not given the chance to anneal naturally in the manner they may had they been in the actual environment through thermal cycling and varying exposure rates or reduced magnitudes. This test made the Duroid 5880 stand out as the better material.

As the Duroid RT 5880 sample proved to have the least damage and change after material exposure tests, it was used to build a sample LC reflectarray and phase shifter cell. In addition to the molecular damage that can be done by radiated particles there is a secondary concern that is of importance for reconfigurable anisotropic materials or other

switching approaches like MEMS, varactors, PIN diodes. That problem comes in the form of spacecraft charging.

6.3 Charging Considerations:

The primary particle responsible for charging a spacecraft is electrons. As these particles come into a substrate they deposit a constant amount of energy along their path and if they stop in the substrate, they release a larger magnitude corresponding to the remaining potential of the electron dictated by its electric potential. One area of research that is still not well understood today is how this charge migrates through a complex structure consisting of various dielectric and metallic interfaces. However to understand this it may be best to split the problem up. Consider a point source of charge entering a dielectric substrate with a conductive grounded base. From Gauss Law we know that similar charged particles will diverge from each other. This point charge comes from a beam with current 10 nA/cm^2 and with an electric intensity of 20 keV (typical LEO values). The beam interacts with a common dielectric such as Kapton with a density of 2.2 g/cm^3 , thickness 2.5 microns , and relative permittivity of 3.9 . To determine how far such a beam would penetrate into a substrate we rely on open literature [79-83] and is summarized in the following discussion. The problem was simplified into NUMIT and TIGER codes by authors as reducing the sample mass to its nearest elemental slab and categorizing materials based on the principal atomic mass. From there the problem of understanding current density, $J(x,t)$, resulting electric field, $E(x,t)$, the stored dielectric charge density, ρ or $\rho(x,t)$, and the replacement current density on the grounded back electrode, $I(t)$.

$I(t)$ is tracked by the integral of current density across the dielectric thickness, d , and normalized to the thickness as follows,

$$I(t) = \frac{1}{d} \int_0^d J(x, t) dx \quad 27$$

The current density associated with highly energetic electron migration, $J_r(x, t)$ is dictated by the materials radiation induced conductivity, g_{rad} , and the conductivity of the material once the source is removed, or the dark conductivity, g_{dark} . The flux of the incoming radiation defines the dose rate profile, $D(x, t)$ in a dielectric. These are all collected into the total current density:

$$J(x, t) = J_r(x, t) + (g_{dark} + g_{rad} D(x, t)) E(x, t) \quad 28$$

The dielectric charge density can then be obtained via the current continuity equation as

$$-\frac{\partial \rho(x, t)}{\partial t} = \frac{\partial J(x, t)}{\partial x} \quad 29$$

and the electric field is captured through Gauss's law (Poisson equation for source as a potential) to from the dielectric charge density as

$$\frac{\partial (\epsilon(x) E(x, t))}{\partial x} = \rho(x, t) \quad 30$$

Where dielectric permittivity, ϵ , is the product of the dielectric constant and the free space permittivity. The solution requires an iterative solver to converge on the right values. From this point the models make use of the Tabatha algorithm [82] for identifying and calculating fitting parameters (β , A , B , C , D) in the normalized radiation current density, $J_r(S)$, and conditioned as a function of the substrates atomic number, Z , as follows:

$$\beta_c(Z) = 1.7234 + 2.3092e^{-0.23188Z} - 0.6241e^{-0.0062431Z} \quad 31$$

$$A_c(Z) = -0.036183 + 0.75822e^{-0.065448Z} \quad 32$$

$$B_c(Z) = 1.1357 + 0.44169e^{-0.10695Z} - 0.5613e^{-0.023236Z} \quad 33$$

$$C_c(Z) = 0.25231 - 0.18103e^{-0.044663Z} \quad 34$$

$$D_c(Z) = -0.247 + 0.059348Z - 0.0018299Z^2 + 2.4967E - 5Z^3 - 1.1457E - 7Z^4 \quad 35$$

While these codes have been developed for years to understand the impact of charge transport through a bulk simple material, they are noted as still needing improvements for time delay nature of RIC, deposition profile algorithms that are not 2 decades old, multi-layered components (as is the case with an encapsulated LC), and isotropic incidence. While the modeling of this phenomenon in a complex RF component are likely not to be 100% accurate, it should identify trends of concern. To that matter, a finite element Matlab script was written to illustrate the possible current, charge density and electric potentials that are traversing an LC RF element.

The first step was to look at the problem as a single charge source to make sure the progression of charge distribution followed Maxwell laws on divergence of charge from gauss's law, or that if we put a concentrated distribution of electrons at a point in a dielectric we would see them flow out in all directions and trend toward the ground. The code written for this is provided in Appendix A. This code was written using equations and assumptions outlined in NUMIT and TIGER code papers and should in no way be considered complete.

The code written considers an LC arrangement where a dielectric material such as Teflon or Kapton is layered with an LC cavity and with a conducting patch and ground plane. The beam is treated as a point source and illuminated for 0.5 seconds depositing 20keV incident energy at 10 nA/cm². The result charge profile will create a region of increased radiation induced conductivity that will establish the flow of electrons. The depth of deposition is derived from NUMIT and Tabatha algorithms. The next two

figures will show the RIC, Charge density(ρ/cm^3), and field vectors from the deposited charge.

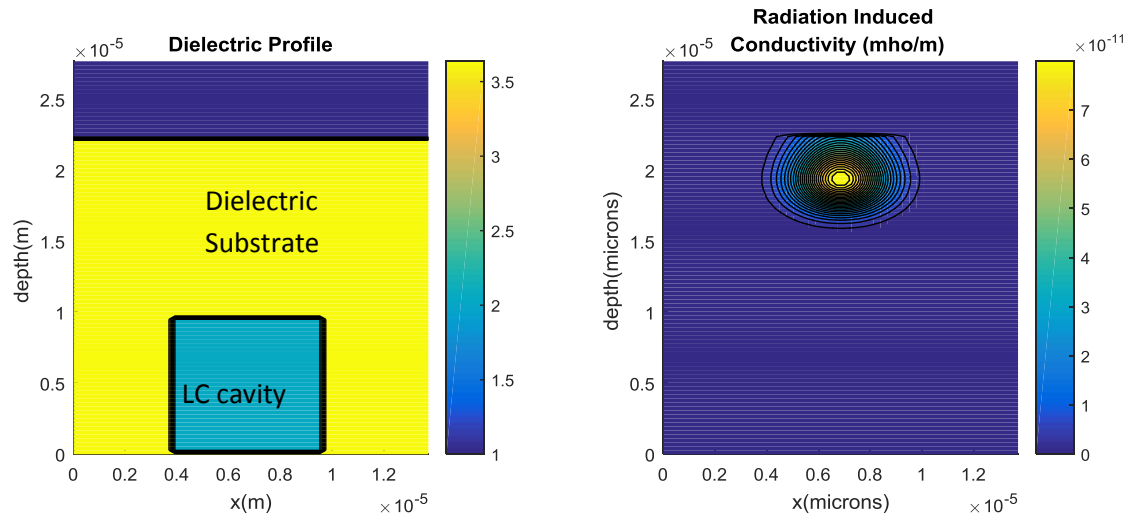


Figure 51 Modeled dielectric LC Profile (left) and the illuminated spot beam creating a charge deposition within the substrate (right)

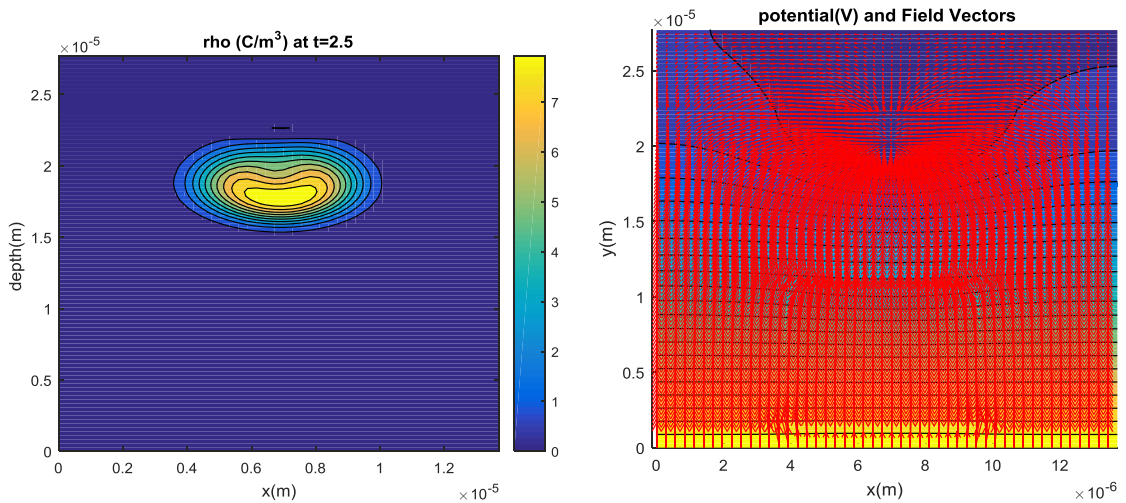


Figure 52 Modeled dielectric charge density (left) and resulting field vectors (right) 2.5 seconds after illumination.

As time progresses, the charged spot disperses through the material. The rate is slow enough that the resulting magnetic and electric field influences on a GHz wave may be

minimal, but the LC would certainly be expected to respond. Below is the same plots 30 seconds later.

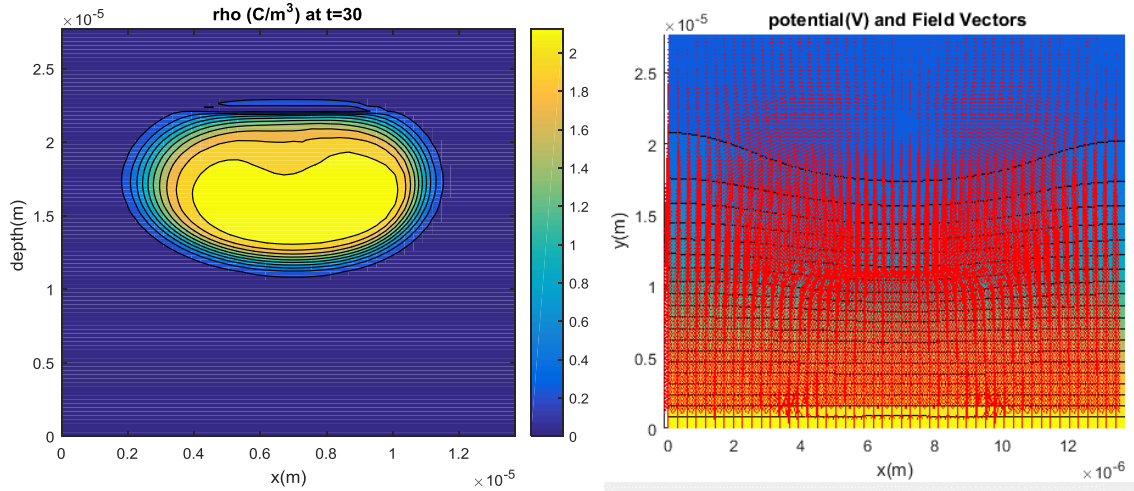


Figure 53 Modeled dielectric charge density (left) and resulting field vectors (right) 30 seconds after illumination.

The iterative model shows that as the charge expands outward, the magnitude of the charge density reduces along with the associated field vectors. Additionally we see the vectors trend toward a normal pointing arrangement, with the exception of the corners of the conducting patch where a point charge is maintained. Now that we know the physical trends are maintained we can focus on the influence of a sheet distribution of deposited charge. Consider the flux of electrons like rain on the ground where drops of charge randomly hit the material and settle in a confined universal depth given a specific energy band. To do this, the Gaussian distribution condition is removed from the beam setup function of the Matlab code. The same problem space is now seen as follows.

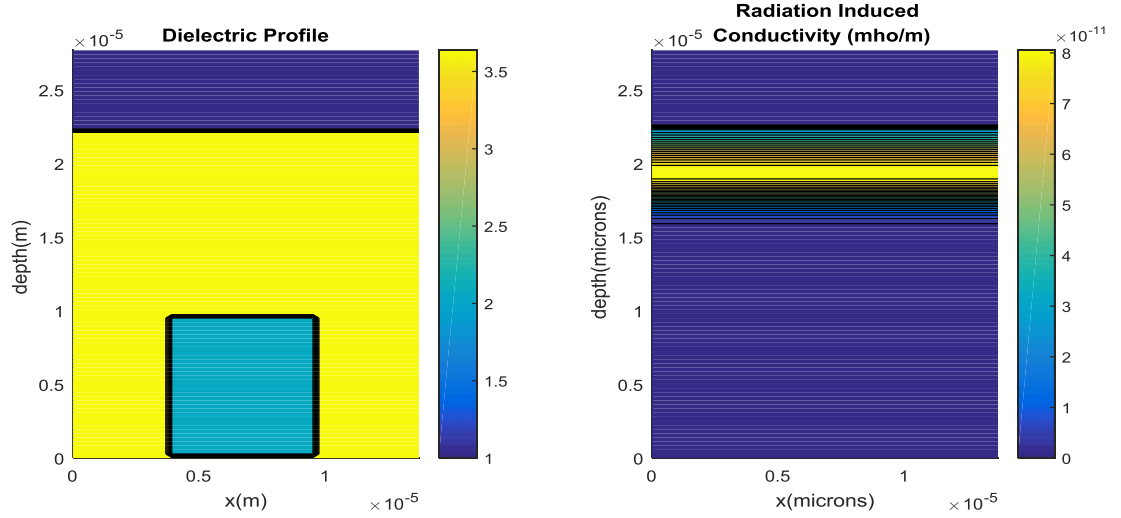


Figure 54 Modeled dielectric LC Profile (left) and the illuminated sheet beam creating a charge deposition within the substrate (right)

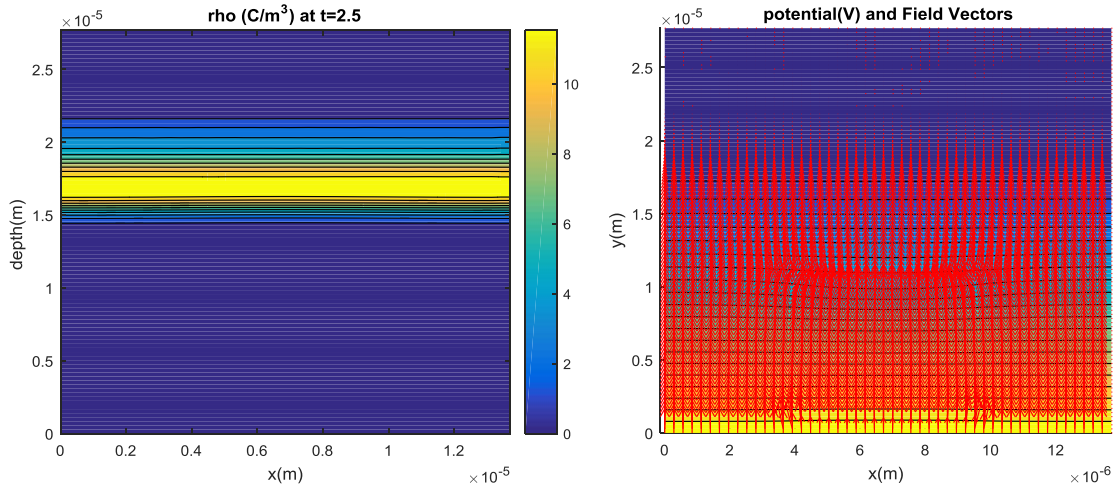


Figure 55 Modeled dielectric charge density (left) and resulting field vectors (right) 2.5 seconds after illumination.

It should be noted that this model only captures a single energy band. In actuality, a broad spectrum is present in space, as shown back in Figure 47. What is interesting here to monitor is the increased rate of distribution as a result of a larger initial charge distribution that allows for the charge to migrate faster through the substrate. The below

figure shows the iterative model 30 seconds later and shows how increased distribution and increased exposure depth will allow the substrate to reach a point of equilibrium faster than with a single penetrating particle.

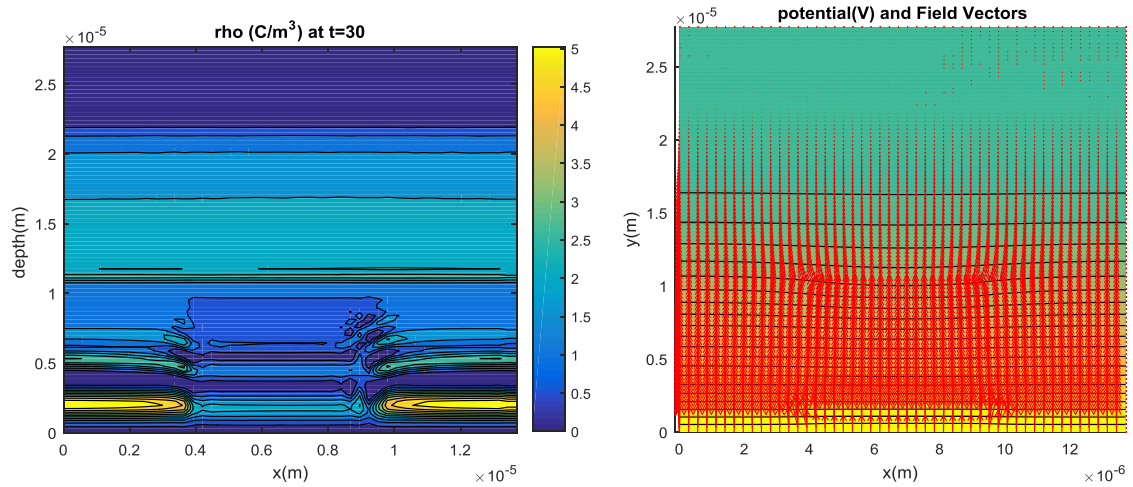


Figure 56 Modeled dielectric charge density (left) and resulting field vectors (right) 30 seconds after illumination.

From these results it seems that a true LC RF element would have to be expected to experience some impact from the initial illumination of electric radiation that can occur during solar storms or entering/leaving eclipse. It seems that for a traditional arrangement, this may require less than a minute depending on the thickness of the material, but what is of concern is the observation of field potential vectors in the LC region. Since LC is an anisotropic material with permittivity controlled by static fields it is now necessary to see if these fields are strong enough to exceed the Fréedericksz transition limit and certainly how it may add to any controlled bias.

To do this, the author wanted to consider the proper candidate materials. From previous radiation experiments, it was seen that Duroid 5880 and Rogers TMM3 represented possible RF substrates for terrestrial uses where only the 5880 seemed to

tolerate simulated space testing. To this end, both materials were evaluated to identify their radiation induced conductivity to better understand what kind of migration to expect and what level of standing voltage to expect.

The Jumbo test chamber, seen in Figure 57 was built at AFRL to address the challenges of ground-based spacecraft charging tests. The chamber is capable of pumping the ~4.8 kL volume from atmosphere to a base pressure of 10^{-7} torr in a matter of hours. This chamber is also outfitted with Helmholtz coils for nulling the earth's magnetic field. Currently under design is the addition of a thermal shroud and plate cooled with liquid or gaseous nitrogen to simulate thermal extremes in addition to vacuum.



Figure 57 Custom built Jumbo chamber for simulated space exposure

Within this chamber, a rotating sample holder is placed to accommodate multiple materials for charge testing. The sample holder is illuminated with multiple sources depending on the environment and spectrum of interest to include a high and low flux electron beam gun, an ion gun and ultraviolet lamps. The sample holder is rotated to help

normalize the Gaussian flux that is distributed from the spot beam illumination. A non-contact probe was placed 1mm above the samples to measure the standing voltage potential on the surface. This setup is shown in the following figure.

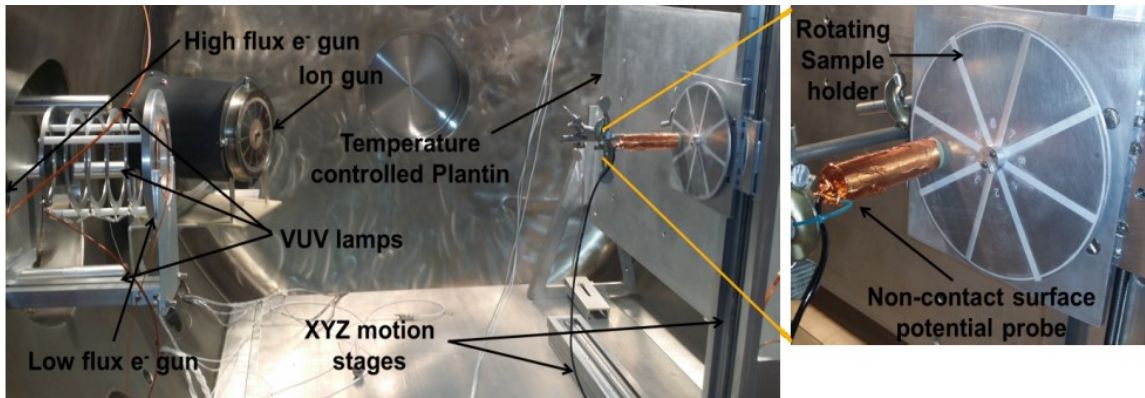


Figure 58 Chamber test hardware in measurement setup

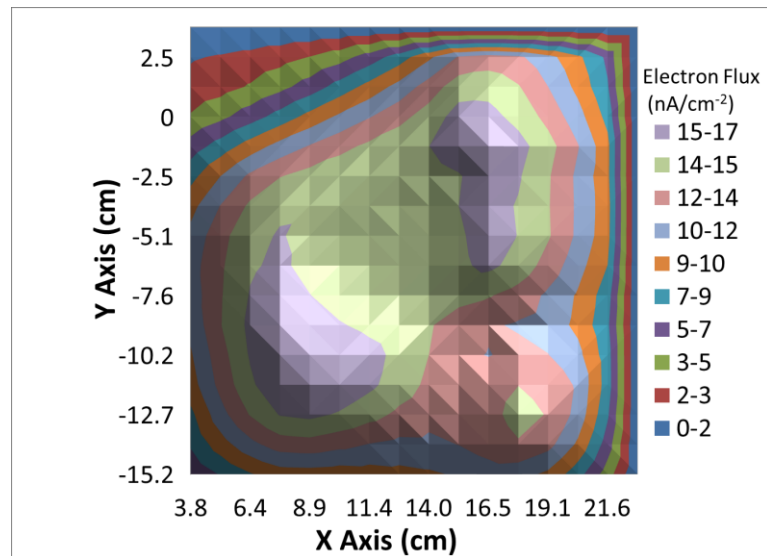


Figure 59 distributed electron flux from test sample used for calibrating chamber.

Samples of the 2 materials were exposed to vacuum charging and exposure to a 20keV source. The TMM3 sample will be discussed first as it shows what happens when materials are not properly chosen. The next two graphs will show how the TMM3

charged up as sample exposure time increased. Instead of tracking time, the system tracks charge distribution over area. In the associated plots, the dots are physical measurements from the system. The computer running the hardware then fits the points to a logarithmic function defining its charge or discharge profiles which can then be used for model inputs or understanding how the material will behave in a charging environment.

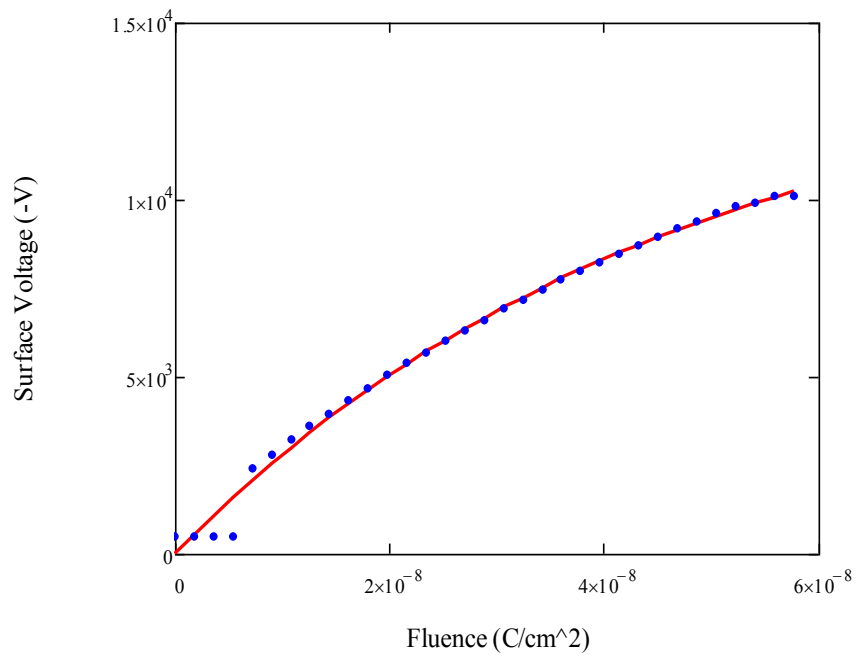


Figure 60 Standing charge on TMM3 with increased charged particle exposure.

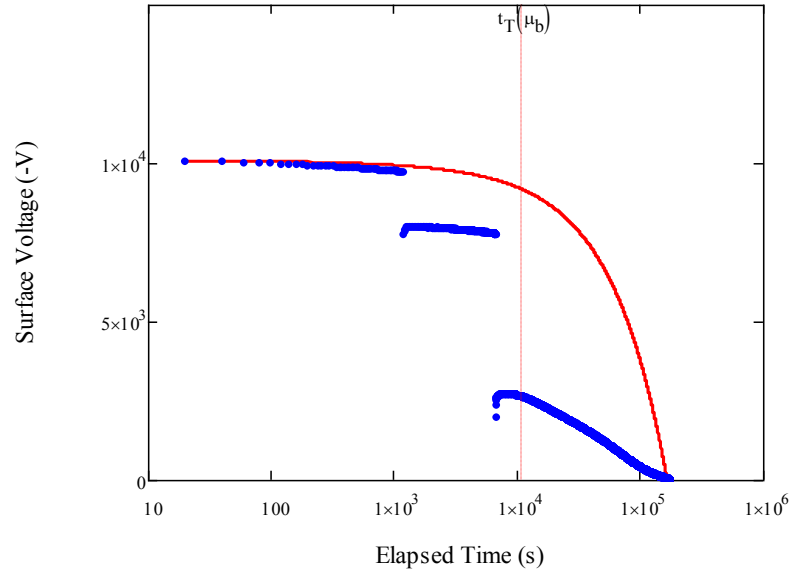


Figure 61 Discharge profile of TMM3 once illumination is removed.

The TMM3 glowed blue during irradiation which is a common occurrence in dielectrics with aromatic rings in their molecular composition and only happens once charge buildup reaches a certain exceedance level. This is not a physical breakdown, but more of a resonance response. However it does correlate with magnitude and from Figure 60 we see that the TMM3 quickly charges to above 10kV. The technicians actually ended the test due to visible arcing in the material and an upset that it caused to the sample motor switching its polarity. Upon discharge the sample continued to arc, releasing a surface plasma that disrupted the measurements for other materials. When this discharge occurs, it releases a substantial amount of stored charge as well makes it impossible to determine the RIC of the material, in that setup.

The 5880, on the other hand performed as a more standard space rated dielectric. It too appeared to have a light blue hue during exposure but not as bright. The measured standing voltage was recorded as seen below in Figure 62.

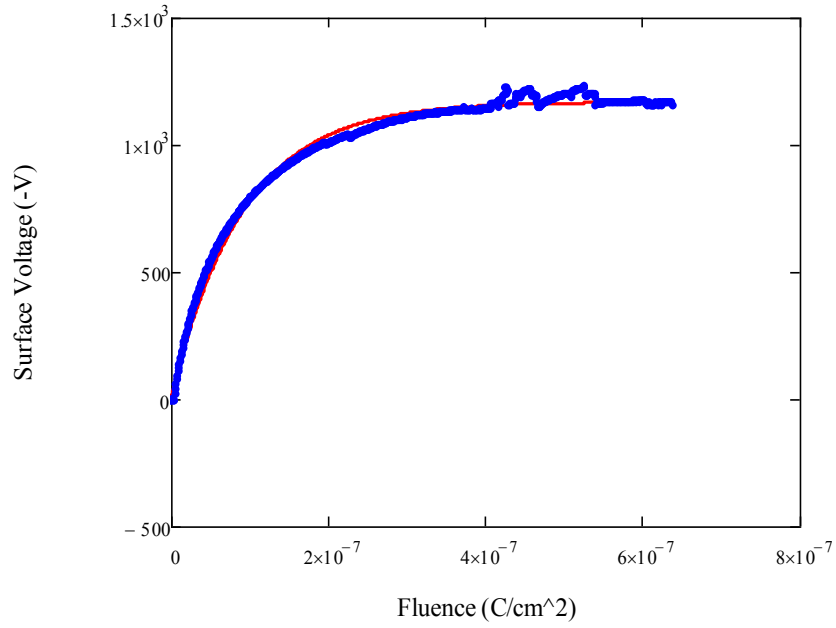


Figure 62 Standing charge on 5880 with increased charged particle exposure.

An interesting observation is made once the material reaches its equilibrium state of $\sim 1200\text{V}$ where the arcing from the TMM3 shows the plasma wave influencing standing voltage on the 5880. Once the illumination is removed, the sample also provides a more reasonable discharge profile where the rate of discharge can be plotted to determine the dark conductivity. The slope of the discharge, from Figure 63, is used along with the permittivity of the material to extract the dark conductivity as follows

$$g_{dark} = \frac{T_{decay}}{\epsilon_0 \epsilon_r} = 6.855 \text{ E16 } \Omega \cdot \text{cm} \quad 36$$

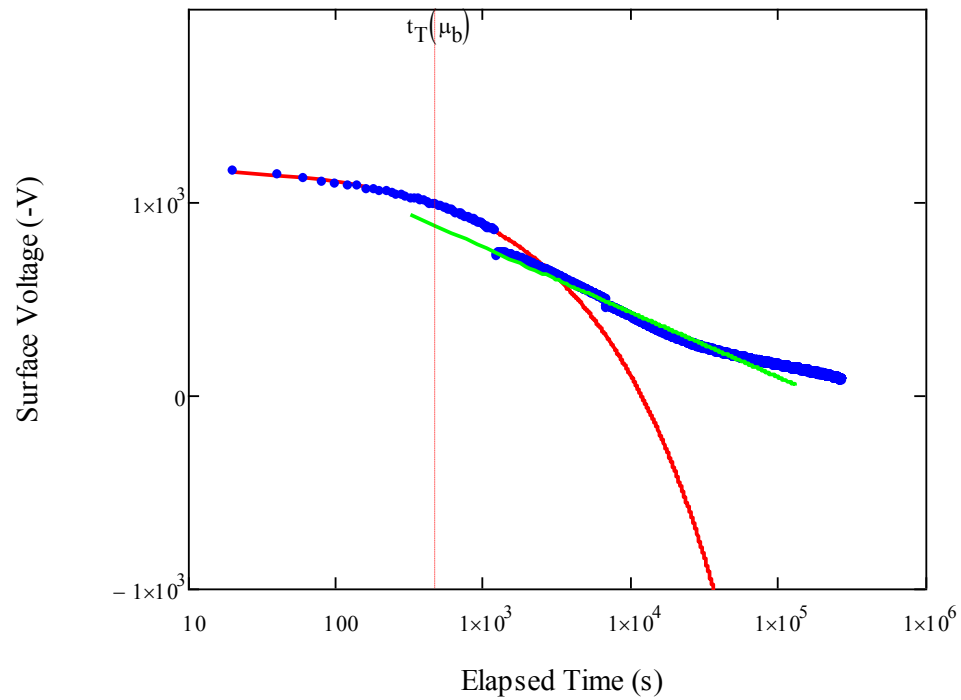


Figure 63 Discharge profile of 5880 once illumination is removed.

From this point, a 35 GHz LC reflectarray element is constructed with the Duroid 5880 dielectric, GT3-23002 LC, and copper ground plane / patch. The layup and measurements are illustrated in the following figure. This is the same element that went through Cobalt-60 and X-ray testing discussed in the previous section.

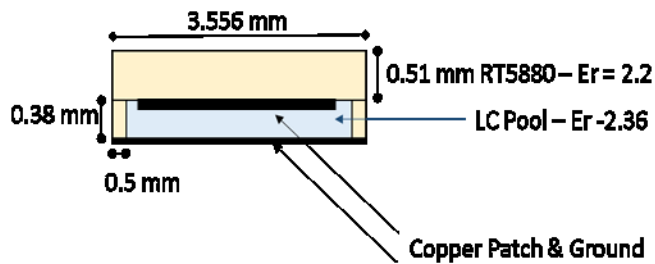


Figure 64 Layup of LC RF element used for charging tests.

The 5880 surface dielectric will become charged external environmental sources like the solar wind plasma. For typical solar wind plasmas significant dielectric surface voltages

develop because of the small volume resistivity. The results from the previous charging test were fed to the developed Matlab code and the boundary conditions were setup to replicate the above figure. The resulting setup is seen below.

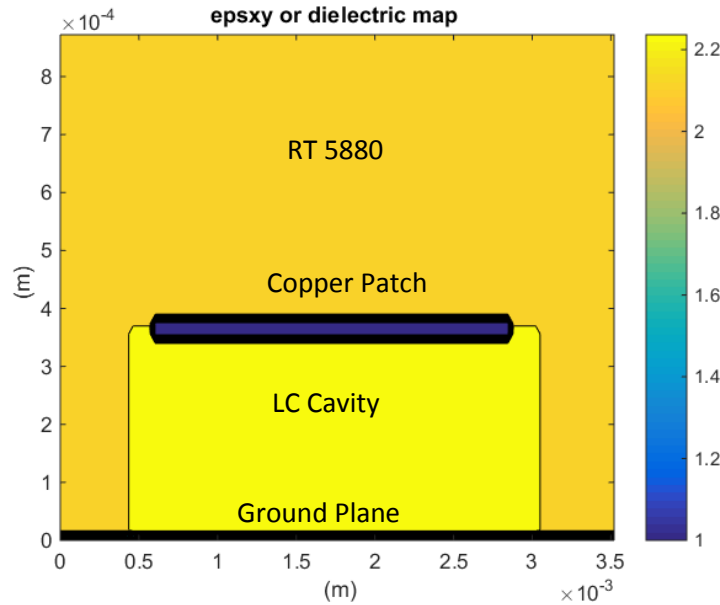


Figure 65 Layout of LC RF element used for charging tests.

From previous simulations we saw the effect of a temporary source, but in actuality, a real material will reach some steady state of charge where the bulk of the charge exist at the deposition point and represents a delta. To simplify modeling, the code is setup to represent that maximum delta that occurs during irradiation and migration is ignored as a representative system would be exposed to long duration exposure. The final model setup is shown below.

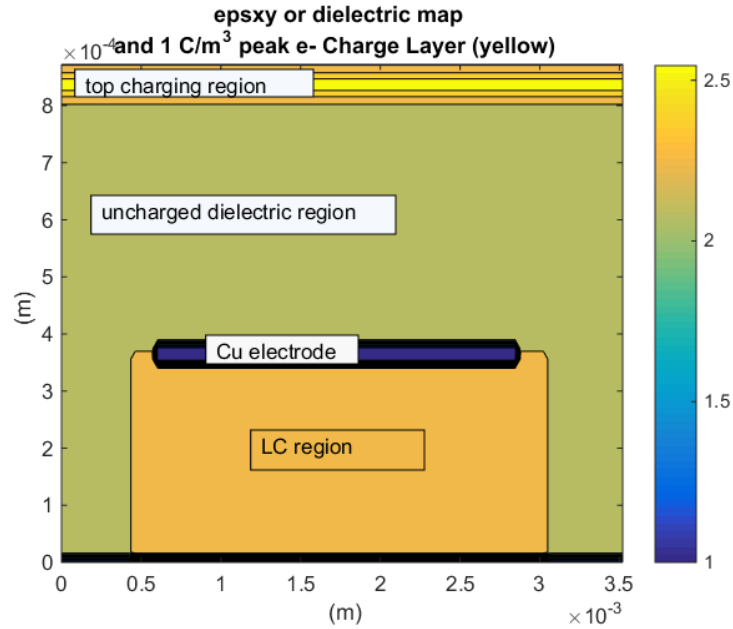


Figure 66 Layup of LC RF element used for charging tests.

The figure below shows a calculated 2D field or center-line distribution which would reproduce the voltages observed in typical tests with the LC sample that utilizes a 30V max biasing. LC distortion from charging will be largest at the copper patch edges and the outer LC region will be impacted. The nominal operating field in the LC regions is about 80 kV/m. A more difficult calculation is to determine the impact on the RF array gain based on LC distortions as the resulting permittivity in that LC region is no longer uniformly controlled by the biasing electrodes alone. In all likelihood, this can only be solved by accurately capturing the time dependent nature of charge migration through the LC and neighboring dielectric and the resulting magnetic and electric fields present.

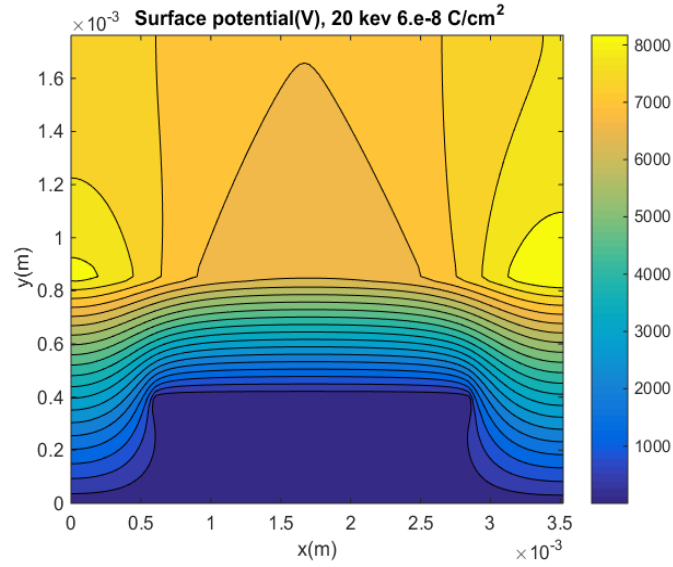


Figure 67 Surface potential expected on LC element under charge exposure.

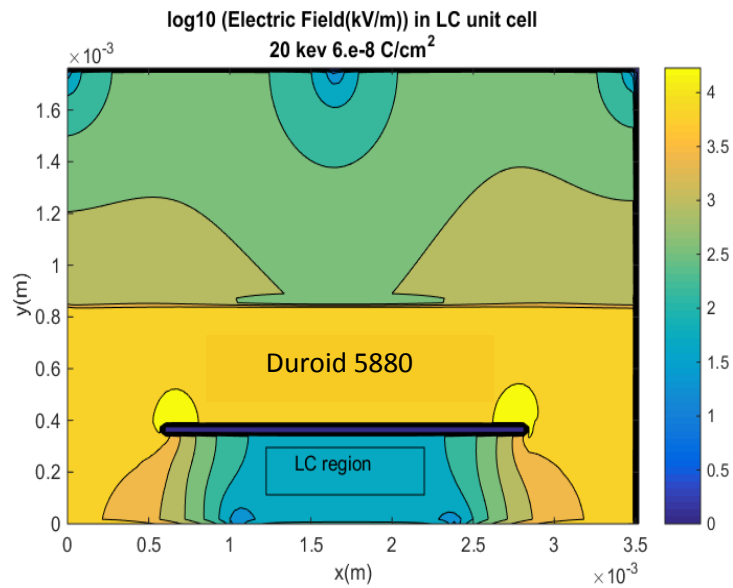


Figure 68 Standing normal electric fields under LC charging exposure.

The results of the model indicate there will be some profile of standing electric fields under the radiator of the LC unit which, depending on actual magnitude, will affect biasing control and will lead to challenges with element tuning to steer an array. The author wanted to setup a similar in-situ test to measure the loss reflection and measure

charge that was done in the JUMBO chamber before, but the setup is not currently appropriate for in-situ complex configurations. Cabling would need to be able to accommodate the mechanical shifting from the sample wheel and have sufficient shielding to prevent noise in the line. Additionally that test environment requires a vacuum to operate the charge sources and detectors.

For this reason, the researcher went back to the strontium source. This source is more difficult to model due to the broad spectrum source but with the energies present should be able to deposit charge throughout the dielectric thickness to establish a standing charge voltage. The setup is shown below, where aluminum scraps were used to block radiation influence on cables and a Plexiglas shroud was used to help minimize electrons. Not shown are a couple steel plates placed outside the chamber to block technicians from the backscattered gamma resulting from the influence on the aluminum blocks.

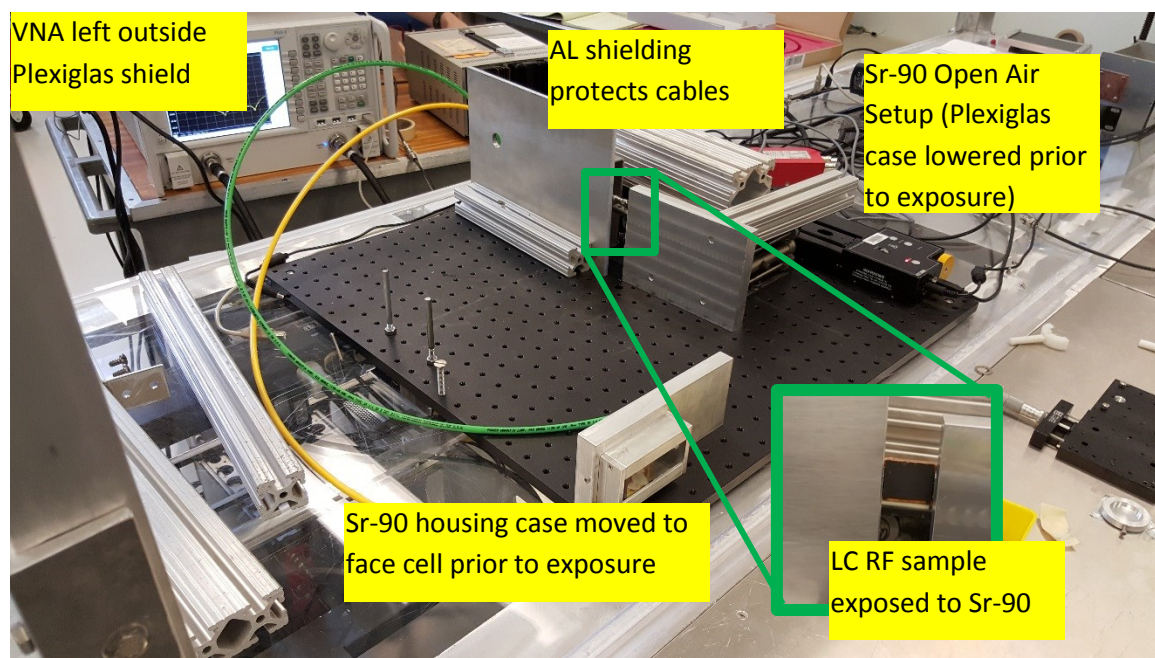


Figure 69 Standing normal electric fields under LC charging exposure.

This setup placed the sample 12 inches from the source. In order to understand how much exposure is occurring, the ESTAR database (<http://physics.nist.gov/PhysRefData/Star/Text/ESTAR.html>) is used to find the penetration across a broad energy spectrum. This can be used to see how much of the Sr-90 source is depositing in the material. This data can be combined with the exposure spectrum to highlight the cutoff energy showing the relevant deposition magnitudes in the following 2 graphs.

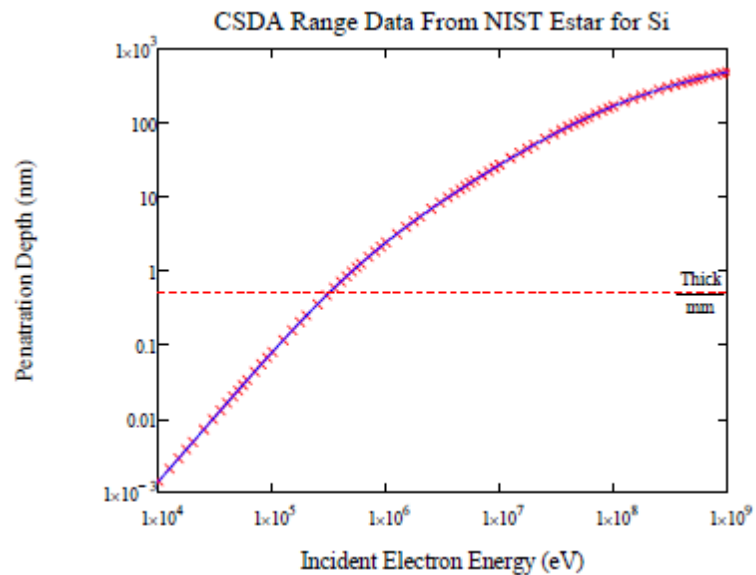


Figure 70 Penetration depth of electrons in Duroid showing at what energy level the electrons become fully penetrating.

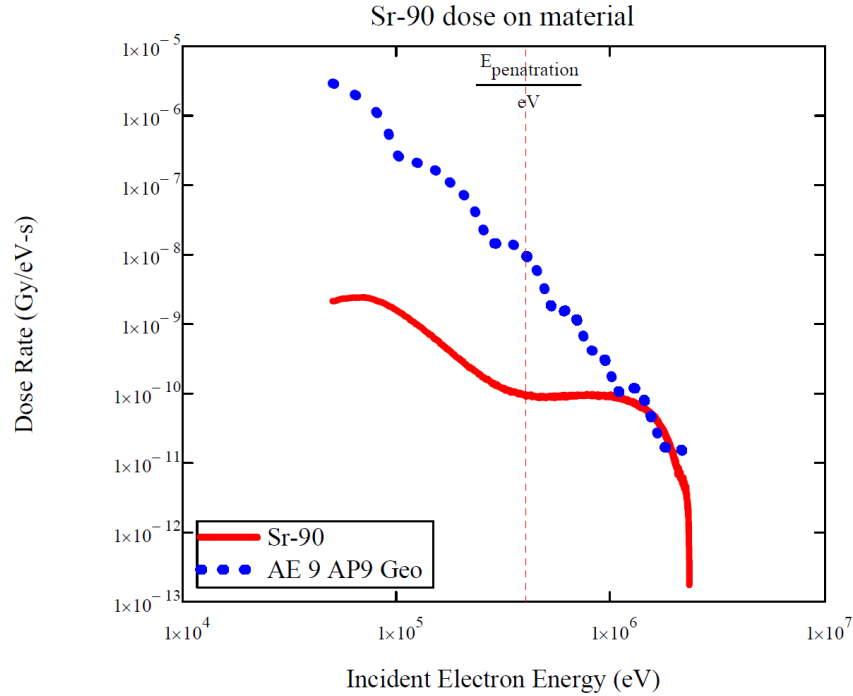


Figure 71 Sr-90 exposure spectrum compared to common GEO dose rates.

This indicates that incident electrons less than 500 keV will stop in the LC element and release their charge making it reasonable to expect some form of effect on readings. The LC element was connected to a VNA and biased through a DC choke using a DC power supply from 0 to 30V without the Sr-90 present and again with the Sr-90 illuminating the sample.

During testing, it was unclear if any effect was present. The sample shifted resonance from 33.5 GHz to 30.5 GHz when powered from 0 to 30 V. 30V over the thickness of the LC substrate corresponds to about 80kV/m of biasing control. The sample was allowed to relax unpowered prior to radiation. Once the sample was illuminated, no shift was seen. This was left alone for 15 minutes with no change. This would indicate that any deposited charge was not providing sufficient standing potential

to exceed the Fréedericksz transition. The sample was powered to 18V and 30V to observe any effect which at the time were unclear. Upon returning to 0V, it seemed that the sample transitioned back to its original resting state. However, once measurements were plotted together, the real influence was observed. The next two plots show the overlay of return loss measurements for the unit cell when it is biased with and without the Sr-90 source and when it initiates and returns to a rested position. It is clear from Figure 72, that no significant shift in response is seen with the exposure of strontium depositing electrons onto the structure. In Figure 73, however, a different observation is seen. While the unbiased cell seems to be slightly influenced by the presence of Sr-90, it is more surprising that once the cell is cycled, it is unable to return to its unbiased state.

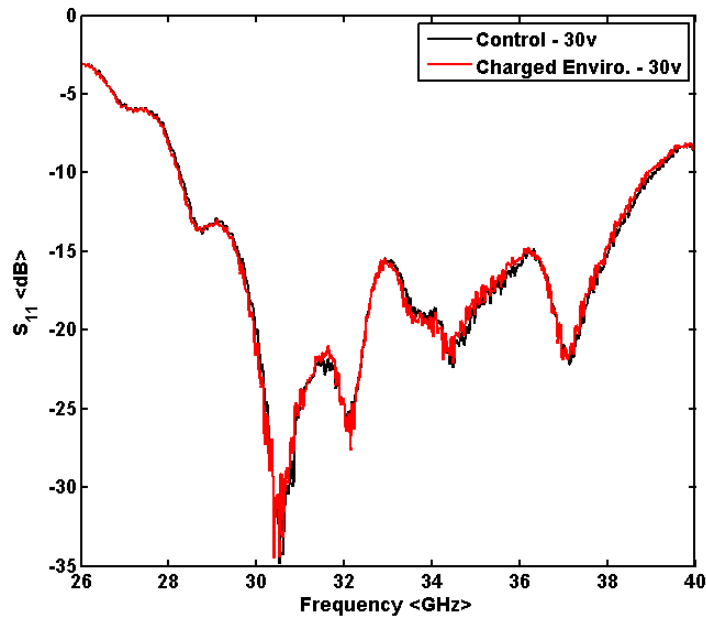


Figure 72 Return loss for LC unit cell when fully biased with/without the Sr-90 source present.

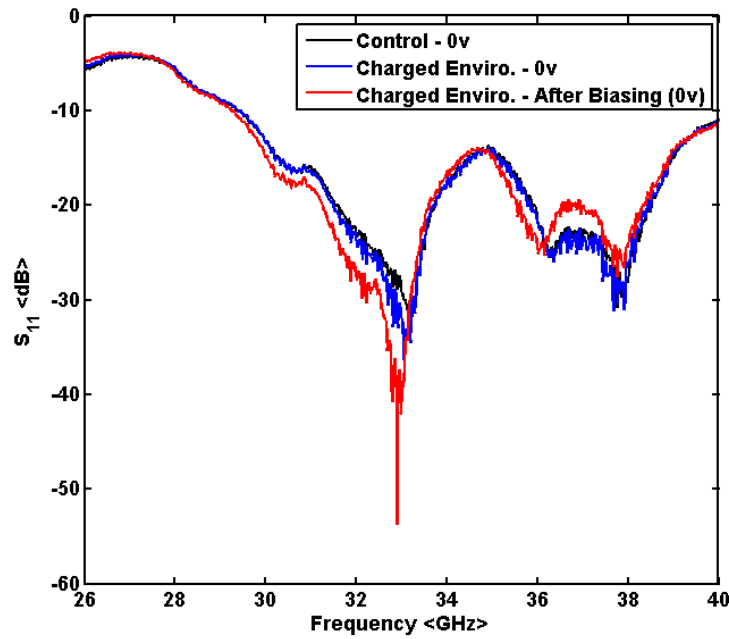


Figure 73 Return loss for LC unit cell when fully relaxed prior to and after biasing with/without the Sr-90 source present.

This has significant impact for applications that want to use LC in a space environment. This measurement demonstrates the impact of the stray E-fields shown in the modeling results of Figure 68 where the effect of charge deposition can allow biasing fields to creep into LC regions. Had this sample utilized a fully open reservoir such as that seen by the current state of the art researchers [43,48], where there are large regions of LC encapsulated only by dielectric material, then we could expect a greater influence from the surface charge. While the peaks may seem close, it is important to remember with these elements that it is the phase that is important as steering is dictated by the phase delay between elements and if that phase cannot be controlled then the resulting culminated beam will be poorly tuned and have significant noise and degradation. The phase was extracted from the VNA measurements and compared for the sample when exposed and when left uncharged. The below figure shows that there is little effect on the 30V charge due to that already being the upper limit of tuning for the LC. Interestingly we see

that the presence of charge helps push the LC when set at 18V to a biasing phase shift more in line with a higher biasing voltage around 20V-22V. Additionally, the inability for phase to return to 0 degrees after irradiation will reduce the overall range of delay possible and consequently will limit the beam steering limits as well. The severity can be further distinguished by concentrating on the percentage difference between both radiation states in Figure 74.

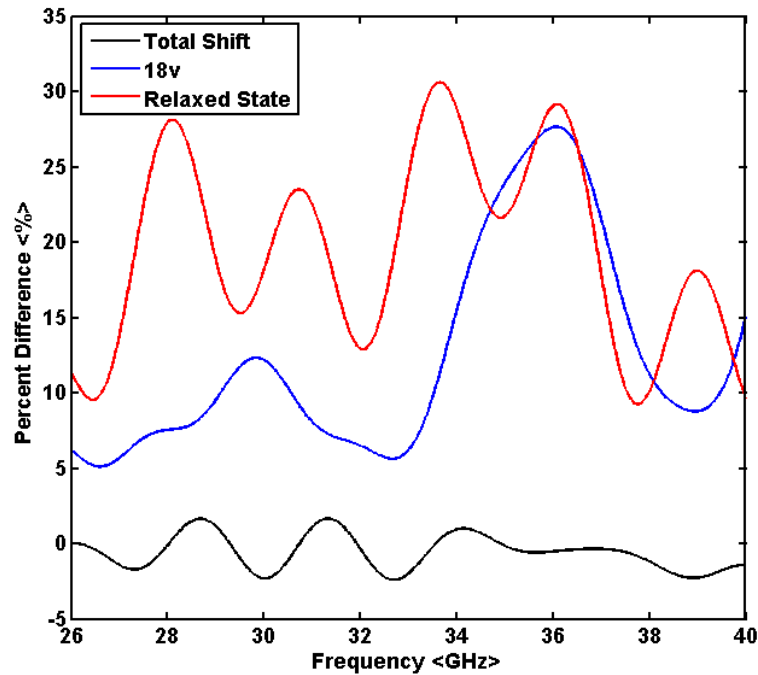


Figure 74 Percentage of difference between radiated and non-radiated voltage states.

Now that the problem has been identified, the author presents the following as ways to minimize or mitigate this problem in future designs. These steps were taken by a fellow student, Christopher Woerhle, in his research focusing on the manufacturing of LC arrays to meet space challenges. The first step would be to consider a surface treatment for the array to mitigate the deposition of charge and to provide a thin conductive surface layer to bleed off static charge and reduce the overall total potential. This process has been tested and described in the literature [84] as effective for charge management of traditional antenna types but can diminish original antenna

performance properties by increasing insertion loss and requires additional consideration for the resulting effect on the input standing wave ratio is designed for. Charging was reduced, not mitigated, by introducing an electrostatic protection layer of Kapton with a tin oxide (TO) film. Another way to reduce the effect is to raise the Fréedericksz transition. LC can be mixed into a variety of polymer networks to add structure to the LC in an unbiased state. While the result of this approach requires higher voltages, which may then create dielectric breakdown risks, it can result in a stronger anchor force to return LC order to its unbiased state. It is suspected that the gradual tuning of the LC's dielectric range at between its perpendicular and parallel states would still be influenced, but by a smaller percentage certainly less than the 30% seen before. The last way proposed is to essentially bury the LC behind conductive elements and reduce the unnecessary cavity size. This has added benefit by increasing the structural robustness of the array but will increase the manufacturing greatly and therefore, drive up costs.

The author worked with the previously mentioned student to incorporate these lessons learned into his design. The resulting array is his work to present, but a model of the setup was created to check out the influence of charge on a new LC array incorporating the charging lessons-learned.

The following figure shows the element that utilizes an LC feed line to provide delay and the coupling provided by a reflector patch above a slotted ground plane. The LC is biased by a conductor under that slotted ground plane and is protected on the backside from an additional grounded shell. The reflector patch is spaced above the ground plane with vacuum gap to prevent static charge distributed on the top surface from migrating to the LC.

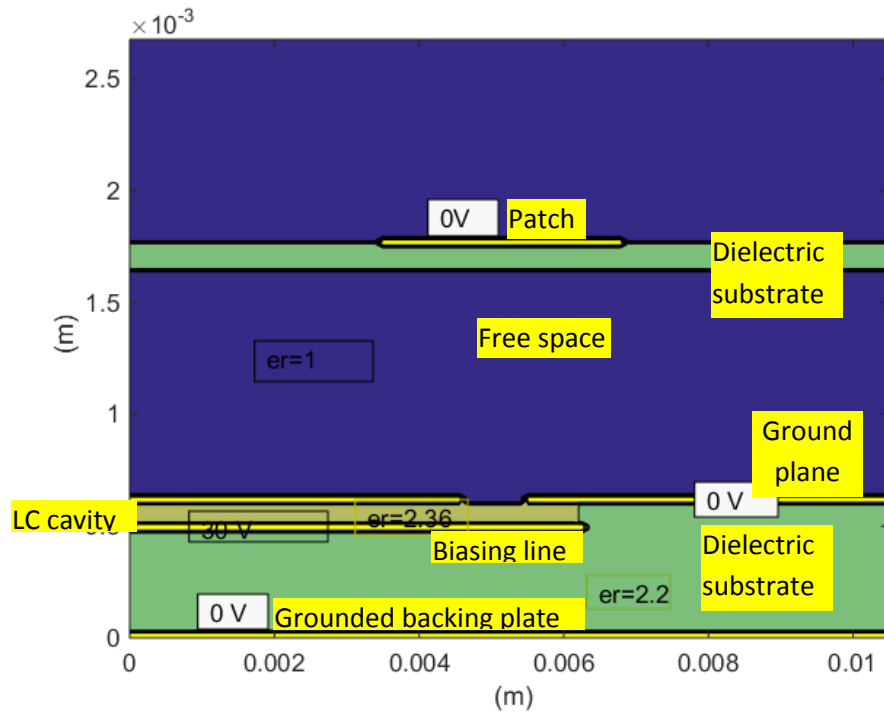


Figure 75 LC feed line slot array with patch radiator setup

The conductor was modeled with a 30V potential to demonstrate the resulting E-fields generated and potential within the setup. The next two graphs show the standing voltages and field strengths present in the complex arrangement without the presence of an incident radiation source depositing charge.

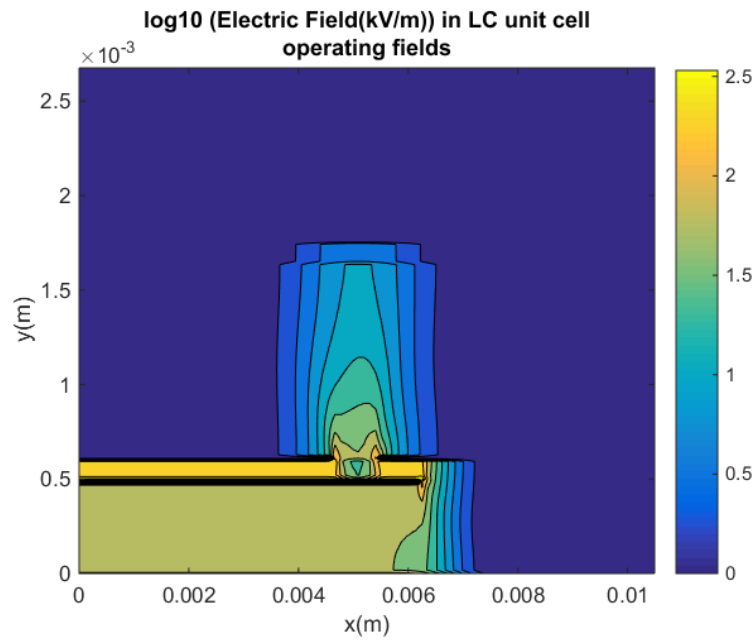


Figure 76 Electric Fields generated by 30V biasing charge on LC feed line.

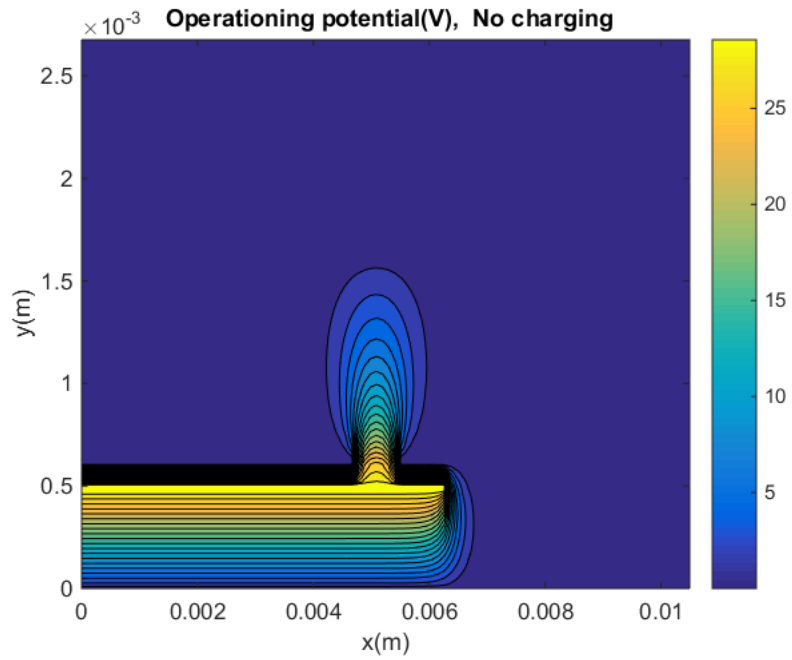


Figure 77 Corresponding voltage potential in LC cell.

Once the sample is radiated with the same source used in Figure 66, the same plots are calculated to check for influence to the LC under is fully biased state and then again when the biasing conductor is set to 0V.

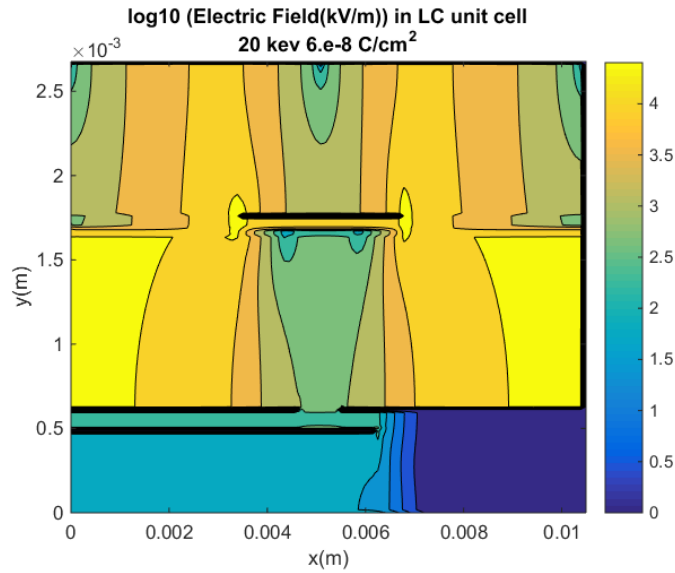


Figure 78 Electric Fields generated by 30V biasing charge on LC feed line in the presence of a low energy charge deposition.

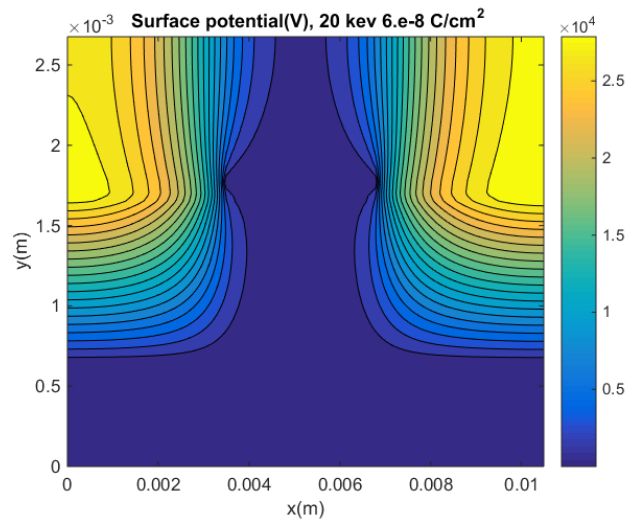


Figure 79 Corresponding voltage potential in LC cell in the presence of a low energy charge deposition.

While large potentials are seen on the top most layer exceeding 2kV, this does not seem to feed through to the LC cavity. Further, it is seen that electric potential within the cavity is unchanged. This is a consistent result with what was seen in a more standard reflectarray configuration. Next, the unbiased scenario is shown.

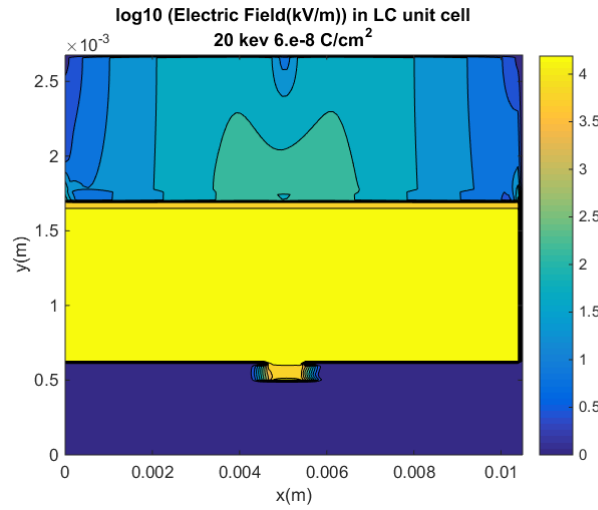


Figure 80 Electric Fields generated by 0V biasing charge on LC feed line in the presence of a low energy charge deposition.

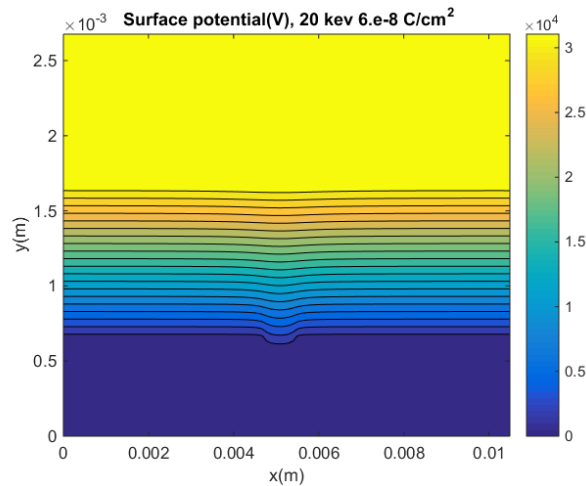


Figure 81 Corresponding voltage potential in LC cell in the presence of a low energy charge deposition.

As can be expected, the charging of the top layer creates a capacitor resulting in a potential between the top layer and slotted ground plane. The open slot (not protected by a conductor naturally flows down to the next available conductor, which is the biasing conductor. This means that a portion of that feed line will be exposed to a biasing field due to the presence of charge deposition, but it does not appear to be quite as extensive as the profile shown in Figure 68. If further protection is needed, the design may require an isotropic slug to fill the feed line at the point of the slot.

CHAPTER 7: CONCLUSIONS AND FUTURE WORK

7.1 Summary of work completed

This research effort focused on the assessment of claims made about LC being a viable candidate material for reconfigurable RF apertures. At the time this research started there were several examples of LC implementations in RF apertures and reflectarrays for terrestrial bench-top demonstrators, but no indications of fielded hardware. This effort then started verifying claims made about the utility by focusing on the material itself when exposed to simulated space environments and manufacturing.

From a fundamental perspective, LCs are a great candidate for reconfigurable apertures. Although the assembly process is challenging in a lab environment, the hardware/equipment list is insignificant compared to other PIN/ VARACTOR/ FET/ MEMS approaches. Additive manufacturing approaches are likely not yet suitable for production of the substrate if complex cavities and fluid fill channels are to be implemented due to the production variability and poor bond strength between printed interfaces during radiation and vacuum exposure. This will change as printing technology trends more toward RF materials and away from cheap fit check plastics

LC thermal limits are less than many common electrical components (-60C to 125C) but manufactures seem to be developing new blends daily that are expanding that limitation. Test performed indicated a cell phase range loss of about 10-15 degrees over the operational thermal limits. Brief analysis on the dielectric and conductive substrates showed that mechanical deformations were likely not of concern within the LC operational limits. However, the trade space of the final array size, the distance from the feed horn and the transmitter power may have significant implications on the array configuration and it is not likely that a sub array will be feasible for higher power transmitters. It is more likely that the reflectarray may have to serve as the primary reflector at the higher power end of the spectrum, which will drive up cost and system complexity. This can be compromised with advanced thermal management technologies

to move the microwave induced heating. Furthermore the effect temperature has on switching speeds is seen to be a big roadblock for this approach where many communications systems may require nanosecond switching.

Vacuum is unlikely to pull LC fluids through the solid walls, but the dielectric encapsulating it will certainly shed any stored gasses. This was an additional issue for printed materials made in standard atmospheric environments where water vapor was trapped during printing and then removed in vacuum causing micro-cracking to occur in the printed strands. While coating materials exist to prevent an enclosed fluid from escaping, any material effects resembling micro-cracks will likely create a leaking path.

The LC have been tested for radiation hardness and have appeared to maintain operation. But the material breakdown is still not known. Radiation certainly degrades encapsulating dielectric materials mechanically through bond dislocation, but the electrical properties seem to maintain their original parameters. This becomes less true at frequencies above 60GHz where micro structural defects may start to propagate and influence EM interactions. While radiation damage may not have had a significant impact on performance, charging from space radiation did. Modeling was done to show that charge buildup may be an issue. Testing showed that deposited charge biased the LC materials slightly causing an increase to control voltages below the max value and an inability for the LC to return to an unbiased state once control was set to 0V.

7.2 Recommendations for future LC designs

Although some testing showed performance that are not suitable for all RF applications, there are foreseeable mitigation steps that can be taken. LC blends are continuing to mature and are now being considered by the manufacturer, Merck, for RF utilization so it is expected that improved figures of merit will continue to be released with respect to greater permittivity range and lower insertion losses.

Ceramic substrates and machining of those substrates to allow for cavity sizes is strongly recommended. Ceramics will tolerate heating and cavity size restriction to only the volume required for tuning will allow less variability in an operational environment where standing charge fluctuates and may change the RF material properties of the assembly. Additionally, consideration of arrangements that cover LC in as much conductively grounded material should reduce the influence of standing fields on the surface of an antenna substrate or deposited within. While radiation effects still need to be better understood, it is not likely a show stopper for LC operations in space.

Finally, while these steps may allow for applications related to single beam pointing system, SAR scanning apertures, or telemetry platforms, the switching speed must increase dramatically for both 'on' and 'off' states to make it a viable communication replacement for currently fielded phased arrays that utilize TDMA scheduling windows and frequency hopping. This may be achievable through polymerized networks within the LC cavity which acts like a binder to the LC directors creating a significantly larger anchoring force. This also raises the Fréedericksz transition voltage significantly which may in turn resolve the influence from deposited charges in the assembly. A basic flow of the thought process for this research and recommended course of action for future LC RF designs is provided in the following process diagram.

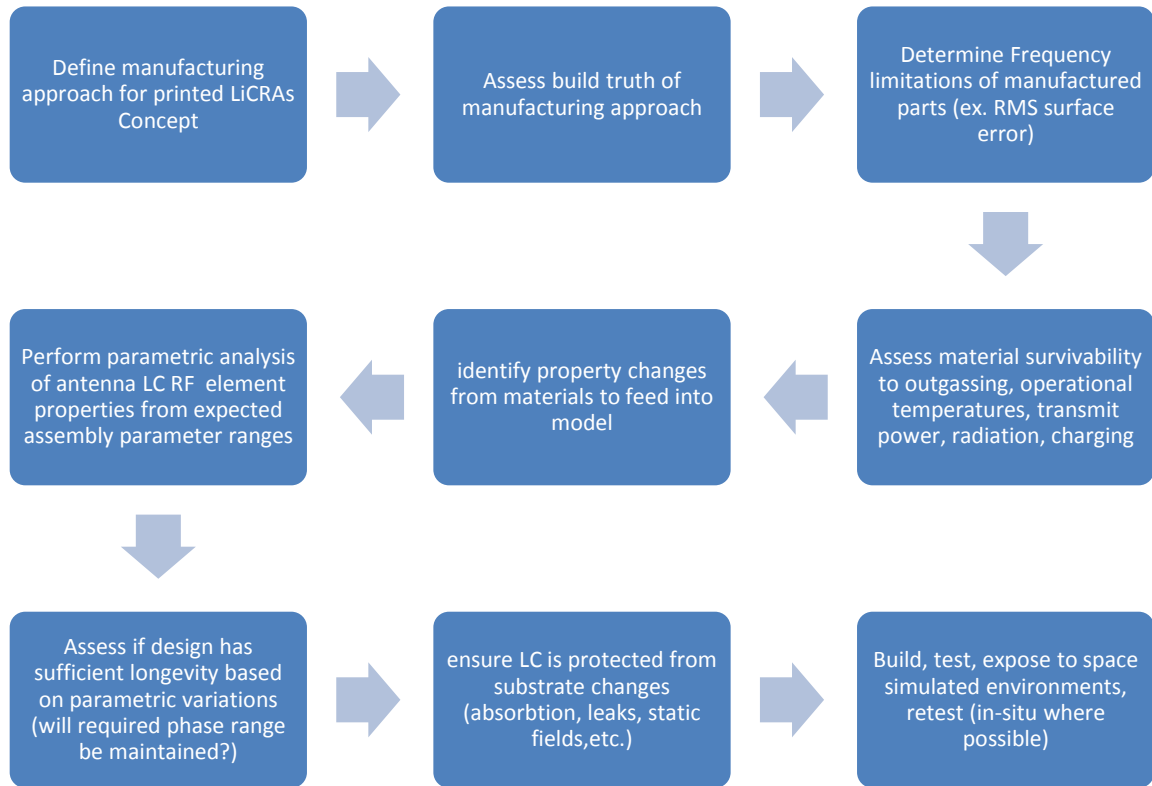


Figure 82 Recommended design process for printed LC RF elements.

7.3 Ideas for future research

Several research opportunities still exist for this field of research. The first idea that comes to mind is the topic for an LC reflectarray topic with broadband response across its tunable range that allows it to maintain a constant reflection magnitude over a range of permittivity values. The final product may have similarities MEMS type phoenix cells where the element has several resonant features that correspond to different permittivity ranges.

Another area of research could be in refining the charge migration and deposition work. The current code can be used to show charge propagation but corners and interfaces create instabilities in the code that are likely effecting results. Also the

influence of current flow is not present. The deposited energies only show one spectrum while space will have a much broader coverage. If a precise mapping can be made of the element and charge with correlation provided between the E-fields and the anisotropic permittivity of the LC, software codes like HFSS may be able to better model and capture the far-field effects.

APPENDIX A

% 2D finite element code using triangular elements (Credit to David Welles for figuring out finite element modelling of charge migration)

```
clear all;
ygrnd=1;
setup_Beam;
```

```
% Setup problem space and Beam
%
```

```
clear all;
% mks units (usually) for FEC inputs unless otherwise stated
eps0=1/(36.*pi)*1.e-9; % f/m
q=1.602e-19;
% problem space
% time points
ntmax=100;
delt=.5;% seconds
% Beam and material parameters
Einc=20; % keV to replicate available HW
Jin=10.e-9; % amp/cm^2 Beam current
Density=2.2; % g/cm^3 dielectric density
Zav=6; % average atomic number
eps_material_LC=2.5; % LC on state
eps_material=3.5; % DC dielectric constant
eps_material_metal=1e12
```

```
ygrnd=1;
```

```
% bring in RIC and charge profile
[chargeprofile, sigma,Depth_cm,str,str1,str2]=ChargeDeposition(Jin,delt,Einc,Zav,Density); % Jin
amps/cm^2, delt sec, Einc kev , Coul/cm^3
```

% calculates range in materials, units here are hazardous atomic number

```
function [chargeprofile, sigma,Depth_cm,str,str1,str2]=ChargeDeposition(Jin,delt,Einc,Zav,Density) % Jin
amps/cm^2, delt sec, Einc kev , Coul/cm^3
g(1:100)=0; % depth array
nd(1:100)=0;
stra='Z= ';
strb=num2str(Zav);
str=[stra strb];
stra='density(g/cm^2)= ';
strb=num2str(Density);
str1=[stra strb];
stra='Electron energy(kev)= ';
strb=num2str(Einc);
str2=[stra strb];
Aa(1:82)=0.;
Bb(1:82)=0.;
Cc(1:82)=0.;
Dd(1:82)=0.;
Ee(1:82)=0.;
Ff(1:82)=0.;
for nz=1:82
```

```

    Z(nz)=nz;
end
for nz=1:82
    zin=nz;
    [Aa(nz),Bb(nz),Cc(nz),Dd(nz),Ee(nz),Ff(nz)] = ABCDEFcoef(zin);

```

```

function [A,B,C,D,E,F] =ABCDEFcoef(Z)

```

```

A=2;
B=0;
if(Z>=12)
    B=(Z-12.)*(8/8) +0;
end
if(Z>=20)
    B=(Z-20.)*(15/62) + 8;
end
C=0;
if(Z>=10)
    C=(Z-10)/5*(-12);
end
if(Z>=15)
    C=(Z-15)*(-2/5) -12;
end
if(Z>=20)
    C=(Z-20)*(2/10) -14;
end
if(Z>=30 && Z<=40)
    C=(Z-30)*(12/10) - 12;
end
if(Z>=40)
    C=0;
end
D=0;
if(Z>=5)
    D=(Z-5.);
end
if(Z>=15)
    D=(Z-15)/27*(3)+ 10;
end
if(Z>=42)
    D=(Z-42)/40*(82)+ 13;
end
E=exp(-(Z-30)/15);
F=-exp(-(Z-35)/13) + 5.5;
end

```

```

end
g(1:100)=0;
for nw=1:100
    nd(nw)=(nw-1)*.05;
    w=nd(nw);
    [A,B,C,D,E,F] = ABCDEFcoef(Zav);
    g(nw)=( A+ B*w +C*w^2 +D*w^3)*exp(-(E*w^3 + F* w) );
end
% integrate gz
norm=sum(g)*.05;

```

```

g=g/norm;
% determine bulk plasmon energy
% hb= 1.05457173e-34 ; % m2 kg / s
% % density of valence electrons(m^3)'
% Nv= 4/(1.5e-9)^3 % density of valence atoms
q= 1.602176487e-19 ;
evJ=q;
%
[alpha , beta] =ABcoef(Zav);


---


function[alpha , beta] =ABcoef(Z)
% coefficient for deposition based on IEEE paper by Kim
alpha=0;
beta=0;
if(Z<=41)
    alpha=4.2 + 1.3/40*Z;
end
if(Z>=41)
    alpha=5.5+2.4/41*(Z-41);
end
beta=1.78*(exp(-Z/600)); % Energ(n)=n ; % kev
Rang=alpha*Einc^(beta)/1000; % mg/cm^2
for nw=1:100
    gnorm(nw)=g(nw)* Einc/Rang;
end
% backscatter coefficient vs energy
for n=1:1000
    Mev(n)=n*.001 ; % MEV
    Bak(n)=(.14 - .039*Mev(n))*(.1*Zav^.9) ;
end
Depth_cm=nd*Rang*(Density*1.e-3);
xval=(Depth_cm).^1;
yval= gnorm*(1-Bak(Einc)).*xval;
sumyval=sum(yval)*Depth_cm(2);
chargeprofile=yval/sumyval;
chargeprofile=Jin*chargeprofile*delt;


---


EnergD=gnorm*(1-Bak(Einc))*1.e6*Jin*(Density) ;% J/cm^3/s for 1 nA/cm^2, Amps to electrons 1./1.6e-19, Mev = 1e6, ev to J 1.6e-19
Drate=EnergD/(Density*1.e-3); % Gray Joule/kg-s, convert J/cm^3/s --> J/kg-s, density is g/cm^3
% radiation conductivity for Kapton -- French paper on Kapton
log_sigma=.8185*log(Drate)-28.387;
%
sigma=exp(log_sigma); %mho/m


---


%
Depth_m=Depth_cm*.01; % convert to meters
% Note the yp or dely for gridding is determined by beam energy and energy deposition, low energy
smaller -> dely
chargeprofile=chargeprofile*1.e6 ; % convert to Coul/m^3

% specify grid
[nc1, nchgmax]=size(chargeprofile)
nymax=nchgmax;
nxmax=50; %Probelm space width

```

```

dely=Depth_m(2)-Depth_m(1);
delx=dely;
xp(1:nxmax)=0;
yp(1:nymax)=0;
% specify 2D coordinates
for ny=1:nymax
    yp(ny)=(ny-1)*dely;
end
for nx=1:nxmax
    xp(nx)=(nx-1)*delx;
end
%2D problem space arrays
epsxy(1:nxmax,1:nymax)=1;
rhonow(1:nxmax,1:nymax)=0;
rhobeam(1:nxmax,1:nymax)=0;
% radiation induced conductivity
sigRIC(1:nxmax,1:nymax)=0.e-12;
% conductivity based on number density and mobility
sig_n(1:nxmax,1:nymax)=0;
% total conductivity
sig(1:nxmax,1:nymax)=0.e-12;
Jmap(1:nxmax,1:nymax)=0;
Jx(1:nxmax,1:nymax)=0;
Jy(1:nxmax,1:nymax)=0;
divJ(1:nxmax,1:nymax)=0;
ex(1:nxmax,1:nymax)=0;
ey(1:nxmax,1:nymax)=0;
etot(1:nxmax,1:nymax)=0;
fxy(1:nxmax,1:nymax)=0;
% number of electrons
nelect(1:ntmax)=0;
% Match profile to problem space
% add dark conductivity
for nx=1:nxmax
    for ny=1:nymax
        rhobeam(nx,ny)=chargeprofile(ny);
        sigRIC(nx,ny)=sigma(ny)+ 2.e-15 ;
    end
end
% invert deposition and conductivity profile to match grid setup
rhodum=rhobeam;
sigdum=sigRIC;
for nx=1:nxmax
    for ny=1:nymax
        rhobeam(nx,ny)=rhodum(nx,nymax-ny+1);
        sigRIC(nx,ny)=sigdum(nx,nymax-ny+1);
    end
end

% shift profile 20 *dely for vacuum at top of problem space
rhodum=rhobeam;

sigdum=sigRIC;
for nx=1:nxmax
    for ny=20:nymax

```

```

        rhobeam(nx,ny-19)=rhodum(nx,ny);
        sigRIC(nx,ny-19)=sigdum(nx,ny);
    end
end
% vacuum space
for nx=1:nxmax
    for ny=nymax-18:nymax
        rhobeam(nx,ny)=0.e-4;
        sigRIC(nx,ny)=0;
    end
end
% Make a 2D Gaussian spot -- just add a simple envelope at center of problem space
for nx=1:nxmax

    taper=exp(-(nx-nxmax/2-.5)^2/36);
    rhobeam(nx,:)= rhobeam(nx,:)*taper;
    sigRIC(nx,:)=sigRIC(nx,:)*taper;
end
% 2D contour plots
% -----FEC setup-----
% number of finite element triangular elements for FEC code
nemax=(nxmax-1)*(nymax-1)*2;
% triangle points, 3 for each triangle
x(1:nemax,1:3)=0;
y(1:nemax,1:3)=0;
%number of nodes
nn=nxmax*nymax;
k(1:nn,1:nn)=0;
b(1:nn)=0;
bel(1:3)=0;
ke(1:3,1:3)=0;
phi(1:nn)=0;
% element arrays
f(1:nemax)=0;
eps(1:nemax)=1 ;
rho(1:nemax)=0;
f(1:nemax)=0;
n(3,1:nemax)=0;
ne=0;
% FEC node maps
for ny=1:nymax-1
    nstart=(ny-1)*nxmax + 1;
    nstop= ny*nxmax-1 ;
    for numx=nstart:nstop
        ne=ne+1;
        n(1,ne)=numx;
        n(2,ne)=numx +1;
        n(3,ne)=numx+ nxmax;
        ne=ne+1;
        n(1,ne)=numx+1;
        n(2,ne)=numx +nxmax+1;
        n(3,ne)=numx+ nxmax;
    end
end
    ne=0;
for ny=1:nymax-1

```

```

for nx=1:nxmax-1
ne=ne+1;
    x(ne,1)=(nx-1)*delx;
    x(ne,2)=nx*delx;
    x(ne,3)=(nx-1)*delx;
    y(ne,1)=(ny-1)*dely;
    y(ne,2)=(ny-1)*dely;
    y(ne,3)=(ny)*dely;
ne=ne+1;
%   upper triangle
    x(ne,1)=(nx)*delx ;
    x(ne,2)=(nx)*delx;
    x(ne,3)=(nx-1)*delx;
    y(ne,1)=(ny-1)*dely;
    y(ne,2)=(ny)*dely;
    y(ne,3)=(ny)*dely;
end
end
ne=0;
% Specify Dielectric, sigma and convert to node map
for ny=1:nymax
    for nx=1:nxmax
        if (ny>1 && ny<= 35) && (nx >= 15 && nx <= 35))
            epsxy(nx,ny)=eps_material_LC;
        else
            epsxy(nx,ny)=eps_material;
        end
    end
    % relative dielectric constant
    if(ny>= nymax-19)
        epsxy(nx,ny)= 1;
    end
end
end
% Map the 2D epsxy array onto the nodal elements
[XX,YY] = meshgrid(xp,yp);
figure(1) %
subplot(121)
[XX,YY] = meshgrid(xp,yp);
hold on
contourf(XX,YY,epsxy',10)
hold off
colorbar
title({'Dielectric Profile'})
xlabel('x(m)');
ylabel('depth(m) ');
subplot(122)
hold on
contourf(XX,YY,(sigRIC)',25);
colorbar
hold off
title({' Radiation Induced','Conductivity (mho/m) '})
xlabel('x(microns)');
ylabel('depth(microns) ');
% initial charge density array
rho_start=rho_beam;
column_rho(1:nxmax)=0.;

```



```

    for nx=1:nxmax
        column_rho(nx)=sum(rhostart(nx,:))*dely;
    end
ne=0;
% load node maps
for ny=1:nymax-1
    for nx=1:nxmax-1
        ne=ne+1 ;
        eps(ne)=epsxy(nx,ny);
        rho(ne)=rhostart(nx,ny);
        ne=ne+1;
        eps(ne)=epsxy(nx,ny);
        rho(ne)=rhostart(nx,ny);
    end
end

% specify gound plane
% when ney < ygrnd charge will not appear
Boundary_Ks;

np=0;
nl=0;
% specify potential on FEC boundary nodes for potential
% Specify ground plane
for ny=1:nymax
    for nx=1:nxmax
        np=np+1;

        if( (ny==1 || ny== 1) && (nx >= 1 && nx <= nxmax))
            nl=nl+1;
            nd(nl)=np;
            p(nl)=-1.e10; % ground plane potential(V)
        end
        if( (ny>=0 && ny<= 1e-4) && (nx >= 0 && nx <= 3.5e-3))
            nl=nl+1;
            nd(nl)=np;
            p(nl)=30; % ground plane potential(V)
        end
    end
end
nlmax=nl;
be(1:3)=0;
ce(1:3)=0;
ne=0;
for ne=1:nemax
    be(1)= y(ne,2)-y(ne,3);
    be(2)= y(ne,3)-y(ne,1);
    be(3)= y(ne,1)-y(ne,2);
    ce(1)= x(ne,3)-x(ne,2);
    ce(2)= x(ne,1)-x(ne,3);
    ce(3)= x(ne,2)-x(ne,1);
    deltae=.5*(be(1)*ce(2)- be(2)*ce(1));
    % generate elemental matrix
    for i=1:3
        for j=1:3
            del_ij=0;

```

```

        if(i==j)
            del_ij=1;
        end
        alpha=eps(ne);
        ke(i,j)=(alpha*be(i)*be(j) + alpha*ce(i)*ce(j))/(4.0*deltae);
    end
end
% add ke to k
for i=1:3
    for j=1:3
        k(n(i,ne),n(j,ne))=k(n(i,ne),n(j,ne)) + ke(i,j);
    end
end
end



---


% Start time loop, charge density and conductivity (sig) arrays are updated
tm=0;
sig=0;
time(1:ntmax)=0;
% number of time step before Beam turns off
% Set noff=0 , electrostatic problem, no charge added
noff=1;
% time steps to spew plots, pause after plots
nmap=5;
% time history for Efield at center of ground plane
ey_base(1:ntmax)=0;
for nt=1:ntmax
    tm=tm+ delt;
    time(nt)=tm;
    ne=0;
    % -----update beam and conductivity
    % beam on
    if(nt<=noff)
        rhonow=rhobeam+ rhonow;
        %sig_n is 2D array conductivity based on density of electrons and make believe mobility
        sig_n=rhonow*1.e-6*1.e-3 *.001 ; % mobility cm^2/V/s--> m^2 V/s
        % dark conductivity is 2.e-15 mho/m
        sig=sigRIC+ sig_n;
    end
    % beam off
    if(nt>noff)
        sig_n=rhonow*1.e-6*1.e-3*.001 ; % mobility cm^2/V/s--> m^2 V/s
        sig=sig_n;
    end
    % load rho charge density into FEC triangular finite elements

    for ny=1:nymax-1
        for nx=1:nxmax-1
            % lower triangle
            ne=ne+1 ;
            rho(ne)=rhonow(nx,ny);
            eps(ne)=epsxy(nx,ny);
            % upper triangle
            ne=ne+1;
        end
    end
end

```

```

        rho(ne)=rhonow(nx,ny);
        eps(ne)=epsxy(nx,ny);
    end
end
% Poisson charge density driver array
% rezero FEC driver arrays each time step and reload
b(1:nn)=0;
k(1:nn,1:nn)=0;
Boundary_Ks;
for ne=1:nemax
    bel(1:3)=0;
    % Poission driver, note eps(ne)
    for i=1:3
        bel(i)=-deltae* rho(ne)/3 *2/eps(ne)* 1/eps0/delx/dely ;
    end
    for i=1:3
        b(n(i,ne))=b(n(i,ne)) +deltae* bel(i);
    end
end
% % impose Dirichlet boundary nodes
for i=1:nlmax
    b(nd(i))=p(i);
    k(nd(i),nd(i))=p(i);
    for j=1:nn
        if(j ~= nd(i))
            b(j)=b(j)-k(j,nd(i))*p(i);
            k(nd(i),j)=0;
            k(j,nd(i))=0;
        end
    end
end
end
% Solve FEC matrix , k is nodal matrix , b' is driver array
phi=k\b';
% convert potential nodes into 2D map nodes
%
np=0;
% PhiMap(1:nxmax,1:nymax)=0;
% Emap(1:nxmax,1:nymax)=0;
for ney=1:nymax
    for nex=1:nxmax
        np=np+1;
        aaa=phi(np);
        TF = isnan(aaa);
        if(TF==1)
            phi(np)=0;
        end

        PhiMap(nex,ney)=(phi(np));
    for nl=1:nlmax
        if(np==nd(nl))
            PhiMap(nex,ney)=b(nd(nl));
        end
    end
end
end
end
% Work in 2D array space-----

```

```

% find electric field and compute current density
%sig(1:nxmax,1:nymax)=0.e-8;
for ney=1:nymax-1
    for nex=1:nxmax-1
        ey(nex,ney)=-(PhiMap(nex, ney+1)- PhiMap(nex,ney))/dely;
        ex(nex,ney)=-(PhiMap(nex+1, ney)- PhiMap(nex,ney))/delx;
        Jx(nex,ney)=sig(nex,ney)* ex(nex,ney);
        Jy(nex,ney)=sig(nex,ney)* ey(nex,ney);
    end
end
% before charge advance
nelect(nt) =sum(sum(rhonow))*delx*dely/q ;
nbefore= nelect(nt);
% FORWARD
for ney=1:nymax-1
    for nex=1:nxmax-1
        divJ(nex,ney)=(Jx(nex+1,ney)-Jx(nex,ney))/delx+(Jy(nex,ney+1)-Jy(nex,ney))/dely ;
    end
end
% GOING to AVERAGE divJ
for ney=ygrnd:nymax
    for nex=1:nxmax
        rhonow(nex,ney)=rhonow(nex,ney)+divJ(nex,ney)*delt ;
        if(rhonow(nex,ney) <= 0)
            rhonow(nex,ney)=0;
        end
        rhonow(nxmax,ney)=rhonow(nxmax-1,ney);
% % doesn't impact
        if(ney<=ygrnd)
            rhonow(nex,ney) =0;
        end
    end
end
% BACKWARD
for ney=2:nymax
    for nex=2:nxmax
        divJ(nex,ney)=(Jx(nex,ney)-Jx(nex-1,ney))/delx + (Jy(nex,ney)-Jy(nex,ney-1))/dely ;
    end
end
% AVERAGE
for ney=ygrnd:nymax
    for nex=1:nxmax
        rhonow(nex,ney)=rhonow(nex,ney) + divJ(nex,ney)/2*delt ;
        if(rhonow(nex,ney) <= 0)
            rhonow(nex,ney)=0;
        end
        rhonow(1,ney)=rhonow(2,ney);
        rhonow(nxmax,ney)=rhonow(nxmax-1,ney);
% doesn't impact
    end
end
for nex=1:nxmax
    rhonow(nex,39)= rhonow(nex,40)/2;
    rhonow(nex,40)= (rhonow(nex,39) +rhonow(nex,41))/2.;
end
% Graph results

```

```

    nxmid=floor(nxmax/2);
    ey_base(nt)=ey(nxmid,60+1);
    'nt'
    nt
    % store sample field point
    if(floor(nt/nmap)*nmap==nt)
        Mapping


---


figure(3)
subplot(211)
[XX,YY] = meshgrid(xp,yp);
contourf(XX,YY,(rhonow)',10);
colorbar
s2=num2str(time(nt));
s1='rho (C/m^3) at t=' ;
s=[s1 s2];
title(s)
xlabel('x(m)');
ylabel('depth(m) ');
figure(4)
    % max(max(PhiMap))
    hold on
    contourf(XX,YY,PhiMap',20);
    colorbar
    scale=5;
    quiver(xp,yp,ex',ey',scale,'r')
    title(' potential(V) and Field Vectors')
    xlabel('x(m)');
    ylabel('y(m)');


---


    pause
    end

```

REFERENCES

1. Imbriale, W.A., Gao, S., Boccia, L., *Space Antenna Handbook*, John Wiley & Sons, West Sussex, UK, 2012.
2. Tan, C.G., Song, F., Choke, T.Y., Kong, M., Song, D., Yong, C., Shu, W., You, Z.H., Lin, Y., Shanaa, O., “A Universal GNSS (GPS/Galileo/Glonass/Beidou) SoC with a 0.25 mm² Radio in 40nm CMOS,” Proc. of the International Solid-State Circuits Conference, session 19.4, 2013.
3. Wertz, J., Larson, W., *Space Mission Analysis and Design, Third Ed.*, Microcosm Press, Hawthorne, CA, 2007.
4. SpaceX, Falcon 9 Launch Vehicle Payload User’s Guide, Rev. 1, 2009, downloaded from <http://www.spaceflightnow.com/falcon9/001/f9guide.pdf>
5. Paquin, R., “Mechanical and thermal properties of optical and structural materials,” SC219 Short Course, SPIE International Symposium on Optical Science and Technology, 2000.
6. Harnisch, B., Kunkel, B., Deyerler, M., Bauereisen, S. and Papenburg, U., “Ultra-lightweight C/SiC mirrors and structures,” ESA Bulletin, 95, August, 1998.
7. Gilmore, D., *Spacecraft Thermal Control Handbook*, 2nd Ed., vol. 1, The Aerospace Press and AIAA, El Segundo, CA, 2002.
8. Kharipov, S.A., “Simulate Aging of Spacecraft External Materials on Orbit,” Proceedings of the Advanced Maui Optical and Space Surveillance Technologies Conference, 2006.
9. Chen, X., Parini, C.G., Collins, B., Yao, Y., Rehman, M.U., *Antennas for Global Navigation Satellite Systems*, John Wiley & Sons, West Sussex, UK, 2012.
10. Lui, P.L., “Passive intermodulation interference in communication systems,” Electronics & Communication Engineering Journal, Vol. 2, No.3, pp. 109–118, 1990.
11. Kudsia, C., Cameron, R. and Tang, W.-C., “Innovations in microwave filters and multiplexing networks for communications satellite systems,” IEEE Transactions on Microwave Theory and Techniques, Vol. 40, No. 6, pp. 1133–1149, 1992.
12. Simmons, A.J. and Kay, A.F., “The scalar feed – a high performance feed for large paraboloid reflectors,” Design and Construction of Large Steerable Aerials, IEEE Conference Publication, vol. 21, 1966.
13. McEwan, N.J. and Goldsmith, P.F., “Gaussian beam techniques for illuminating reflector antennas,” IEEE Transactions on Antennas and Propagation, Vol. 37, No. 3, pp. 297–304, 1989.
14. Pozar, D.M. and Schaubert, D., *Microstrip Antennas: The Analysis and Design of Microstrip Antennas and Arrays*, John Wiley & Sons, Inc., 1995.
15. Woo, R., “Multipacting breakdown in coaxial transmission lines,” Proceedings of the IEEE, Vol. 56, No. 4, pp. 776–777, 1968.
16. Huang, J., Encinar, J.A., *Reflectarray Antennas*, IEEE Press, Wiley & Sons, Hoboken, NJ, 2008.
17. S.S.D. Jones et al., “Electromagnetic wave lens and mirror systems”, US Patent No 2,986,734, May 30, 1961 (filed July2, 1958)

18. Nayeri, P., Liang, M., Sabory-Garcia, R., Tuo, M., Yang, F., Gehm, M., Xin, H., Elsherbeni, A.Z., "3D Printed Dielectric Reflectarrays: Low-Cost High Gain Antennas at Sub-Millimeter Waves," *IEEE Trans. On Antennas and Propagation*, DOI 10.1109/TAP.2014.2303195, 2013.
19. Encinar, J.A., Zornoza, J.A., "Three - layer printed reflectarrays for contour beam space applications," *IEEE Trans. Antennas Propagat.*, Vol. 52, pp. 1138–1148, 2004.
20. Thales Alenia Space, "R&D Main Achievements on Reflectarrays," available at: http://www.asi.it/files/DBresciani_4-11-13.pdf, downloaded March 2014.
21. Pozar, D.M., "Microstrip reflectarrays myths and realities," *Proceedings of the JINA International Symposium on Antennas*, Nice, France, pp. 175–179, 2004.
22. Pozar, D.M., "Bandwidth of reflectarrays," *Electronics Letters*, Vol. 39, pp. 1490-1491, Oct. 2003.
23. Rahim, M.K.A., Masri, T., Majid, H.A., Ayop, O., Zubir, F., "Design and Analysis of Ultra Wide Band Planar Monopole Antenna," *World Scientific and Engineering Academy and Science Transactions and Communications*, Vol. 10, No. 7, pp. 212-221, July 2011.
24. Sarchet, M., "AEHF Update: presentation to AFCEA Los Angeles Chapter," delivered March 2012, available at: https://afcea-la.org/sites/afcea-la.org/files/Sarchet%20AEHF%20AFCEA%20brf%20-%20as%20of%2022%20Mar%2012_0.pdf, downloaded April 2014.
25. Christodoulou, C.G., Tawk, Y., Lane, S.A., Erwin, S.R., "Reconfigurable antennas for wireless and Space Applications," *Proceedings of the IEEE*, Vol. 100, No. 7, pp. 2250-2261, 2012.
26. Pereira, R., Gillard, R., Sauleu, R., Potier, P., Dousset, T., Delestre, X., "Dual linearly-Polarized Unit-cells with Nearly 2-Bit Resolution for Reflectarray Applications in X-Band," *IEEE Transactions on Antennas and Propagation*, Vol. 60, No. 12, pp.6042-6048, 2012.
27. Inam, M., Ismail, M.Y., Zain, A.F.M., Misran, N., "Multi-State Frequency Switchable Reflectarray Antenna Design," *Proceeding of the IEEE International Conference on Space Science and Communication*, pp.253-256, 2013.
28. Kohmura, A., Lanteri, J., Ferrero, F., Migliaccio, C., Futatsumori, S., Yonemoto, N., "Ka-Band Beam Switchable Fresnel Reflector," *Proceedings of the International Symposium on Antennas and Propagation*, pp. 535-538, 2012.
29. Zainud-Deen, S.H., Gaber, S.M., Awadalla, K.H., "Beam Steering Reflectarray Using Varactor Diodes," *IEEE Japan-Egypt Conference for Electronics, Communications and Computers*, pp.178-181, 2012.
30. Hasani, H., Perruisseau-Carrier, J., Peixeiro, C., Mosig, J., "Dual-Band Dual Polarized Reconfigurable Unit-Cell for Reflectarray Antenna in Ku-Band," *Proceedings of the European Conference on Antennas and Propagation*, pp.861-862, 2013.
31. Kishor, K.K., Hum, S.V., "An Amplifying Reconfigurable Reflectarray Element," *IEEE Proceedings of the Antennas and Propagation Society International Symposium*, DOI: 10.1109/APS.2010.5561002, pp. 1-4, 2010
32. Microsemi, Space Solutions Brochure, http://www.microsemi.com/document-portal/doc_download/131787-microsemi-space-solutions-brochure

33. Montori, S., Chiappesi, E., Farinelli, P., Marcaccioli, L., Vincenti, G., Sorrentino, R., "W-band beam-steerable MEMS-based reflectarray," *International Journal of Microwave and Wireless Technologies*, Vol. 3, No.5, pp.522-532, 2011.
34. Rajagopalan, H., Rahmat-Samii, Y., and Imbriale, W.A., "RF MEMS actuated reconfigurable reflectarray patch-slot element," *IEEE Transactions on Antennas and Propagation*, 56(12), 3689–3699, 2008.
35. Salti, H., Fourn, E., Gillard, R., Legay, H., Minimization of MEMS breakdowns effects on the radiation of a MEMS based reconfigurable reflectarray , *IEEE Transactions on Antennas and Propagation*, 2010;58(7):2281–2287, doi: 10.1109/TAP.2010.2048861.
36. Uttamchandani, D., *Handbook of Mems for Wireless and Mobile Applications*, Woodhead publishing, 2013.
37. Okoniewski, M., McFeetors, G., "Radio Frequency MicroElectroMechanical Systems Components," *Microwaves, Radar & Wireless Communications*, pp, 147-154, 2006.
38. Blondy, P., Pothier, A., Stefanini, R., Gauvin, J., Passerieux, D., Vendier, O., Courtade, F., "Development of an All-Metal Large Contact Force Reliable RF-MEMS Relay for Space Applications," *Proceedings of the 42nd European Microwave Conference*, pp 184-185, 2012.
39. Romanofsky, R. R., "Advances in Scanning Reflectarray Antennas Based on Ferroelectric Thin-Film Phase Shifters for Deep Space Communications," *Proceedings of the IEEE*, Vol. 95, No. 10, pp. 1968-1975, 2007.
40. Romanofsky, R. R., Mueller, C., Chandrasekar, C. V., Concept for a Low Cost, High Efficiency Precipitation Radar System Based on Ferroelectric Reflectarray Antenna," *Proceedings of the IEEE National Radar Conference*, DOI: 10.1109/RADAR.2009.4977135, 2009.
41. Pringle, L. N., Harms, P. H., Blalock, S. P., Kiesl, G. N., Kuster, E. J., Friederich, P. G., Prado, R. J., Morris, J. M., Smith, G. S., "A Reconfigurable Aperture Antenna Based on Switched Links Between Electrically Small Patches," *IEEE Transactions on Antennas and Propagation*, Vol. 52, No. 6, pp. 1434-1446, 2004.
42. Li, Q., *Liquid Crystals Beyond Displays: Chemistry, Physics and Applications*, John Wiley & Sons, Hoboken, NJ, 2012.
43. Gaebler, A., Moessinger, A., Goelden, F., Manabe, A., Goebel, M., Follmann, R., Koether, D., Modes, C., Kipka, A., Deckelmann, M., Rabe, T., Schulz, B., Kuchenbecker, P., Lapanik, S., Mueller, S., Haase, W., and Jakoby, R., "Liquid Crystal Reconfigurable Antenna Concepts for Space Applications at Microwave and Millimeter Waves," *International Journal of Antennas and Propagation*, Vol. 2009.
44. Nickolas, K., "Liquid Crystal Polymer: Enabling Next-Generation Conformal and Multilayer Electronics," *Microwave Journal*, Vol. 51, N. 5, pg. 188-200, 2008.
45. Uber, C.F., Tremer, M.E., Lane, S., Gallagher, E.E., Collins, S.R., Benoit, M.R., "Radiation Testing of Liquid Crystal Optical Phase Shifters for Space Survivability," *Proceedings of the Military Communications Conference*, DOI: 10.1109/MILCOM.2008.4753053, 2008.
46. A. Manabe, "Liquid crystals for microwave applications," in *Proc 7th Eur. Conf. Antennas Propag. (EUCAP)*, Gothenburg, Sweden, 2013, pp. 1973–1974.

47. Farinelli, P.; Montori, S.; Fritzsche, C.; Chiappesi, E.; Marcaccioli, L.; Giacomozzi, F.; Sorrentino, R.; Jakoby, R., "MEMS and combined MEMS/LC technology for mm-wave electronic scanning," Proc. Of Millimeter Waves and THz Technology Workshop (UCMMT), 2013 6th UK, Europe, China, 2013.
48. Perez-Palomino, G., Barba, M., Encinar, J.A. Cahill, R., Dickie, R., Baine, P., Bain, M., "Design and Demonstration of an Electronically Scanned Reflectarray Antenna at 100 GHz Using Multiresonant Cells Based on Liquid Crystals," IEEE transactions on Antennas and Propag. 2015.
49. P. G. de Gennes and J. Prost. The Physics of Liquid Crystals. Clarendon Press, Oxford, second paperback edition, 1995.
50. M.J. Stephen and J.P Straley. Physics of liquid crystals. Rev. Mod. Phys., 46:617–704, 1974.
51. Epifanio G. Virga. Variational Theories for Liquid Crystals. CRC Press, 1994.
52. Andrienko, D., "Introduction to Liquid Crystals," http://www2.mpi-mainz.mpg.de/~andrienk/teaching/IMPRS/liquid_crystals.pdf (14 September 2006).
53. Mueller, S., Moessinger, A., Marin, R., Goelden, F., Lapanik, A., Haase, W., Jakoby, R., "Liquid Crystals-Microwave Characterization and Tunable Devices," Frequenz, Vol. 61, pg 217-223, 2007.
54. Utsumi, Y., Kamei, T., Naito, R., "Measurements of effective dielectric permittivity of microstrip-line-type liquid crystal devices using inductive coupled ring resonator," Electronics Letters, Vol. 39, No. 11, pg 849-850, 2003.
55. Arslanagić, S., Hansen, T.V., Mortensen, N.A, Gregersen, A.H., Sigmund, O., "A review of the scattering parameter extraction method with clarification of ambiguity issues in relation to metamaterial homogenization," *Antennas and Propagation Magazine, IEEE* 55.2 (2013): 91-106.
56. Lopez, A.G.; Lopez E.E.; Chandra R.; Johansson A.J., "Optimization and fabrication by 3D printing of a Volcano Smoke Antenna for UWB Applications," Proc. of the 7th European Conference on Antennas and Propagation, pp.1471-1473, 2013.
57. Garcia C.R.; Rumpf R.C.; Tsang H.H.; Barton J.H., "Effects of extreme surface roughness on 3D printed horn antenna," IEEE Electronics Letters, Vol. 49, No. 12, June 2013.
58. Advanced Circuit Materials Division, *RT/duroid 6006/6010LM High Frequency Laminates*, Data Sheet 1.6000, Revised 1058 071913, Publication #92-105, 2013.
59. Jones, R.G., "Precise dielectric measurements at 35 GHz using an open microwave resonator," Proc. Inst.Elec. Eng., v. 123, No 4, p. 285-290, Apr. 1976.
60. Yu, P.K., Cullen, A.L., "Measurement of permittivity by means of an open resonator: I. Theoretical," Proc. R. Soc. Lond. A., vol. 380, p.49-71,1982
61. Zhu B.; Vanlooocke S.; Stiens J.; Zutter D.D.; Elhawil A.; Tandt C.D.; Vounckx R., "A novel 3D printed focusing probe in scattering-type scanning near-field millimetre & terahertz wave microscope," Proc. of the 5th European Conference on Antennas and Propagation, pp.745-748, 2011.

62. Geterud E.G.; Bergmark P.; Yang J., “ Lightweight waveguide and antenna components using plating on plastics,” *Proc of the 7th European Conference on Antennas and Propagation*, pp.1812-1815, 2013.
63. Ivanov, S. A., Belyae. V.V, Zeinalov, A., Ostrovskii, B.I., “Characteristics of the behavior of elastic constants of liquid crystal due to reentrant polymorphism,” *Eksp. Teor. Fiz.* 91,560-568, August 1986.
64. L. Leger, A. Martinet. VISCOSITY MEASUREMENTS IN THE NEMATIC AND SMECTIC A PHASES OF A LIQUID CRYSTAL CRITICAL BEHAVIOUR. *Journal de Physique Colloques*, 1976, 37 (C3), pp.C3-89-C3-97.
65. Senyuk, B., Liquid Crystals: A simple view on a complex matter; 4. Anisotropy in Liquid Crystals, available online at: <http://www.personal.kent.edu/~bisenyuk/liquidcrystals/maintypes4.html>, accessed 9-1-2015.
66. P. G. de Gennes and J. Prost. *The Physics of Liquid Crystals*. Clarendon Press, Oxford, 2nd Ed., 1995
67. Diisanayake, A., Allnutt, J., Haidara, F., “A prediction model that combines rain attenuation and other propagation impairments along Earth-satellite paths,” *Online Journal of Space Communications*, Is. 2, 2002.
68. Gaebler, A., Moessinger, A., Goelden, F., et al. “Liquid crystal-reconfigurable antenna concepts for space applications at microwave and millimeter waves,” *Int. Journ. Antennas Propag.* 2009.
69. Tarumi, K., Finkenzeller, U. and Schuler, B., “Dynamic behavior of twisted nematic liquid crystals,” *Japanese Journal of Applied Physics*, 31:pages 2829–2836. Sept. 1992.
70. Seviour, R., “Fundamentals of Metamaterials for High Power RF Applications,” AFRL-AFOSR-UK-TR-2012-0001.
71. Mallon, K., “TWTAs for satellite communications: Past, present and future,” *Vacuum electronics conference proceedings*, 2008.
72. TELEDYNE MEC, Solid state products:
<http://www.teledynemicrowave.com/index.php/more-satcom-hw-9/twt-communication>
73. Kingsley, N., “Liquid Crystal Polymer: Enabling Next-Generation Conformal and Multilayer Electronics,” *Microwave Journal*, May 2008, pp. 188-195.
74. Kim, Y.K., Senyuk, B., Lavrentovich, O.D., “Molecular reorientation of a nematic liquid crystal by thermal expansion,” *Nat Commun*, 3:1133, 2012.
75. Ennis, C.P., Kaiser, R.I., “Mechanistical studies on the electron-induced degradation of polymethylmethacrylate and Kapton,” *Physical Chemistry Chemical Physics Journal*, DOI: 10.1039/c0cp01130d, 2010.
76. Ryan Hoffman, Personal communication on radiation degradation in materials , October 19, 2015.
77. Lane, S.A., Brown, J.A., Tremer, M.E., Uber, C., Gallagher, E.E., Collins, S.R., Benoit, M.R., Miniscalco, W.J., “Radiation testing of liquid crystal optical devices for space laser communication,” *Optical Engineering*, Vol 48, Issue 11, Nov 2009.

78. Tsoufanidis, N., Landsberger, S., *Measurement and Detection of Radiation*, 4th ed. CRC Press, Boca Raton, FL, 2011.
79. Kim, W., Jun, I., Garrett, H.B., "An Algorithm For Determining Energy Deposition Profiles In Elemental Slabs By Low Energy Electrons: An Internal Charging Application," IEEE Transactions in Nuclear Sciences, Vol 55, Issue 6, 2008.
80. Paulmier, T., Hanna, R., Belhaj, M., Dirassen, B., et. al., "Aging Effects and Induced Electric Phenomena on Dielectric Materials Irradiated with High Energy Electrons," IEEE Trans on Plasma Science, Vol 41, No. 12 Dec 2013
81. Kim, W., Jun, I., Garrett, H.B., "Modeling of Deep-dielectric Spacecraft Charging in Realistic Environment with NUMIT2", 3rd AIAA Atmospheric Space Environments Conference June 2011, AIAA 2011-3975.
82. Fredickson, A.R., Bell, J.T., "Analytic Approximation for Charge Current and Deposition by .1 to 100 MeV Electrons in Thick Slabs," IEEE Trans on Nuclear Science, Vol 42 No 6, Dec 1995.
83. Wilson, G., Dennison, J.R., "Approximation of Range in Materials as a Function of Incident Electron Energy," Proceedings of the 11th Spacecraft Charging Technology Conference, 2010.
84. Li, W., Yang, L., Yussan. L., Shenbou, G., "Research of a Large Dielectric Plate Antenna Charging in Low-Altitude Polar Orbit Environment," 6th Spacecraft Charging Technology Conference, pp.143-146, 2000.